

© Copyright by Sohini Sengupta 2016

All Rights Reserved

PROPERTIES OF A 2D PERIODIC LEAKY WAVE ANTENNA AT
MICROWAVE AND OPTICAL FREQUENCIES

A Dissertation

Presented to

the Faculty of the Department of Electrical and Computer Engineering

University of Houston

In Partial Fulfillment

of the Requirements for the Degree

Doctor of Philosophy

in Electrical Engineering

by

Sohini Sengupta

August 2016

PROPERTIES OF A 2D PERIODIC LEAKY WAVE ANTENNA AT
MICROWAVE AND OPTICAL FREQUENCIES

Sohini Sengupta

Approved:

Chairman of the Committee
Dr. David R. Jackson, Professor,
Electrical and Computer Engineering

Committee Members:

Dr. Stuart A. Long, Professor,
Electrical and Computer Engineering

Dr. Donald Wilton, Professor,
Electrical and Computer Engineering

Dr. Lowell Wood, Professor,
Physics

Dr. Daniel Onofrei,
Assistant Professor,
Mathematics

Dr. Suresh Khator, Associate Dean,
Cullen College of Engineering

Dr. Badrinath Roysam,
Department Chair and Professor,
Electrical and Computer Engineering

ACKNOWLEDGEMENTS

It has been a great experience to do the research for my Ph. D. dissertation. I am glad that I got the opportunity to work on an interesting project. I would like to thank my advisor Dr. David Jackson for his invaluable guidance through the course of the research. I think I am very fortunate to have him as my advisor because of his deep understanding of the subject, his wealth of knowledge, and his power of reasoning. I would like to thank Dr. Stuart Long for employing me as his teaching assistant and for all the support he provided. I want to thank Dr. Wilton for all the “pocket coffee” he gave me, which helped me stay sharp while I was struggling to finish the dissertation. Dr. Jackson, Dr. Wilton, and Dr. Long are some of the best professors I have encountered. They have taught excellent courses which have been very helpful in laying the theoretical foundation upon which my research is based. It is wonderful how they treat their students with a lot of respect and consideration. I would like to thank Dr. Daniel Onofrei and Dr. Lowell Wood for taking an interest in my work and being part of my dissertation committee.

My parents have always given me unconditional love and support and that gives me the strength to be an independent and free-thinking individual and pursue my dreams without fear of consequences. My brother has been my best friend for life, and I am always inspired by his kindness and courage.

The time I spent doing the research for my Ph. D. was time well-spent. Not only did I gain a lot of invaluable knowledge of electromagnetics, but I made some truly wonderful friends in the lab – Dr. Krishna Kota, Nick Boggs, Xinyu Liu, Mona Yang, and Dr. Anthony Lau. Their friendship and camaraderie has introduced fun and light-heartedness into the seriousness of pursuing a Ph. D. degree.

PROPERTIES OF A 2D PERIODIC LEAKY WAVE ANTENNA
AT MICROWAVE AND OPTICAL FREQUENCIES

An Abstract
of a
Dissertation
Presented to
the Faculty of the Department of Electrical and Computer Engineering
University of Houston

In Partial Fulfillment
of the Requirements for the Degree
Doctor of Philosophy
in Electrical Engineering

by
Sohini Sengupta
August 2016

ABSTRACT

Highly focused and directional beams of electromagnetic radiation can be obtained using a two-dimensional periodic leaky wave antenna (2D periodic LWA) formed by a periodic arrangement of metal patches on a grounded dielectric layer, excited by a simple source such as a slot in the ground plane. The slot in the ground plane launches a radially-propagating (cylindrical) TM_0 surface wave, guided by the grounded substrate. This surface wave becomes perturbed into a leaky wave due to the periodic patches, resulting in radiation from a higher-order space harmonic (Floquet wave) of the leaky wave, producing a beam that is asymmetric, being narrower in the E plane than in the H plane. Such structures are extremely simple in construction and can produce very narrow beams at broadside. The leaky wave propagates anisotropically, having a complex wavenumber that varies with the angle of propagation. One of the goals of this investigation is to characterize the wave propagation and radiation characteristics of this class of 2D periodic leaky-wave antennas, and to show how the beam properties can be optimized.

The phenomenon of directive beaming at optical frequencies using a periodically corrugated plasmonic metal (e.g., silver) film can be explained and studied in terms of leaky plasmon waves. The structure usually consists of a periodic set of grooves surrounding a subwavelength aperture in a thin silver film. At optical frequencies the silver has a negative permittivity due to plasmonic behavior, allowing for the guidance of a plasmon wave (similar to the TM_0 surface wave that propagates on a grounded substrate layer at microwave frequencies). The grooves perturb the cylindrically propagating plasmon wave that is launched by the subwavelength aperture. Therefore, the structure

has a physical principle of operation similar to the periodic metal-patch LWA at microwave frequencies. The theory developed for the microwave LWA discussed above is applied to the plasmonic directive-beaming structure to illustrate its fundamental principle of operation, and to show how it can be optimized.

TABLE OF CONTENTS

Acknowledgements.....	v
Abstract.....	vii
Table of Contents.....	ix
List of Figures.....	xii
List of Tables.....	xvii
Chapter 1 Introduction.....	1
1.1 Background and Motivation.....	2
1.2 Review of Previous Work.....	3
1.3 Leaky-Wave Theory.....	13
1.4 Proposed Structure of the 2D Periodic Leaky-Wave Antenna.....	14
1.5 Organization of the Dissertation.....	16
Chapter 2 Theoretical Foundation.....	18
2.1 Nature of the Leaky Waves.....	18
2.2 Far Field Calculation - Spectral Domain Immittance (SDI) with Reciprocity to Analyze the Periodic Leaky-Wave Antenna.....	19
2.3 Current Distribution and Near Field Calculation – Using the Array Scanning Method for the Currents on the Patches of the 2D Periodic LWA Structure.....	34

2.4 Solving for the Wavenumber of the Leaky Wave on the 2D Periodic LWA	
Structure	47
2.5 Enhancement Factor.....	48
2.6 CAD Formula for Calculating the Radiation Pattern of a 1D Leaky-Wave	
Antenna	49
2.7 Grating Lobes.....	51
Chapter 3 Radiation Characteristics of the 2D Periodic Microwave Antenna	57
3.1 Optimization of the 2D Periodic Leaky-Wave Antenna.....	57
3.2 Radiation Patterns	60
3.3 Variation of the Main Beam with Frequency	65
3.4 CAD Formula for the Leaky-Wave Radiation Pattern	66
3.5 Designs for 2D Periodic Leaky-Wave Antenna with Different Practical Substrates	
.....	69
3.6 Cross-Section of the Main Beam for Different Power Levels	77
3.7 Variation of Beamwidth and Enhancement Factor with the Length of the Patches	
.....	80
3.8 Bandwidth, Figure of Merit, and Normalized Tolerance of the 2D Periodic Leaky-	
Wave Antenna.....	82
Chapter 4 Properties of the Leaky Wave in the 2D Periodic Microwave Antenna	85
4.1 Current Distribution on the Patches	85

4.2 Relation Between the Propagation and Attenuation Constants of the Leaky Mode and the Radiation at Broadside	88
4.3 Dispersion Behaviour – Variation of Leaky-Mode Wavenumber as a Function of the Azimuthal Angle ϕ	91
4.4 CAD Formula to Predict the Shape of the Main Beam at Arbitrary Angle ϕ	93
4.5 Formation of the Grating Lobes and Predicting their Location	96
4.6 Radiation Efficiency of the 2D Periodic Leaky-Wave Antenna.....	107
Chapter 5 Plasmonic Structure – Directive Beaming at Optical Frequencies	112
5.1 Radiation Patterns and Radiation Properties.....	114
5.2 CAD Formula to Calculate the Radiation Pattern of the Leaky-Wave Beam	119
5.3 Current Distribution on the Patches from the Array Scanning Method.....	123
5.4 Dispersion Behaviour – Variation of Leaky Plasmon Wavenumber as a Function of the Azimuthal Angle ϕ	125
Chapter 6 Summary and Conclusions.....	129
6.1 Summary	129
6.2 Conclusions.....	131
6.3 Future Work	134
References.....	137

LIST OF FIGURES

Fig. 1.1. Schematic of the 2D periodic leaky-wave antenna under consideration.....	15
Fig. 2.1. Distribution of the surface-wave field over the 2D periodic leaky-wave antenna structure, when excited by a horizontal magnetic dipole	19
Fig. 2.2. Side view of the 2D periodic leaky-wave antenna for microwave frequencies	20
Fig. 2.3. Side view of the 2D periodic leaky-wave antenna for optical frequencies	20
Fig. 2.4. TEN model for the LWA structure with the patch currents as the source.....	26
Fig. 2.5. The orientation of the vectors \hat{u} and \hat{v} with respect to the x and y axes	28
Fig. 2.6. The surface current \tilde{J}_s and the magnetic fields it produces at the surface.....	29
Fig. 2.7. The 2D periodic leaky-wave antenna	34
Fig. 2.8. A single source is replaced by infinite array of sources in the ASM calculation	35
Fig. 2.9. Side view of the 2D periodic leaky-wave antenna for the microwave case	36
Fig. 2.10. The TEN model for the layers of the LWA with the series voltage source (magnetic dipole).....	40
Fig. 2.11. Representation of current on a bi-directional 1D leaky-wave antenna in free space	49
Fig. 2.12. Circle diagram to explain the grating lobes	52
Fig. 2.13. Direction of the radial component of the leaky wave and the plane of observation	53
Fig. 3.1. Optimization of the beam at broadside.....	58

Fig. 3.2. Contour plot of the power radiated at broadside for different values of a and b	58
Fig. 3.3. Plot of optimized maximum electric field at broadside vs b	59
Fig. 3.4. (a)-(f) Radiation patterns in different ϕ planes for a lossless substrate with $L = 0.25$ cm	61
Fig. 3.5. (a)-(f) Radiation patterns in different ϕ planes for a lossless substrate with $L = 0.30$ cm	62
Fig. 3.6. (a)-(f) Radiation patterns in different ϕ planes for a lossy substrate with $L = 0.25$ cm	63
Fig. 3.7. (a)-(f) Radiation patterns in different ϕ planes for a lossy substrate with $L = 0.30$ cm	64
Fig. 3.8. Splitting of the beam in the E-plane, when the frequency is changed from the optimum frequency of 12 GHz	65
Fig. 3.9. Variation of the beam in the H-plane, when the frequency is changed from the optimum frequency of 12 GHz	66
Fig. 3.10. (a) Pattern of the leaky-wave beam compared to the pattern from reciprocity in the E-plane. (b) An expanded view of the main beam around the -20 dB power level	68
Fig. 3.11. Pattern of the leaky-wave beam compared to the pattern from reciprocity in the H-plane	68
Fig. 3.12. Radiation patterns in E-plane, H-plane, and D-plane ($\phi = 45^\circ$)	69
Fig. 3.13. Radiation patterns in E-plane, H-plane, and D-plane ($\phi = 45^\circ$)	70
Fig. 3.14. Radiation patterns in E-plane, H-plane, and D-plane ($\phi = 45^\circ$)	71

Fig. 3.15. Radiation patterns in E-plane, H-plane, and D-plane ($\phi = 45^\circ$).....	71
Fig. 3.16. Radiation patterns in E-plane, H-plane, and D-plane ($\phi = 45^\circ$).....	72
Fig. 3.17. Radiation patterns in E-plane, H-plane, and D-plane ($\phi = 45^\circ$).....	72
Fig. 3.18. Radiation patterns in E-plane, H-plane, and D-plane ($\phi = 45^\circ$).....	73
Fig. 3.19. Radiation patterns in E-plane, H-plane, and D-plane ($\phi = 45^\circ$).....	74
Fig. 3.20. Radiation patterns in E-plane, H-plane, and D-plane ($\phi = 45^\circ$).....	75
Fig. 3.21. Radiation patterns in E-plane, H-plane, and D-plane ($\phi = 45^\circ$).....	75
Fig. 3.22. Radiation patterns in E-plane, H-plane, and D-plane ($\phi = 45^\circ$).....	76
Fig. 3.23. Radiation patterns in E-plane, H-plane, and D-plane ($\phi = 45^\circ$).....	77
Fig. 3.24. Cross-section of beam at a power level of -3 dB.....	78
Fig. 3.25. Cross-section of beam at a power level of -6 dB.....	78
Fig. 3.26. Cross-section of beam at a power level of -9 dB.....	79
Fig. 3.27. Cross-section of beam at a power level of -12 dB.....	79
Fig. 3.28. Beamwidths and enhancement factors vs length of patches for a lossy substrate	81
Fig. 3.29. Beamwidths and enhancement factors vs length of patches for a lossless substrate.....	81
Fig. 4.1. Current distribution from ASM on the patches in the E-plane.....	86
Fig. 4.2. Current distribution from ASM on the patches in the H-plane	87
Fig. 4.3. Current distribution from ASM and Designer on the patches in the E-plane....	88
Fig. 4.4. Plot of normalized α and β along the x -axis and the power radiated at broadside vs a	90

Fig. 4.5. Plot of normalized α and β along the y -axis and the power radiated at broadside vs b	90
Fig. 4.6. Dispersion diagram showing the variation of the phase constant with ϕ	92
Fig. 4.7. Dispersion diagram showing the variation of the attenuation constant with ϕ	92
Fig. 4.8. (a) Comparison of the main beam from reciprocity and the CAD formula for an angle $\phi = 45^\circ$. (b) An expanded view of the main beam around the -20 dB power level	94
Fig. 4.9. (a) Comparison of the main beam from reciprocity and the CAD formula for an angle $\phi = 60^\circ$. (b) An expanded view of the main beam around the -20 dB power level	94
Fig. 4.10. (a) Comparison of the main beam from reciprocity and the CAD formula for an angle $\phi = 75^\circ$. (b) An expanded view of the main beam around the -20 dB power level	95
Fig. 4.11. (a) Comparison of the main beam from reciprocity and the CAD formula for an angle $\phi = 85^\circ$. (b) An expanded view of the main beam around the -20 dB power level	95
Fig. 4.12. Grating lobe predicted using the CAD formula for case 1	98
Fig. 4.13. Grating lobe predicted using the CAD formula for case 2	100
Fig. 4.14. Grating lobe predicted using the CAD formula for case 3	101
Fig. 4.15. Grating lobe predicted using the CAD formula for case 4	103
Fig. 5.1. Directive beaming in a silver film with corrugations around a subwavelength aperture. (a) Cross-section view, (b) 3D view of the plasmonic structure	112

Fig. 5.2. Top view and cross-sectional view of the silver film, with the grooves modeled as perfectly conducting patches and the aperture modeled as a magnetic dipole	113
Fig. 5.3. Contour plot of the power radiated at broadside for different values of a and b	115
Fig. 5.4. Radiation patterns for different angles ϕ , calculated with 5 basis functions ...	116
Fig. 5.5. Radiation patterns for different angles ϕ , calculated with 1 basis function.....	117
Fig. 5.6. Beamwidths and enhancement factor vs. the length of the patches	118
Fig. 5.7. Pattern of the leaky-wave beam compared to the pattern from reciprocity in the E-plane for a lossy silver substrate	120
Fig. 5.8. Pattern of the leaky-wave beam compared to the pattern from reciprocity in the H-plane for a lossy silver substrate	121
Fig. 5.9. Pattern of the leaky-wave beam compared to the pattern from reciprocity in the E-plane for a lossless silver substrate	122
Fig. 5.10. Pattern of the leaky-wave beam compared to the pattern from reciprocity in the H-plane for a lossless silver substrate	122
Fig. 5.11. Current distribution on the patches in the E-plane from ASM.....	124
Fig. 5.12. Current distribution on the patches in the H-plane from ASM	125
Fig. 5.13. Dispersion diagram showing the variation of the phase constant with ϕ	126
Fig. 5.14. Dispersion diagram showing the variation of the attenuation constant with ϕ	127

LIST OF TABLES

Table 3.1. Bandwidth, figure of merit, exact directivity, approximate directivity, and beamwidths in the E-plane and the H-plane for the 2D periodic leaky-wave antenna for different lengths L of the patches, for a lossless substrate	83
Table 3.2. Bandwidth, normalized tolerance, and beamwidths in the E-plane and the H-plane for the 2D periodic leaky-wave antenna for different lengths L of the patches, for a lossy substrate	84
Table 4.1. Tracking the grating lobe due to the $(-1, 0)$ Floquet harmonic of the E-plane leaky mode (perturbed surface wave mode).....	104
Table 4.2. Tracking the grating lobe due to the $(-1, -1)$ Floquet harmonic of the E-plane mode (perturbed surface wave mode)	105
Table 4.3. Tracking the grating lobe due to the $(0, -1)$ Floquet harmonic of the H-plane mode	106
Table 4.4. Radiation efficiency vs. length of patches	111

CHAPTER 1 INTRODUCTION

A leaky-wave antenna can be thought of as a guided-wave structure that has been modified to gradually leak out power from the guided mode along the direction of propagation of the guided mode. The power leakage is dependent on factors like the geometric parameters of the structure with respect to the wavelength of operation, the materials comprising the guiding structure, the frequency of operation, and the guided mode from which the leakage occurs. Leaky-wave structures can be designed to produce narrow beams that scan over a range of angles from broadside to endfire. The attenuation constant, due to the leakage of power, and the phase constant need to be carefully considered in designing these antennas, and therefore their design is fairly complicated. A 2D leaky-wave antenna design is more complicated than that of a 1D leaky-wave antenna, and therefore it becomes necessary to carefully study the behavior of these structures. Understanding the fundamental principles of operation of the 2D leaky-wave antenna is very important in order to design these antennas.

Various books and book chapters cover the basics of leaky-wave antennas (LWAs) [1–7]. The first leaky-wave antenna was a waveguide with a slit along its side [8, 9], being a 1D uniform LWA. After that came waveguides with closely spaced holes instead of a slit, which produced narrower beams by having less perturbations per unit length [10], being a 1D quasi-uniform LWA. A 1D periodic LWA called the “sandwich wire antenna” [11] was studied but was found to be not practical. In [12] the concept of introducing a uniform or periodic asymmetry to turn a waveguide or transmission line structure into a leaky-wave antenna was first introduced. Oliner and others did much work on 1D LWAs, and a comprehensive report was published [13].

Von Trentini began work on 2D LWAs using a 2D periodic partially reflective screen over a ground plane in order to produce narrow pencil beams at broadside [14]. It was the first quasi-uniform 2D LWA, although it was not recognized as such. Jackson and Alexopoulos studied uniform 2D LWAs consisting of a superstrate over a grounded substrate in [15, 16], though again it was not originally recognized that this structure was acting as a 2D LWA. This structure was further analyzed by Jackson and Oliner in [17, 18] from a leaky-wave point of view. A 2D LWA using a partially reflective surface was further explored in [19] using different kinds of elements. The radiation characteristics of a 2D quasi-uniform LWA with metal patches and slots was studied in [19, 20]. Since then, metamaterial structures have also been used in the design of LWAs [22 – 25].

1.1 Background and Motivation

In the area of optics, the phenomenon of directive beaming of light through a sub-wavelength aperture has been observed, wherein a beam of light incident on the sub-wavelength aperture in a thin sheet of a plasmonic metal such as silver emerges on the other side as a highly directive narrow beam of light. This occurs when the sub-wavelength aperture is surrounded by a periodic set of optimized grooves on the exit surface. When the entrance face of the metal sheet is similarly covered by an optimized periodic distribution of grooves around the aperture, there is an enhancement of the power transmitted through the aperture. This optical effect is known as enhanced transmission of light through a sub-wavelength aperture and is related to the directive beaming effect by reciprocity. Usually the periodicity of the periodic structure placed around the aperture is optimized for maximum radiation at broadside, but it can also be

designed to produce beams with different scan angles. It has been shown that this phenomenon is due to leaky-wave radiation from a surface plasmon wave supported by the metal film [26, 27]. Therefore, leaky-wave theory has been found to be successful in the design and optimization of the 1D plasmon structures and in predicting their behavior. In this work we shall apply the concepts of 2D leaky waves to predict the behavior of 2D periodic plasmon structures. The surface plasmon mode in the plain metal film becomes leaky due to the presence of a 2D periodic corrugation at the surface.

1.2 Review of Previous Work

Much research has been done in the area of leaky-wave antennas and some interesting designs have emerged, and various methods and approaches for analyzing these structures have been proposed and demonstrated. Some of these previous works that are relevant to the present study are discussed here.

In [28], a linear printed circuit LWA has been explored for microwave and millimeter-wave applications. Here modal analysis was performed on the unit cell, based on the spectral-domain method. The beam-scanning properties of the LWA were studied in terms of spatial harmonics as a function of both phase shift and spacing between the periodic elements. This work explored the transition region between the surface wave and leaky wave regimes, and the formation of grating lobes due to the presence of additional complex improper modes. This work also analyzed the radiative properties of a linear array of microstrip LWAs, with focus on the occurrence of grating lobes in the pattern. A parametric analysis was also done on the dispersion behavior as a function of the phase shift and geometry.

Recently, substrate integrated waveguide (SIW) leaky-wave antennas have become popular. In [29] a new slotted substrate integrated waveguide (SIW) leaky-wave antenna is constructed by including a periodic set of centered transverse slots on the top surface of the SIW, in order to interrupt the current flow on the top conductor and produce leakage from the TE_{10} mode of the SIW. This structure is found to have a leaky mode, a proper waveguide mode, and a surface-wave type of mode all propagating on the structure. This work studied the design of a uniformly slotted SIW leaky-wave antenna that has a frequency dependent beam scanning from near broadside to forward endfire. This type of antenna has a wide impedance bandwidth and a narrow beam that scans with frequency. When the beam scans away from endfire, the radiation is coming from the leaky-wave mode. When the beam scans to endfire, the radiation is due to a combination of the proper waveguide mode and the surface-wave mode, in addition to the leaky mode. Another design for an SIW LWA [30] consists of a periodic arrangement of metallic vias where an open periodic waveguide structure supports the propagation of leaky-wave modes when the distance between the vias is large. It is seen that the leakage loss of the structure increases with distance between the vias. In this work the leakage loss is studied and is used to design a leaky-wave antenna based on the SIW structure. This can find application at millimeter-wave frequencies. The finite difference frequency domain method was used for analyzing the periodic leaky-wave antenna, and two modes were identified and analyzed – TE_{10} and TE_{20} . In this work a novel concept was applied, which utilizes the fact that the leakage loss increases as the via separation is increased, which enables the formation of leaky waves in the structure. The radiation properties of the leaky TE_{20} mode were found to be better than that of the TE_{10} mode.

In [31] an array factor approach was proposed for fast and efficient computation of the radiation pattern of complex metamaterial leaky-wave structures of arbitrary size. This method is based on the analysis of a single periodic unit cell of the structure.

A novel design of a leaky-wave antenna with a double-strip grating is proposed in [32], which consists of two strips per unit cell. With this design the stopband behavior around the broadside scan region can be almost (but not completely) eliminated. Therefore, this leaky wave antenna is able to scan from backward end-fire to forward end-fire without any large frequency range of high attenuation.

A full-wave numerical approach for the modal analysis of 2D printed periodic structures on a grounded dielectric slab was presented in [33]. The proposed method allows the analysis of an arbitrary metallization in the unit cell over a grounded dielectric substrate. The method is based on a mixed-potential integral equation using the method of moments in the spatial domain to solve the integral equation.

Another full-wave numerical analysis method for the modal analysis of 2D periodic planar structures on a grounded dielectric slab with arbitrary metallization in the unit cell was introduced in [34]. Leakage effects are accounted for by choosing the correct path of integration in the spectral domain for each spatial harmonic.

The radiation patterns from a 2D Electromagnetic Band Gap (EBG) structure were studied in [35]. The structure consists of a metallic strip grating over a grounded dielectric substrate excited by a line source. This structure is theoretically studied with a full-wave spectral analysis, solved using the method of moments.

For aperiodic problems, the “array scanning method” (ASM) was used to find the solution from the corresponding periodic problem where the line source is also

periodically duplicated. Excitation of both proper and improper leaky-wave modes were investigated in this work. The Kirchoff-Huygens integral was used to calculate the radiation pattern due to the leaky wave from the complex propagation constant of the leaky wave. They found that the TM case allowed a small range of scanning angles due to a strong variation of the modal leaky-wave wavenumber with frequency. On the other hand, the TE case had a moderate variation of the modal leaky-wave wavenumber with frequency, so it had a wide range of scanning angles, with beam that scanned close to broadside. Overall, scanning from near end-fire to near broadside with a nearly constant beamwidth was obtained.

In [36], an equivalent transmission line model was developed using linearized series and shunt immittances to approximate the periodic (Bloch) structure of a periodic LWA. Based on that, asymptotic transmission line formulas were derived that characterized the propagation constant, impedance, energy, power, and quality factor for near broadside to off-broadside radiation in either the forward or backward directions. Then it was shown that for radiation at broadside, the total power in the series and shunt elements are always equal. Therefore there would be a fair amount of degradation in broadside radiation when only one of the two elements, either series or shunt, is responsible for the radiation and the other dissipates the energy. A condition for optimum broadside radiation was presented that is also found to be identical to the Heaviside condition for distortionless propagation in transmission line theory.

In reference [37], the mixed-potential integral equation along with the method of moments was used to analyze a 1D periodic leaky-wave antenna in a layered media. The unit cell contains an arbitrary 3D shaped metallic or dielectric structure in a layered

media. This method considers both periodic electric and magnetic current sources, including vertical current sources, and calculates both bound and leaky-mode wavenumbers.

In [38] a simple perturbation analysis is used to study the fields generated by a planar periodic leaky-wave antenna based on the perturbation of the surface-wave fields from a slot exciting a grounded dielectric substrate. The periodic LWA consists of a circular metallic grating on top of a grounded dielectric substrate, which causes the perturbation of the surface wave. Radiation is achieved using a fast $n = -1$ space harmonic. In order to characterize the complex radial wavenumber that corresponds to the leaky mode, a perturbation analysis was done on the surface wave excited by a slot in the grounded dielectric slab.

Reference [39] introduced a method to find the dispersion characteristics of open periodic structures. This method is based on the reflection pole method. When illuminated by a plane wave, the poles of the reflection coefficient will be the leaky or bound modes of the open waveguide structure. Here, the modes are tracked by varying the incident angle of the plane wave, and in case of low loss structures, the poles are detected based on the frequencies at which the surface impedance of the open structure resonates. In the slow-wave region, inhomogeneous plane wave incidence is used and a reflection coefficient is obtained that is greater than unity.

A leaky-wave antenna consisting of a metallic grating of concentric annular rings fed by a non-directive TM_0 surface wave source is presented in [40]. This antenna is meant for two-sided continuous beam scanning and directive pencil beam radiation at broadside. To ensure only the leakage of the TM_0 field and its radiation into the far-field region, the

launching of a TE polarized field distribution is suppressed over a large bandwidth by choosing the right grating periodicity and sectoring (which involves the removal of portions of the grating and the ground plane) of the 2D guiding structure. This antenna could be used for radar systems and communication applications. Suppressing the TE polarized surface wave launched by the source can increase the gain, minimize reflection losses, and reduce cross-polarization levels.

The design of a conformal leaky-wave antenna (CLWA) with a metal strip grating that utilizes a backward-radiating leaky wave to focus the beam is done in [41]. This work demonstrates that it is possible to get proper focusing of the beam towards broadside in spite of a smoothly curved aperture by modulating the periodicity of the metal strip grating. Using a bi-directional wave results in a doubling of the aperture but the directivity is also doubled. A simple 2D Fourier series analysis was used to interpret the radiation physics. One of the CLWA that was designed had different parts of the structure operating in the forward, open-stopband, and backward regions. All three sections corresponding to these three operating regions were modulated for radiation at broadside. It was also found that unlike the planar case, the open-stopband was not a problem for the LWA with curvature.

There have been several studies done on the Fabry-Pérot leaky-wave antenna, which has a partially reflective surface (PRS) over a grounded dielectric slab [42, 43]. This class of antenna has a structure that is somewhat similar to the periodic leaky-wave antenna discussed in this dissertation, and some of the fundamental physics is the same; but it has a very different mode of operation. Some of these Fabry-Pérot antennas have an artificial magnetic conductor (AMC) as the ground plane instead of the usual electric conductor as

the ground plane [44, 45]. This serves to reduce the height of the antenna structure. Reference [46] demonstrates a simple way to solve for the complex wavenumber and therefore the dispersive characteristics of a thin periodic 2D Fabry-Pérot leaky-wave antenna. This method eliminates the process of root-finding in the complex plane to get the leaky-wave complex wavenumber. This technique employs the method of moments and reciprocity in combination with array theory to get the complex dispersion characteristics. This technique is applicable for high gain planar leaky-wave antennas using PRS or AMC surfaces. However, this method does not work when grating lobes are present.

The motivation for the present research in this dissertation comes from the area of plasmonics, from the phenomena of directive beaming and enhanced transmission. Therefore, some of the most relevant research in this area is described below.

In [47] the link between the phenomena of extraordinary transmission and surface plasmons is noted. It is shown that the enhanced transmission is due to the coupling of light to the surface plasmon.

The fundamental physics behind the phenomena of directive beaming from a subwavelength aperture in a thin silver film is explored further in [48]. This reference points out that light passing through a subwavelength aperture would normally spread uniformly in all directions as it emerges through the small aperture that does not transmit light well. With periodic grooves on the surface of the silver film on the exit face, the transmitted light emerges as a highly directional and collimated beam. This reference identifies the excitation of surface plasmons that are diffracted by the grooves and produce the directional beam. In this reference a bull's-eye structure was studied.

Some of the most seminal works establishing the link between leaky waves and directive beaming were presented in [26] and [27]. Reference [27] provides a fundamental explanation for the directive radiation from a sub-wavelength aperture in a silver film surrounded by corrugations on the exit face, in terms of leaky-waves. This investigation provides evidence that the distribution of fields along the interface and the radiation from the structure is due to a leaky plasmon wave on the silver film. This work also showed that the $|\beta_{-1}| = \alpha$ relation holds for this structure in order to achieve maximum power density radiated at broadside, as it usually does in the case of leaky-wave radiation. A method to approximately calculate the radiation efficiency was also proposed here. In [26] the open stop band effect was described in detail, and it was shown that the directive beaming and enhanced transmission effects are related to each other by reciprocity.

The phenomena of enhanced transmission in a silver film by placing concentric ring nanoslits on the surface of the silver film was further explored in [49]. This structure was found to result in the generation of both radially and azimuthally polarized light, and the transmission through the structure was found to have spectral and spatial inhomogeneity.

The work in [50] provides a semi-analytical theoretical basis for the operation of a plasmonic structure made of a nano-slit aperture surrounded by surface corrugations, in terms of two nested coupled surface plasmon polariton modes. This leads to figures of merit defined for the structure, relating the structural parameters to the normal or oblique wave incidence or beaming. This allows for an easy optimization of the structure and a performance prediction.

Then, in [51] there was given a practical application of an optical antenna formed with a concentric ring grating around a subwavelength aperture, also known as a “bull’s-eye” structure. This grating improves the coupling of the incident illumination to the antenna, even when it is focused by an aplanatic lens and the beam that is produced is restricted to a small solid angle and is well-collimated.

The different ways to tweak the parameters to optimize the bull’s-eye structure were explored in [52]. Both an experimental and theoretical study were done and the resonance intensity variations dependent on different geometrical parameters were explored to see the patterns and form rules for the optimization of the transmission properties.

In [53] the corrugations in the bull’s-eye structure were placed in such a way that there is maximum leakage of radiation to the sides. Then, some secondary corrugations are added at some distance from the source, which cause reflection of these leaky waves thus trapping the leaky waves and producing standing waves with a strong optical (particle) trapping.

A method to convert surface plasmon polaritons into leaky-wave modes that produce radiation by using a periodic array of plasmonic nano-scatterers is demonstrated in [54]. The structure consists of a subwavelength slit placed next to an array of periodic gratings, which couples the energy from the slit into leaky plasmon waves. The coupling between the excitation and the surface plasmon polariton can be maximized by varying the slit width and the angle of excitation in order to channel the excitation more towards the grating side. This also has the advantage of suppressing slit diffraction.

In [55] a split bull’s-eye nanometer germanium antenna was designed to function as a photodetector. Here aluminum was used, which is a non-traditional plasmonic material,

in order to form the antenna structure that was meant for applications in optoelectronic devices. The new design, with the bull's-eye structure split in two halves, with a nanogap in between, can result in a significant enhancement in absorption over the area of illumination, allowing for a reduction in the grating area required. An optical leaky-wave antenna formed out of the semiconductor silicon was designed and analyzed and then integrated within a Fabry Pérot resonator in [56] in order to obtain better performance and better control over the intensity of radiation.

In [57], an optical leaky-wave antenna was introduced that consists of a silicon nitride dielectric with periodic silicon semiconductor corrugations. This structure produces a narrow beam radiation because of leaky wave present in the structure. This work also showed that by means of carrier injection in the semiconductor corrugations the antenna can be electronically tuned.

The design of a low profile horn antenna [58] was inspired by the optical leaky-wave antenna construction, taking advantage of the leaky waves to produce radiation. In this design a subwavelength aperture was placed in the middle of periodic concentric ring corrugations on a conducting plate. The aperture in the center was fed by a waveguide. This antenna operates on the principles of enhanced transmission/directive beaming and produces a narrow beam of radiation with a high gain. A bull's-eye corrugation is integrated with an artificially soft surfaces structure into the ground plane of a microstrip patch antenna to prevent diffraction from the edges and improve the pattern in [59].

1.3 Leaky-Wave Theory

A leaky-wave antenna operates by gradually leaking out energy from a guided mode or travelling wave. The wavenumber of the leaky guided mode along the direction of propagation (z -axis) is taken to be $k_z = \beta - j\alpha$ where β is the phase constant and α is the attenuation constant. A 1D leaky-wave antenna is one where the leaky guided mode travels in a fixed direction (called z). A 2D leaky-wave antenna is one where the leaky guided mode propagates out in a radial direction as a cylindrical wave.

Classification of leaky-wave antennas

Uniform The antenna is structurally uniform along the direction of propagation of the guided wave. The leaky-wave antenna radiates through one of the fast-wave modes of the waveguide, i.e. $\beta < k_0$. One of the most common examples of a 1D uniform LWA is a waveguide with a narrow slit along its length, or a wide microstrip line operating in its first higher-order mode, which is a fast-wave.

Periodic A waveguiding structure is used that supports a non-radiating guided wave that is a slow wave. When periodic discontinuities (in the form of metallization, slots, changes in permittivity, etc.) are introduced into the waveguiding structure, the guided mode is perturbed into an infinite number of space harmonics known as Floquet modes. The wavenumbers of the Floquet modes are periodically spaced. For a 1D LWA the phase constants are $\beta_n = \beta_0 + 2\pi n/p$, where p is the periodicity of the structure, β_n is the phase constant of the n^{th} space harmonic, and β_0 is the phase constant of the fundamental mode or the 0^{th} space harmonic. One of these Floquet modes, usually $n = -1$, can be designed

to be a fast wave and thus become leaky and radiate, making a leaky-wave mode out of the mode on the waveguiding structure. The structure is designed so that the $n = -1$ space harmonic is the only space harmonic that radiates, forming a single beam that can scan from broadside to endfire in both the forward and backward directions, unlike the uniform LWA that is usually limited to scanning only in the forward direction.

Quasi-Uniform Quasi-uniform LWAs are geometrically similar to the periodic LWAs and also have infinite number of space harmonics or Floquet modes. However, they behave as uniform leaky-wave antennas. The quasi-uniform LWAs have a period that is much smaller than a wavelength, i.e. $p \ll \lambda_0$. Therefore the higher-order Floquet modes are all slow waves. The quasi-uniform LWA radiates from its fundamental Floquet mode, which is a fast wave.

1.4 Proposed Structure of the 2D Periodic Leaky-Wave Antenna

The structure that is proposed and studied here in the present work is shown in Fig. 1.1. It is a 2D periodic leaky wave antenna with a periodic arrangement of patches in a 2D rectangular lattice on the surface of a grounded dielectric. The plasmonic structure that is examined to study the phenomena of directive beaming has a similar geometry with the patches replaced by grooves of the same shape and no ground plane; also the dielectric (silver) has much higher loss than the microwave case, and it has a negative permittivity. The grooves are modeled as conducting patches for the mathematical analyses.

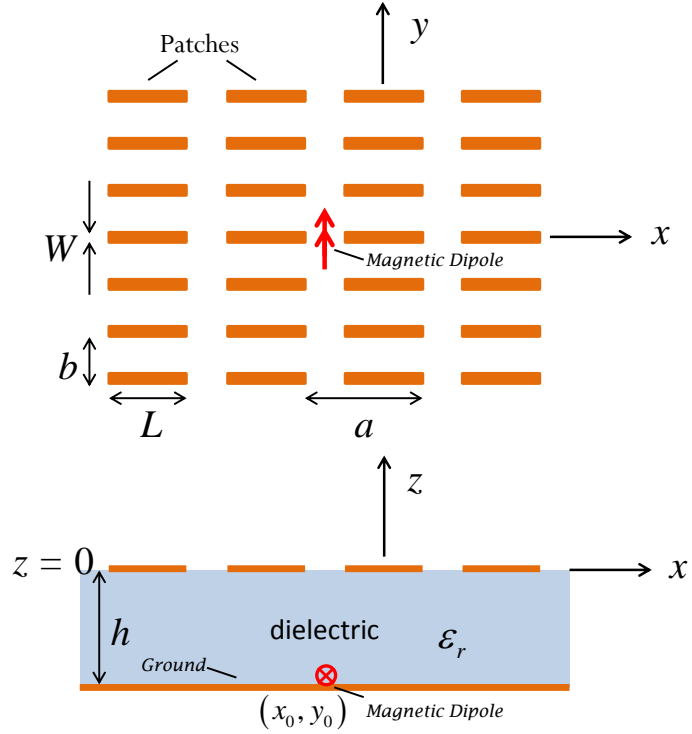


Fig. 1.1. Schematic of the 2D periodic leaky-wave antenna under consideration.

The structure considered here consists of a grounded dielectric slab with a 2D rectangular periodic arrangement of metal patches on the upper surface. The periodicity in the x direction is a and that in the y direction is b . The dimension of the patches in the x direction is L and that in the y direction is W . The height of the dielectric substrate is h and is chosen to be such that only a TM_0 surface wave would propagate when the patches are not present. The relative permittivity of the substrate is ϵ_r . A magnetic dipole source is located at $z = -h_d$, $x = -a/2$, and $y = 0$. For the plasmonic structure at optical frequencies, there is no ground plane and the position of the magnetic dipole is taken to be at the surface of the dielectric slab since the subwavelength aperture is located at the surface of the dielectric, i.e., at $z = 0$.

1.5 Organization of the Dissertation

The present chapter, Chapter 1, “Introduction,” introduces the subject of the dissertation, namely 2D periodic leaky-wave antennas in the microwave and optical regime. It talks about the background and motivation, some of the related work done in this area so far, the general leaky-wave theory, the geometry of the antenna structure under consideration, and the organization of the dissertation.

The next chapter, Chapter 2, “Theoretical Foundation,” goes into the details of the theoretical analyses. It explains in details all the methods of analysis and theoretical approaches with the relevant mathematical formulations, for studying the 2D periodic leaky-wave antenna under consideration. The methods discussed here are (i) the spectral domain immittance method and reciprocity, (ii) the array scanning method, and (iii) CAD formulas for LWAs. This chapter also includes a theoretical discussion of the grating lobes that appear on this type of structure, and their origin.

Chapter 3, titled “Radiation Characteristics of the 2D Periodic Microwave Antenna,” presents some of the radiation properties observed for the 2D periodic leaky-wave antennas, including optimization of the design, radiation patterns, comparison with the CAD formula, the cross-sectional characteristics of the main beam of the pattern, and the variation of the beamwidths and the enhancement factor with the size of the patches. It also presents the bandwidth, figure of merit, and normalized tolerance of the 2D periodic LWA for some cases.

Chapter 4, titled “Properties of the Leaky Wave in the 2D Periodic Microwave Antenna,” investigates the modal analysis and dispersion properties of the 2D periodic

leaky-wave antennas, the characteristics of the radiating leaky mode, and the grating lobes that are observed, and presents some results related to these properties. This chapter also includes a discussion about the radiation efficiency of the antenna along with some results.

In Chapter 5, “Plasmonic Structure – Directive Beaming at Optical Frequencies” the equivalent plasmonic structure is studied using some of the same methods that were used for the 2D periodic leaky-wave antenna, examining the radiation characteristics and modal properties of the 2D plasmonic structure and presenting some results.

Chapter 6 is titled “Summary and Conclusions”, and it summarizes the entire dissertation and provides a number of conclusions drawn from the results presented in Chapters 3, 4, and 5. All the references are provided at the end of the dissertation.

CHAPTER 2 THEORETICAL FOUNDATION

2.1 Nature of the Leaky Waves

When there are no patches present on the surface of the grounded dielectric slab, and the slab is excited by a slot in the ground plane along the y -axis, a surface wave is excited within the slab as shown in Fig. 2.1. The height of the substrate is chosen such that only the TM_0 surface wave is excited in the slab. Therefore, the height of the substrate needs to be below the cutoff of the TE_1 surface-wave mode. The height or thickness of the dielectric slab h , having a relative permittivity ϵ_r , should therefore be restricted as (where λ_0 is the free-space wavelength)

$$h < \frac{\lambda_0/4}{\sqrt{\epsilon_r - 1}}. \quad (2.1)$$

The y -directed slot in the ground plane, which can be modeled as a y -directed magnetic dipole, excites the TM_0 surface wave in the grounded dielectric slab as a cylindrical wave propagating radially outward from the source. So the resulting z -directed electric field distribution due to the surface wave will be of the form

$$E_z^{TM} \propto A_{TM} \cos \phi, \quad (2.2)$$

where A_{TM} is the amplitude of the z -directed electric field. The strength of the surface-wave field launched by the magnetic dipole varies with angle ϕ . Therefore, the surface wave is strongest when propagating along the x -axis ($\phi = 0$) and much weaker along the y -axis ($\phi = 90^\circ$). In Fig. 2.1 the green wedge region around the x -axis represents the region where the surface wave carries the most energy.

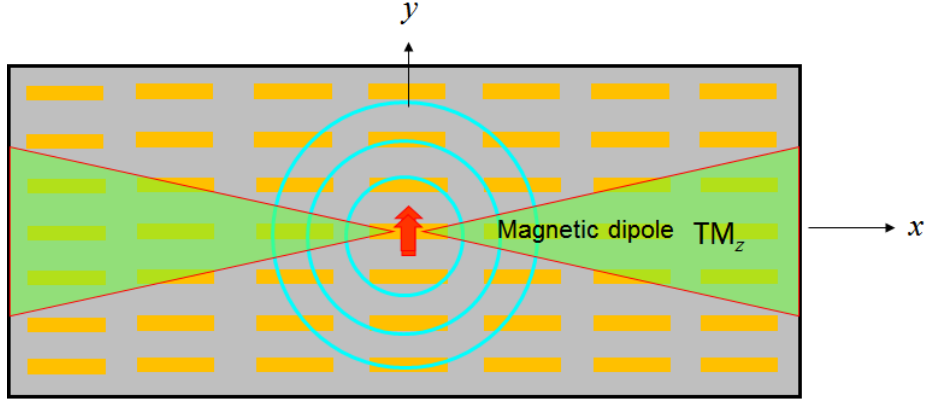


Fig. 2.1. Distribution of the surface-wave field over the 2D periodic leaky-wave antenna structure, when excited by a horizontal magnetic dipole.

When the surface of the grounded dielectric slab has periodic patches present, as in the case of the present structure, the surface wave gets perturbed into an infinite number of spatial harmonics or Floquet waves defined by the wave numbers $k_{xp} = k_{x0} + 2\pi p/a$ and $k_{yq} = k_{y0} + 2\pi q/b$ for the $(p, q)^{\text{th}}$ Floquet harmonic, where k_{x0} and k_{y0} correspond to the $(0, 0)^{\text{th}}$ or the fundamental Floquet harmonic. One or more of these Floquet waves is a fast wave and is thus a leaky wave, and this produces the radiation.

2.2 Far Field Calculation – Spectral Domain Immittance (SDI) with Reciprocity to Analyze the Periodic Leaky-Wave Antenna

Figure 2.2 shows the 2D periodic leaky-wave antenna structure at microwave frequencies with the grounded dielectric slab and metal patches on the upper surface. The magnetic dipole source is located at $(x_0, y_0, -h_d)$ with $h_d = h$ since the magnetic dipole models a slot in the ground plane. A testing dipole is also shown here located at (r, θ, ϕ) , where $r \rightarrow \infty$ since we calculate the radiation in the far-field region. This is used in the reciprocity calculation of the far-field pattern.

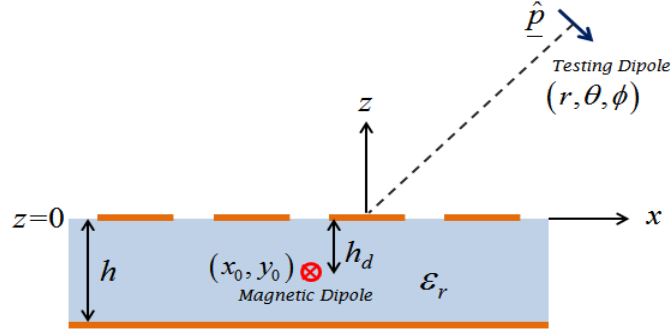


Fig. 2.2. Side view of the 2D periodic leaky-wave antenna for microwave frequencies.

Similarly for the plasmonic structure at optical frequencies, Fig. 2.3 shows the 2D periodic leaky-wave antenna structure with the dielectric slab (silver) and no ground plane, and conducting patches on the upper surface. For the practical optical 2D periodic LWA there are periodic rectangular grooves on the surface of the substrate that are modelled here as conducting patches. The magnetic dipole source is located at $(x_0, y_0, -h_d)$, with $h_d = 0$ since the magnetic dipole models a subwavelength aperture in the dielectric slab. A testing dipole is also shown here located at (r, θ, ϕ) , where $r \rightarrow \infty$ since we calculate the radiation in the far-field region.

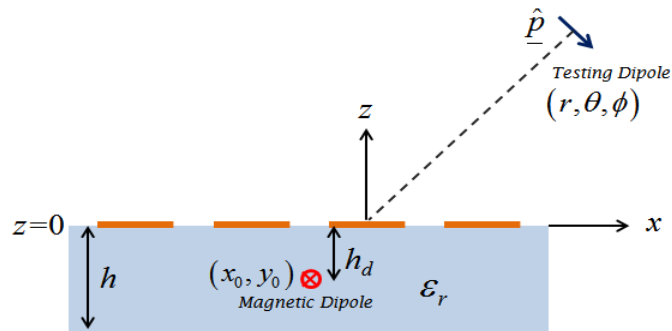


Fig. 2.3. Side view of the 2D periodic leaky-wave antenna for optical frequencies.

The testing dipole is an infinitesimal electric dipole located in the direction of unit vector $\underline{\hat{p}}$, which is $\underline{\hat{\theta}}$ for TM_z polarization and $\underline{\hat{\phi}}$ for TE_z polarization. The incident field from the testing dipole is given by

$$\underline{E}^{inc} = \underline{\hat{p}} \left(-\frac{j\omega\mu}{4\pi r} e^{-jk_0 r} \right) e^{+jk \cdot \underline{r}'}, \quad \underline{\hat{p}} = \underline{\hat{\theta}} \text{ for } \text{TM}_z, \underline{\hat{\phi}} \text{ for } \text{TE}_z. \quad (2.3)$$

Here r is the distance of the testing dipole from the origin, \underline{r}' is the location of the observation point, and the incident wavenumber of the plane wave is

$$\underline{k} = k_x^{pw} \underline{\hat{x}} + k_y^{pw} \underline{\hat{y}} + k_z^{pw} \underline{\hat{z}}, \quad (2.4)$$

where

$$k_x^{pw} = -k_0 \sin \theta \cos \phi = k_{x0}, \quad (2.5)$$

$$k_y^{pw} = -k_0 \sin \theta \sin \phi = k_{y0}, \quad (2.6)$$

and

$$k_z^{pw} = -k_0 \cos \theta = -k_{z0}. \quad (2.7)$$

The total field seen on the surface of the patches is given by

$$\underline{E}^{total} = \underline{E}^{layer} + \underline{E}^{sca}, \quad (2.8)$$

where the “layer” field is that produced in the absence of the patches (i.e., by the layered structure only), and the scattered field is that due to the radiating currents of the patches.

Considering the field in the x -direction,

$$E_x^{layer} = E_x^{inc} (1 + \Gamma), \quad (2.9)$$

where for the microwave structure (Fig. 2.2)

$$\Gamma = \frac{jZ_1 \tan(k_{z_1}h) - Z_0}{jZ_1 \tan(k_{z_1}h) + Z_0}, \quad (2.10)$$

and for the optical structure (Fig. 2.3)

$$\Gamma = \frac{Z_{in} - Z_0}{Z_{in} + Z_0}, \quad Z_{in} = Z_1 \frac{Z_0 + jZ_1 \tan(k_{z_1}h)}{Z_1 + jZ_0 \tan(k_{z_1}h)}. \quad (2.11)$$

The incident field from the testing dipole is scattered by the patches. The scattered field is given by

$$E_x^{sca} = \frac{1}{ab} \sum_{p=-\infty}^{\infty} \sum_{q=-\infty}^{\infty} \tilde{G}_{xx}^{EJ}(k_{xp}, k_{yq}) \tilde{J}_{sx}^P(k_{xp}, k_{yq}) e^{-j(k_{xp}x + k_{yq}y)}, \quad (2.12)$$

where

$$\tilde{G}_{xx}^{EJ}(k_x, k_y) = -\frac{1}{k_t^2} [k_x^2 V^{TM} + k_y^2 V^{TE}] = -\frac{1}{k_t^2} \left[\frac{k_x^2}{D_{TM}(k_x, k_y)} + \frac{k_y^2}{D_{TE}(k_x, k_y)} \right], \quad (2.13)$$

where for the microwave structure

$$D_{TM}(k_x, k_y) = Y_0^{TM} - jY_1^{TM} \cot(k_{z_1}h) \quad (2.14)$$

and

$$D_{TE}(k_x, k_y) = Y_0^{TE} - jY_1^{TE} \cot(k_{z_1}h). \quad (2.15)$$

For the optical structure

$$D_{TM}(k_x, k_y) = Y_0^{TM} + \left(Z_1^{TM} \frac{Z_0^{TM} + jZ_1^{TM} \tan(k_{z_1}h)}{Z_1^{TM} + jZ_0^{TM} \tan(k_{z_1}h)} \right)^{-1} \quad (2.16)$$

and

$$D_{TE}(k_x, k_y) = Y_0^{TE} + \left(Z_1^{TE} \frac{Z_0^{TE} + jZ_1^{TE} \tan(k_{z_1}h)}{Z_1^{TE} + jZ_0^{TE} \tan(k_{z_1}h)} \right)^{-1}. \quad (2.17)$$

The derivation of the Green's function $\tilde{G}_{xx}^{EJ}(k_x, k_y)$ is shown in detail later.

The current on the patches is taken to be in the x -direction and is given by

$$J_{sx}^P(x, y) = \sum_{n=1}^N a_n B_n(x, y) = \sum_{n=1}^N a_n f_n(x) g_n(y), \quad (2.18)$$

where a_n is the coefficient of the n^{th} basis function $B_n(x, y)$ and

$$f_n(x) = \sin\left[\frac{n\pi}{L}\left(x + \frac{L}{2}\right)\right], \quad g_n(y) = \frac{1/\pi}{\sqrt{(W/2)^2 - y^2}}. \quad (2.19)$$

The Fourier Transform of the patch current is then given by

$$\tilde{J}_{sx}^P(k_x, k_y) = \sum_{n=1}^N a_n \tilde{B}_n(k_x, k_y) = \sum_{n=1}^N a_n \tilde{f}_n(k_x) \tilde{g}_n(k_y), \quad (2.20)$$

where

$$\tilde{f}_n(k_x) = \frac{e^{-jk_x L/2} \left(-n\pi L + e^{jk_x L} L(n\pi \cos(n\pi)) \right)}{(k_x L)^2 - (n\pi)^2} \quad (2.21)$$

and

$$\tilde{g}_n(k_y) = J_0(k_y W/2). \quad (2.22)$$

The method of moments is then applied by enforcing the electric field integral equation (EFIE) on the $(0, 0)^{\text{th}}$ patch (assuming it to be a perfect electric conductor) in the x -direction,

$$E_x^{\text{tot}} = E_x^{\text{layer}} + E_x^{\text{sca}} = 0. \quad (2.23)$$

Substituting from Eqs. (2.9) and (2.12), we have

$$E_x^{inc}(1+\Gamma) + \frac{1}{ab} \sum_{p=-\infty}^{\infty} \sum_{q=-\infty}^{\infty} \tilde{G}_{xx}^{EJ}(k_{xp}, k_{yq}) \tilde{J}_{sx}^P(k_{xp}, k_{yq}) e^{-j(k_{xp}x + k_{yq}y)} = 0. \quad (2.24)$$

Applying Galerkin's method and taking the testing function to have the same form as the basis function, we have

$$\begin{aligned} \int_{-w/2}^{w/2} \int_{-L/2}^{L/2} \frac{1}{ab} \sum_{p=-\infty}^{\infty} \sum_{q=-\infty}^{\infty} \tilde{G}_{xx}^{EJ}(k_{xp}, k_{yq}) \tilde{J}_{sx}^P(k_{xp}, k_{yq}) B_m(x, y) e^{-j(k_{xp}x + k_{yq}y)} dx dy \\ = - \int_{-w/2}^{w/2} \int_{-L/2}^{L/2} E_x^{inc}(x, y, 0) (1+\Gamma) B_m(x, y) dx dy. \end{aligned} \quad (2.25)$$

Replacing $\tilde{J}_{sx}^P(k_{xp}, k_{yq})$ from Eq. (2.20) and $E_x^{inc}(x, y, 0)$ from above, we have

$$\begin{aligned} \int_{-w/2}^{w/2} \int_{-L/2}^{L/2} \frac{1}{ab} \sum_{p=-\infty}^{\infty} \sum_{q=-\infty}^{\infty} \tilde{G}_{xx}^{EJ}(k_{xp}, k_{yq}) \sum_{n=1}^N a_n \tilde{B}_n(k_{xp}, k_{yq}) B_m(x, y) e^{-j(k_{xp}x + k_{yq}y)} dx dy \\ = - \int_{-w/2}^{w/2} \int_{-L/2}^{L/2} E_x^{inc}(0, 0, 0) e^{-j(k_{x0}x + k_{y0}y)} (1+\Gamma) B_m(x, y) dx dy \end{aligned} \quad (2.26)$$

or

$$\begin{aligned} \sum_{n=1}^N a_n \frac{1}{ab} \sum_{p=-\infty}^{\infty} \sum_{q=-\infty}^{\infty} \tilde{G}_{xx}^{EJ}(k_{xp}, k_{yq}) \tilde{B}_n(k_{xp}, k_{yq}) \tilde{B}_m(-k_{xp}, -k_{yq}) \\ = -E_x^{inc}(0, 0, 0) (1+\Gamma) \tilde{B}_m(-k_{x0}, -k_{y0}). \end{aligned} \quad (2.27)$$

The matrix form of the above EFIE relation is

$$[Z_{mn}][a_n] = [R_m], \quad (2.28)$$

where

$$Z_{mn} = \frac{1}{ab} \sum_{p=-\infty}^{\infty} \sum_{q=-\infty}^{\infty} \tilde{G}_{xx}^{EJ}(k_{xp}, k_{yq}) \tilde{B}_n(k_{xp}, k_{yq}) \tilde{B}_m(-k_{xp}, -k_{yq}) e^{-jk_{zpq} \Delta z}. \quad (2.29)$$

Here Δz denotes the z -displacement between the current on the patches and the testing function, and

$$R_m = -E_x^{inc}(0,0,0)(1+\Gamma)\tilde{B}_m(-k_{x0}, -k_{y0}). \quad (2.30)$$

The z -displacement Δz is added for easier convergence of the infinite summations in p and q and makes the computations easier. It can be thought of as accounting for the thickness of the conductor patches. Unless otherwise specified, the z -displacement has been applied in all numerically generated theoretical results presented in later chapters, and it is taken to be $\Delta z = 0.01a$. The above matrix equation is then solved for the coefficients of the basis function, a_n . Using reciprocity, the electric field in the far-field region is then calculated as

$$E_i^{FF}(r, \theta, \phi) = H_y(x_0, y_0, -h_d) = H_y(-a/2, 0, -h_d) \quad (2.31)$$

or

$$E_i^{FF}(r, \theta, \phi) = E_x^{inc}\left(-\frac{1}{Z_0}\right)(1-\Gamma)\left\{\frac{e^{-jk_{z1}^{pw}h_d}(1-\Gamma_1e^{-j2k_{z1}^{pw}(h-h_d)})}{(1-\Gamma_1e^{-j2k_{z1}^{pw}h})}\right\}e^{-j(k_{x0}x_0+k_{y0}y_0)} \\ + \frac{1}{ab}\sum_{n=1}^N a_n \sum_{p=-\infty}^{\infty} \sum_{q=-\infty}^{\infty} \tilde{G}_{yx}^{HJ}(k_{xp}, k_{yq})\tilde{B}_n(k_{xp}, k_{yq})e^{-j(k_{xp}x_0+k_{yq}y_0)}. \quad (2.32)$$

Here $x_0 = -a/2$, $y_0 = 0$, $z_0 = -h_d$, and $i = \theta$ for TM, ϕ for TE polarization. The Green's function $\tilde{G}_{yx}^{HJ}(k_x, k_y)$ is given by (the derivation is given later)

$$\tilde{G}_{yx}^{HJ}(k_x, k_y) = -\frac{1}{k_t^2}\left[k_x^2 I_i^{TM}(-h_d) + k_y^2 I_i^{TE}(-h_d)\right]. \quad (2.33)$$

Case I

This case is when $h_d = 0$, i.e. the magnetic dipole source is located at the surface of the dielectric. The transverse equivalent network (TEN) model is used to find the Green's function, and is shown in Fig. 2.4.

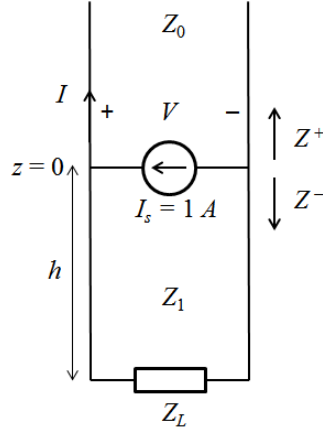


Fig. 2.4. TEN model for the LWA structure with the patch currents as the source.

In Fig. 2.4 above, $Z_L = Z_0$ for the optical case (no ground plane) and $Z_L = 0$ for the microwave case (PEC ground plane). Consider the impedances above and below the source in Fig. 2.4,

$$Z^+ = Z_0, \quad Z^- = Z_1 \frac{Z_L + jZ_1 \tan(k_{z1}h)}{Z_1 + jZ_L \tan(k_{z1}h)}. \quad (2.34)$$

Using the current divider rule, the current right above the surface of the dielectric at $z = 0$ is

$$I_i(0^+) = \frac{Z^-}{Z^+ + Z^-}. \quad (2.35)$$

Again using the current divider rule, the current right below the surface of the dielectric at $z = 0$ is

$$I_i(0^-) = -\frac{Z^+}{Z^+ + Z^-}. \quad (2.36)$$

At the location of the dipole,

$$I_i(0) = I_i(0^+) = I_i(0^-). \quad (2.37)$$

Case II

This case is when $0 < h_d \leq h$, i.e., the magnetic dipole source is inside the dielectric slab, below the patches. In this case we have

$$I_i(-h_d) = I_i(0) \frac{e^{-jk_{z1}^{pw} h_d} \left(1 - \Gamma_1 e^{-j2k_{z1}^{pw} (h-h_d)}\right)}{\left(1 - \Gamma_1 e^{-j2k_{z1}^{pw} h}\right)}, \quad \Gamma_1 = \frac{Z_L - Z_1}{Z_L + Z_1}. \quad (2.38)$$

For the microwave case, $\Gamma_1 = -1$ and the above expression reduces to

$$I_i(-h_d) = I_i(0) \frac{\cos(k_{z1}^{pw} (h-h_d))}{\cos(k_{z1}^{pw} h)}. \quad (2.39)$$

Derivation of the Green's Functions $\tilde{G}_{xx}^{EJ}(k_x, k_y)$, $\tilde{G}_{yx}^{HJ}(k_x, k_y)$

A spectral-domain transverse equivalent network is used to formulate the Green's functions. We define the transverse component of the wavenumber as

$$\underline{k}_t = \underline{\hat{x}}k_x + \underline{\hat{y}}k_y. \quad (2.40)$$

In Fig. 2.5 the vectors $\underline{\hat{u}}$ and $\underline{\hat{v}}$ are shown in the transverse, i.e., x - y plane, and are defined in Fig. 2.5.

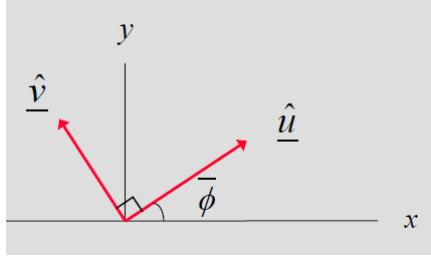


Fig. 2.5. The orientation of the vectors $\underline{\hat{u}}$ and $\underline{\hat{v}}$ with respect to the x and y axes.

We then have

$$\underline{\hat{u}} = \underline{k}_t / k_t, \quad (2.41)$$

$$\underline{\hat{v}} = \underline{\hat{z}} \times \underline{\hat{u}} \quad \text{or,} \quad \underline{\hat{u}} \times \underline{\hat{v}} = \underline{\hat{z}}, \quad (2.42)$$

$$\underline{\hat{u}} \cdot \underline{\hat{x}} = \cos \bar{\phi} = \frac{k_x}{k_t}, \quad (2.43)$$

$$\underline{\hat{v}} \cdot \underline{\hat{x}} = -\sin \bar{\phi} = -\frac{k_y}{k_t}, \quad (2.44)$$

$$\underline{\hat{u}} \cdot \underline{\hat{y}} = \sin \bar{\phi} = \frac{k_y}{k_t}, \quad (2.45)$$

and
$$\underline{\hat{v}} \cdot \underline{\hat{y}} = \cos \bar{\phi} = \frac{k_x}{k_t}. \quad (2.46)$$

Considering the components of the surface current $\underline{\tilde{J}}_s$ at an interface (with the same material on either side) as shown in Fig. 2.6, $\underline{\tilde{J}}_{su}$ launches a TM_z wave and $\underline{\tilde{J}}_{sv}$ launches a TE_z wave. The fields of the TM_z and TE_z polarizations launched by these components

of the surface current are as follows: for $TM_z: \tilde{J}_{su} \Rightarrow \tilde{E}_u$ and \tilde{H}_v , and for $TE_z: \tilde{J}_{sv} \Rightarrow \tilde{E}_v$ and \tilde{H}_u . The transverse magnetic field \tilde{H}_t^+ above and the transverse magnetic field \tilde{H}_t^- below the surface of dielectric shown in Fig. 2.6 are equal and opposite due to symmetry and are related to the surface current as

$$\tilde{H}_t^+ = -\frac{1}{2} \hat{z} \times \tilde{J}_s. \quad (2.47)$$

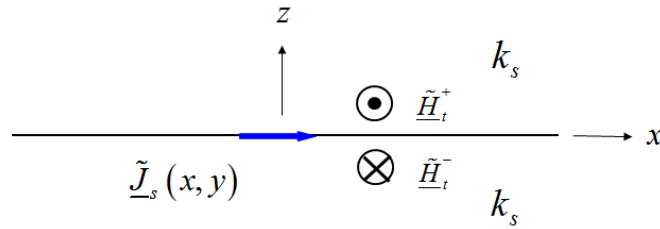


Fig. 2.6. The surface current \tilde{J}_s and the magnetic fields it produces at the surface.

Using the usual TEN convention, the transverse electric and magnetic fields are modeled as voltages and currents as given below.

$$\begin{array}{ll} TM_z: & V^{TM} \rightarrow \tilde{E}_u \\ & I^{TM} \rightarrow \tilde{H}_v \end{array} \quad \begin{array}{ll} TE_z: & V^{TE} \rightarrow -\tilde{E}_v \\ & I^{TE} \rightarrow \tilde{H}_u. \end{array}$$

In Fig. 2.4, the impedances for the TM_z and TE_z components in the medium are denoted by i (0 for air or free space, 1 for dielectric) and are given as

$$Z_i^{TM} = \frac{k_{zi}}{\omega \epsilon_i} \quad (2.48)$$

and

$$Z_i^{TE} = \frac{\omega \mu_i}{k_{zi}}. \quad (2.49)$$

From the boundary conditions,

$$\hat{\underline{z}} \times (\tilde{\underline{H}}_t^+ - \tilde{\underline{H}}_t^-) = \tilde{\underline{J}}_s, \quad (2.50)$$

where $\tilde{\underline{H}}_t^+$ is the transverse magnetic field above the interface and $\tilde{\underline{H}}_t^-$ is the transverse magnetic field below the interface. For the TM_z field, we have

$$\hat{\underline{z}} \times [\hat{\underline{v}} (\tilde{\underline{H}}_v^+ - \tilde{\underline{H}}_v^-)] = \hat{\underline{u}} \tilde{\underline{J}}_{su}, \quad (2.51)$$

$$\Rightarrow -\hat{\underline{u}} (\tilde{\underline{H}}_v^+ - \tilde{\underline{H}}_v^-) = \hat{\underline{u}} \tilde{\underline{J}}_{su}, \quad (2.52)$$

$$\Rightarrow \tilde{\underline{H}}_v^+ - \tilde{\underline{H}}_v^- = -\tilde{\underline{J}}_{su}, \quad (2.53)$$

$$\Rightarrow I^{TM+} - I^{TM-} = -\tilde{\underline{J}}_{su}. \quad (2.54)$$

Similarly, for the TE_z mode,

$$\hat{\underline{z}} \times [\hat{\underline{u}} (\tilde{\underline{H}}_u^+ - \tilde{\underline{H}}_u^-)] = \hat{\underline{v}} \tilde{\underline{J}}_{sv}, \quad (2.55)$$

$$\Rightarrow \tilde{\underline{H}}_u^+ - \tilde{\underline{H}}_u^- = \tilde{\underline{J}}_{sv}, \quad (2.56)$$

$$\Rightarrow I^{TE+} - I^{TE-} = \tilde{\underline{J}}_{sv}. \quad (2.57)$$

Also from the boundary conditions,

$$\hat{\underline{z}} \times (\tilde{\underline{E}}_t^+ - \tilde{\underline{E}}_t^-) = \underline{0}, \quad (2.58)$$

$$\Rightarrow \tilde{\underline{E}}_u^+ = \tilde{\underline{E}}_u^-, \quad \tilde{\underline{E}}_v^+ = \tilde{\underline{E}}_v^-, \quad (2.59)$$

$$\Rightarrow V^{TM+} = V^{TM-}, \quad V^{TE+} = V^{TE-}. \quad (2.60)$$

The electric surface current density is modeled as a parallel current source in the TEN model as shown in Fig. 2.4. The current source in the TEN model is

$$I_S^{TM} = -\tilde{\mathbf{J}}_{su}, \quad I_S^{TE} = \tilde{\mathbf{J}}_{sv}. \quad (2.61)$$

The normalized voltage and current functions then represent the fields following the usual convention of the TEN model, as

$$\begin{aligned} V^{TM} &= V_i^{TM} \left(-\tilde{\mathbf{J}}_{s0} \cdot \hat{\mathbf{u}} \right) \rightarrow \tilde{E}_u, \\ I^{TM} &= I_i^{TM} \left(-\tilde{\mathbf{J}}_{s0} \cdot \hat{\mathbf{u}} \right) \rightarrow \tilde{H}_v, \\ V^{TE} &= V_i^{TE} \left(\tilde{\mathbf{J}}_{s0} \cdot \hat{\mathbf{v}} \right) \rightarrow -\tilde{E}_v, \text{ and} \\ I^{TE} &= I_i^{TE} \left(\tilde{\mathbf{J}}_{s0} \cdot \hat{\mathbf{v}} \right) \rightarrow \tilde{H}_u, \end{aligned}$$

where V_i^{TM} and V_i^{TE} are the voltages due to a unit amplitude parallel current source, and I_i^{TM} and I_i^{TE} are the currents due to a unit amplitude parallel current source at the source location. The spectral-domain electric field \tilde{E}_x due to a the spectral-domain surface current $\tilde{\mathbf{J}}_{s0}$ is given by

$$\tilde{E}_x = \tilde{E}_u (\hat{\mathbf{u}} \cdot \hat{\mathbf{x}}) + \tilde{E}_v (\hat{\mathbf{v}} \cdot \hat{\mathbf{x}}), \quad (2.62)$$

$$\Rightarrow \tilde{E}_x = \tilde{E}_u \frac{k_x}{k_t} + \tilde{E}_v \left(-\frac{k_y}{k_t} \right), \quad (2.63)$$

$$\Rightarrow \tilde{E}_x = \left[V^{TM} \frac{k_x}{k_t} - V^{TE} \left(-\frac{k_y}{k_t} \right) \right] e^{-j(k_x x + k_y y)}, \quad (2.64)$$

$$\Rightarrow \tilde{E}_x = \left[V_i^{TM} \left(-\tilde{\mathbf{J}}_{s0} \cdot \hat{\mathbf{u}} \right) \frac{k_x}{k_t} - V_i^{TE} \left(\tilde{\mathbf{J}}_{s0} \cdot \hat{\mathbf{v}} \right) \left(-\frac{k_y}{k_t} \right) \right] e^{-j(k_x x + k_y y)}, \quad (2.65)$$

$$\Rightarrow \tilde{E}_x = \left[V_i^{TM} \left(-\tilde{\mathbf{J}}_{sx0} \cdot \hat{\mathbf{x}} \cdot \hat{\mathbf{u}} \right) \frac{k_x}{k_t} + V_i^{TE} \left(\tilde{\mathbf{J}}_{sx0} \cdot \hat{\mathbf{x}} \cdot \hat{\mathbf{v}} \right) \frac{k_y}{k_t} \right] e^{-j(k_x x + k_y y)}, \quad (2.66)$$

$$\Rightarrow \quad \tilde{E}_x = \left[V_i^{TM} \tilde{J}_{sx0} \left(-\frac{k_x}{k_t} \right) \frac{k_x}{k_t} + V_i^{TE} \tilde{J}_{sx0} \left(-\frac{k_y}{k_t} \right) \frac{k_y}{k_t} \right] e^{-j(k_x x + k_y y)}, \quad (2.67)$$

$$\Rightarrow \quad \tilde{E}_x = -\frac{1}{k_t^2} \left[V_i^{TM} k_x^2 + V_i^{TE} k_y^2 \right] \tilde{J}_{sx0} e^{-j(k_x x + k_y y)}. \quad (2.68)$$

Therefore, the Green's function is

$$\tilde{G}_{xx}^{EJ}(k_x, k_y, z) = -\frac{1}{k_t^2} \left[k_x^2 V_i^{TM}(z) + k_y^2 V_i^{TE}(z) \right]. \quad (2.69)$$

From the TEN model of the layers, represented in Fig. 2.4, the voltages $V_i^{TM}(z)$ and $V_i^{TE}(z)$ for $z = 0$ (i.e., at the surface of the dielectric) can be calculated as

$$V_i(0) = I_s \left(\frac{1}{Z^+} + \frac{1}{Z^-} \right)^{-1} = \frac{1}{\left(\frac{1}{Z^+} + \frac{1}{Z^-} \right)} = \frac{1}{D}. \quad (2.70)$$

where, substituting from Eq. (2.34),

$$D = \left(\frac{1}{Z^+} + \frac{1}{Z^-} \right) = Y_0 + \left(Z_1 \frac{Z_L + jZ_1 \tan(k_{z1}h)}{Z_1 + jZ_L \tan(k_{z1}h)} \right)^{-1}. \quad (2.71)$$

Therefore,

$$V_i^{TM}(0) = D_{TM}(k_x, k_y) = Y_0^{TM} + \left(Z_1^{TM} \frac{Z_L^{TM} + jZ_1^{TM} \tan(k_{z1}h)}{Z_1^{TM} + jZ_L^{TM} \tan(k_{z1}h)} \right)^{-1} \quad (2.72)$$

and

$$V_i^{TE}(0) = D_{TE}(k_x, k_y) = Y_0^{TE} + \left(Z_1^{TE} \frac{Z_L^{TE} + jZ_1^{TE} \tan(k_{z1}h)}{Z_1^{TE} + jZ_L^{TE} \tan(k_{z1}h)} \right)^{-1}. \quad (2.73)$$

The spectral-domain magnetic field \tilde{H}_y due to a particular spatial harmonic of the surface current \tilde{J}_{s0} is given by

$$\tilde{H}_y = \tilde{H}_u (\hat{u} \cdot \hat{y}) + \tilde{H}_v (\hat{v} \cdot \hat{y}), \quad (2.74)$$

$$\Rightarrow \tilde{H}_y = \tilde{H}_u \frac{k_y}{k_t} + \tilde{H}_v \frac{k_x}{k_t}, \quad (2.75)$$

$$\Rightarrow \tilde{H}_y = \left[I^{TE} \frac{k_y}{k_t} + I^{TM} \frac{k_x}{k_t} \right] e^{-j(k_x x + k_y y)}, \quad (2.76)$$

$$\Rightarrow \tilde{H}_y = \left[I_i^{TE} (\tilde{J}_{s0} \cdot \hat{v}) \frac{k_y}{k_t} + I_i^{TM} (-\tilde{J}_{s0} \cdot \hat{u}) \frac{k_x}{k_t} \right] e^{-j(k_x x + k_y y)}, \quad (2.77)$$

$$\Rightarrow \tilde{H}_y = \left[I_i^{TE} (\tilde{J}_{sx0} \hat{x} \cdot \hat{v}) \frac{k_y}{k_t} + I_i^{TM} (-\tilde{J}_{sx0} \hat{x} \cdot \hat{u}) \frac{k_x}{k_t} \right] e^{-j(k_x x + k_y y)}, \quad (2.78)$$

$$\Rightarrow \tilde{H}_y = \left[I_i^{TE} \tilde{J}_{sx0} \left(-\frac{k_y}{k_t} \right) \frac{k_y}{k_t} + I_i^{TM} \tilde{J}_{sx0} \left(-\frac{k_x}{k_t} \right) \frac{k_x}{k_t} \right] e^{-j(k_x x + k_y y)}, \quad (2.79)$$

$$\Rightarrow \tilde{H}_y = -\frac{1}{k_t^2} \left[I_i^{TE} k_y^2 + I_i^{TM} k_x^2 \right] \tilde{J}_{sx0} e^{-j(k_x x + k_y y)}. \quad (2.80)$$

Therefore, the Green's function for this field is

$$\tilde{G}_{yx}^{HI} (k_x, k_y, z) = -\frac{1}{k_t^2} \left[k_x^2 I_i^{TM} (z) + k_y^2 I_i^{TE} (z) \right]. \quad (2.81)$$

For the reciprocity calculations, the source magnetic dipole is always assumed to be of unit amplitude with zero phase. The distance between the magnetic source dipole and the testing dipole does not affect the final result, as the radiation pattern is usually normalized, and it is taken to be unity at the maximum.

2.3 Current Distribution and Near Field Calculation – Using the Array Scanning Method for the Currents on the Patches of the 2D Periodic LWA Structure

A section of the 2D periodic leaky-wave antenna with the patches on the surface of a grounded dielectric substrate is shown in Fig. 2.7. In applying the array scanning method to calculate near-field quantities, the single magnetic dipole at the center of the structure is first replaced by an array of phased current sources with the same spatial periodicity as the patches, as shown in Fig. 2.8. Then the near field parameter of interest for this set-up is determined, and from this the corresponding near field parameter for the single source in the original structure is determined as detailed below.

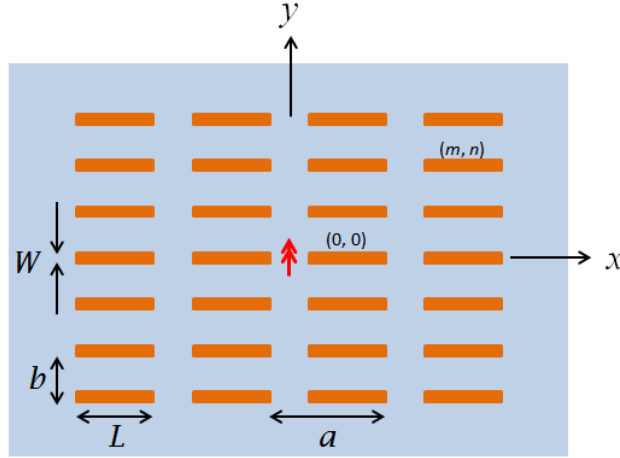


Fig. 2.7. The 2D periodic leaky-wave antenna.

The current amplitude at the center of the patch for the $(m, n)^{\text{th}}$ patch in the 2D periodic LWA structure is given by

$$\begin{aligned}
 A_{mn} &= \frac{ab}{(2\pi)^2} \int_{-\pi/b}^{\pi/b} \int_{-\pi/a}^{\pi/a} A_{mn}^{\infty}(k_{x0}, k_{y0}) dk_{x0} dk_{y0} \\
 &= \frac{ab}{(2\pi)^2} \int_{-\pi/b}^{\pi/b} \int_{-\pi/a}^{\pi/a} A_{00}^{\infty}(k_{x0}, k_{y0}) e^{-j(k_{x0}ma + k_{y0}nb)} dk_{x0} dk_{y0},
 \end{aligned} \tag{2.82}$$

where $A_{mn}^\infty(k_{x0}, k_{y0})$ denotes the amplitude of the current at the center of the $(m, n)^{\text{th}}$ patch for the structure with the infinite number of phased sources.

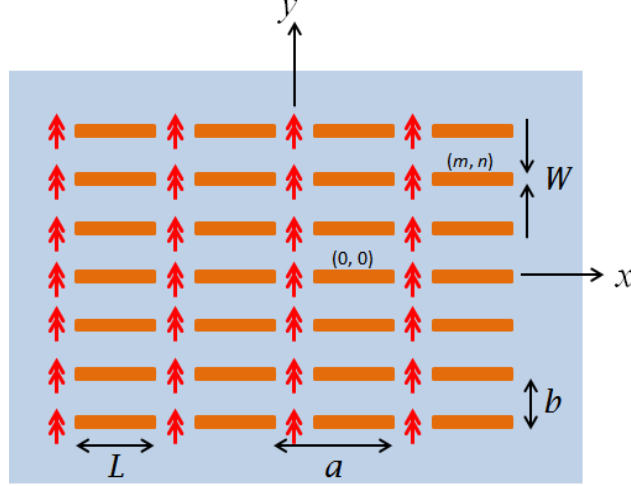


Fig. 2.8. A single source is replaced by infinite array of sources in the ASM calculation.

The current density distribution on the patch surface, when there is an infinite phased array of magnetic dipole sources along with the infinite array of patches, is taken to be

$$J_{xx}^\infty(x, y) = \sum_{l=1}^{N_b} a_l f_l(x) g(y) = \sum_{l=1}^{N_b} a_l B_l(x, y), \quad (2.83)$$

where

$$f_l(x) = \sin\left[\frac{l\pi}{L}\left(x + \frac{L}{2}\right)\right], \quad g(y) = \frac{1/\pi}{\sqrt{(W/2)^2 - y^2}}. \quad (2.84)$$

The Fourier transforms are given by

$$\tilde{f}_l(k_x) = \frac{e^{-j(k_x L/2)} \left[-l\pi L + e^{jk_x L} L(l\pi \cos(l\pi)) \right]}{(k_x L)^2 - (l\pi)^2}, \quad \tilde{g}(k_y) = J_0(k_y W/2). \quad (2.85)$$

The current amplitude on the $(0, 0)^{\text{th}}$ patch in the infinite-dipole phased array set-up is

$$A_{00}^{\infty}(k_{x0}, k_{y0}) = \sum_{l=1}^{N_b} a_l f_l(0). \quad (2.86)$$

The 2D periodic leaky-wave antenna geometry and configuration are the same as shown in Fig. 2.2 (or Fig. 2.9) and Fig. 2.3 for the microwave case and optical frequency case, respectively.

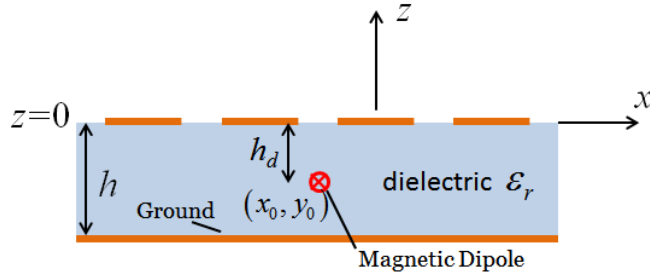


Fig. 2.9. Side view of the 2D periodic leaky-wave antenna for the microwave case.

In the method of moments the EFIE is applied on the surface of the $(0, 0)^{\text{th}}$ patch, enforcing

$$\underline{E}^{layer, \infty} + \underline{E}^{sca, \infty} = 0 \quad \Rightarrow \quad \underline{E}^{layer, \infty} = -\underline{E}^{sca, \infty}. \quad (2.87)$$

Here, $\underline{E}^{layer, \infty}$ is the electric field at the surface of the dielectric slab if there were no patches present and $\underline{E}^{sca, \infty}$ is that due to the current on the patches. The ∞ superscript denotes the incident and scattered field due to the infinite number of dipole sources. The current on the patch array is taken to be x -directed. Therefore, the EFIE is enforced on the electric field in the x -direction as

$$E_x^{sca, \infty} = -E_x^{layer, \infty}. \quad (2.88)$$

The x -component of the scattered field due to the patches can be obtained from the current distribution and is given by

$$E_x^{sca,\infty} = \frac{1}{ab} \sum_{p=-\infty}^{\infty} \sum_{q=-\infty}^{\infty} \tilde{G}_{xx}^{EJ}(k_{xp}, k_{yq}) \tilde{J}_{sx}^{\infty}(k_{xp}, k_{yq}) e^{-j(k_{xp}x + k_{yq}y)}, \quad (2.89)$$

where the Green's function in this case is given by

$$\tilde{G}_{xx}^{EJ}(k_x, k_y) = -\frac{1}{k_t^2} \left[\frac{k_x^2}{D_{TM}(k_t)} + \frac{k_y^2}{D_{TE}(k_t)} \right]. \quad (2.90)$$

The derivation of the above Green's function is the same as was done before for the far-field radiation pattern calculation in the previous section. For the microwave case

$$D_{TM}(k_x, k_y) = Y_0^{TM} - jY_1^{TM} \cot(k_{z1}h) \quad (2.91)$$

and

$$D_{TE}(k_x, k_y) = Y_0^{TE} - jY_1^{TE} \cot(k_{z1}h). \quad (2.92)$$

For the optical case

$$D_{TM}(k_x, k_y) = Y_0^{TM} + \left(Z_1^{TM} \frac{Z_0^{TM} + jZ_1^{TM} \tan(k_{z1}h)}{Z_1^{TM} + jZ_0^{TM} \tan(k_{z1}h)} \right)^{-1} \quad (2.93)$$

and

$$D_{TE}(k_x, k_y) = Y_0^{TE} + \left(Z_1^{TE} \frac{Z_0^{TE} + jZ_1^{TE} \tan(k_{z1}h)}{Z_1^{TE} + jZ_0^{TE} \tan(k_{z1}h)} \right)^{-1}. \quad (2.94)$$

The incident field from the infinite number of phased dipole sources can be calculated from the dipole currents using the TEN model. The surface current density for a single infinitesimal magnetic dipole located at $z = -h_d$, $x = -a/2$, $y = 0$ can be represented as

$$M_{sy}^{dip}(x, y) = \delta(x + a/2)\delta(y - 0). \quad (2.95)$$

The Fourier transform is

$$\tilde{M}_{sy}^{dip}(k_x, k_y) = e^{-j(a/2)k_x}. \quad (2.96)$$

The surface current density distribution from the infinite number of phased dipole sources at $z = -h_d$ is

$$M_{sy}^{dip,\infty}(x, y) = \sum_{m=-\infty}^{\infty} \sum_{n=-\infty}^{\infty} \delta(x - ma + a/2)\delta(y - nb)e^{-j(k_{x0}x + k_{y0}y)}. \quad (2.97)$$

In the spectral domain, the component of the magnetic current \tilde{M}_s^{dip} at the source \tilde{M}_{su}^{dip} launches a TE_z wave, and the component \tilde{M}_{sv}^{dip} launches a TM_z wave. The fields of the TM_z and TE_z polarizations launched by these components of the surface current are as follows: for TM_z : $\tilde{M}_{sv}^{dip} \Rightarrow \tilde{E}_u$ and \tilde{H}_v and for TE_z : $\tilde{M}_{su}^{dip} \Rightarrow \tilde{E}_v$ and \tilde{H}_u . The transverse electric field \tilde{E}_t^+ above and \tilde{E}_t^- below the source magnetic surface current density \tilde{M}_s^{dip} are equal and opposite due to symmetry, and are related to the magnetic surface current density as

$$\tilde{E}_t^+ = \frac{1}{2} \hat{z} \times \tilde{M}_s^{dip}. \quad (2.98)$$

Using the usual TEN convention, the fields are modeled as voltage and current as

$$\begin{array}{ll} TM_z : & V^{TM} \rightarrow \tilde{E}_u \\ & I^{TM} \rightarrow \tilde{H}_v \end{array} \qquad \begin{array}{ll} TE_z : & V^{TE} \rightarrow -\tilde{E}_v \\ & I^{TE} \rightarrow \tilde{H}_u. \end{array}$$

From the boundary conditions, the spectral-domain magnetic surface current $\underline{\tilde{M}}_s^{dip}$ and the corresponding fields are related as,

$$\hat{\underline{z}} \times (\underline{\tilde{E}}_t^+ - \underline{\tilde{E}}_t^-) = -\underline{\tilde{M}}_s^{dip}, \quad (2.99)$$

where $\underline{\tilde{E}}_t^+$ is the transverse electric field above the magnetic surface current and $\underline{\tilde{E}}_t^-$ is the transverse electric field below the magnetic surface current. For the TE_z field,

$$\hat{\underline{z}} \times [\hat{\underline{v}} (\underline{\tilde{E}}_v^+ - \underline{\tilde{E}}_v^-)] = -\hat{\underline{u}} \underline{\tilde{M}}_{su}^{dip}, \quad (2.100)$$

$$\Rightarrow -\hat{\underline{u}} (\underline{\tilde{E}}_v^+ - \underline{\tilde{E}}_v^-) = -\hat{\underline{u}} \underline{\tilde{M}}_{su}^{dip}, \quad (2.101)$$

$$\Rightarrow \underline{\tilde{E}}_v^+ - \underline{\tilde{E}}_v^- = \underline{\tilde{M}}_{su}^{dip}, \quad (2.102)$$

$$\Rightarrow V^{TE+} - V^{TE-} = -\underline{\tilde{M}}_{su}^{dip}. \quad (2.103)$$

Similarly, for the TM_z field,

$$\hat{\underline{z}} \times [\hat{\underline{u}} (\underline{\tilde{E}}_u^+ - \underline{\tilde{E}}_u^-)] = -\hat{\underline{v}} \underline{\tilde{M}}_{sv}^{dip}, \quad (2.104)$$

$$\Rightarrow \underline{\tilde{E}}_u^+ - \underline{\tilde{E}}_u^- = -\underline{\tilde{M}}_{sv}^{dip}, \quad (2.105)$$

$$\Rightarrow V^{TM+} - V^{TM-} = -\underline{\tilde{M}}_{sv}^{dip}. \quad (2.106)$$

Also, from boundary conditions,

$$\hat{\underline{z}} \times (\underline{\tilde{H}}_t^+ - \underline{\tilde{H}}_t^-) = \underline{0}, \quad (2.107)$$

$$\Rightarrow \underline{\tilde{H}}_u^+ = \underline{\tilde{H}}_u^-, \quad \underline{\tilde{H}}_v^+ = \underline{\tilde{H}}_v^-, \quad (2.108)$$

$$\Rightarrow I^{TM+} = I^{TM-}, \quad I^{TE+} = I^{TE-}. \quad (2.109)$$

In the TEN model, the magnetic current sheet is modeled as a voltage source as shown in Fig. 2.10. The spectral domain magnetic surface current density $\tilde{\underline{M}}_s^{dip}$ is modeled as a current source in the TEN model as

$$V_S^{TM} = -\tilde{M}_{sv}^{dip}, \quad V_S^{TE} = -\tilde{M}_{su}^{dip}. \quad (2.110)$$

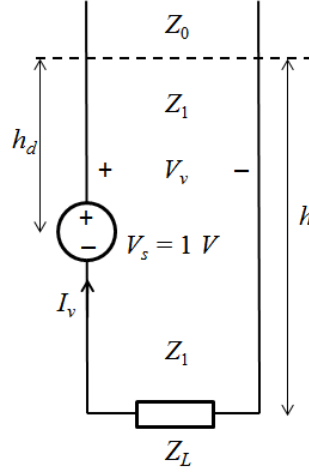


Fig. 2.10. The TEN model for the layers of the LWA with the series voltage source (magnetic dipole).

The normalized voltage and current functions then represent the fields following the usual convention of the TEN model, as

$$\begin{aligned} V^{TM} &= V_v^{TM} \left(-\tilde{\underline{M}}_{s0}^{dp} \cdot \hat{\underline{v}} \right) \rightarrow \tilde{E}_u, \\ I^{TM} &= I_v^{TM} \left(-\tilde{\underline{M}}_{s0}^{dp} \cdot \hat{\underline{v}} \right) \rightarrow \tilde{H}_v, \\ V^{TE} &= V_v^{TE} \left(-\tilde{\underline{M}}_{s0}^{dp} \cdot \hat{\underline{u}} \right) \rightarrow -\tilde{E}_v, \text{ and} \\ I^{TE} &= I_v^{TE} \left(-\tilde{\underline{M}}_{s0}^{dp} \cdot \hat{\underline{u}} \right) \rightarrow \tilde{H}_u, \end{aligned}$$

where V_v^{TM} and V_v^{TE} are the voltages due to an unit amplitude series voltage source in the TEN model, and I_v^{TM} and I_v^{TE} are the currents due to an unit amplitude series voltage

source in the TEN model at the source location. The spectral-domain electric field due to a the magnetic surface current $\tilde{\underline{M}}_{s0}^{dip}$ is given by

$$\tilde{\underline{E}}_x = \tilde{\underline{E}}_u (\hat{\underline{u}} \cdot \hat{\underline{x}}) + \tilde{\underline{E}}_v (\hat{\underline{v}} \cdot \hat{\underline{x}}), \quad (2.111)$$

$$\Rightarrow \tilde{\underline{E}}_x = \tilde{\underline{E}}_u \frac{k_x}{k_t} + \tilde{\underline{E}}_v \left(-\frac{k_y}{k_t} \right), \quad (2.112)$$

$$\Rightarrow \tilde{\underline{E}}_x = \left[V^{TM} \frac{k_x}{k_t} - V^{TE} \left(-\frac{k_y}{k_t} \right) \right] e^{-j(k_x x + k_y y)}, \quad (2.113)$$

$$\Rightarrow \tilde{\underline{E}}_x = \left[V_v^{TM} \left(-\tilde{\underline{M}}_{s0}^{dip} \cdot \hat{\underline{v}} \right) \frac{k_x}{k_t} + V_v^{TE} \left(-\tilde{\underline{M}}_{s0}^{dip} \cdot \hat{\underline{u}} \right) \frac{k_y}{k_t} \right] e^{-j(k_x x + k_y y)}, \quad (2.114)$$

$$\Rightarrow \tilde{\underline{E}}_x = \left[V_v^{TM} \left(-\tilde{\underline{M}}_{sy0}^{dip} \hat{\underline{y}} \cdot \hat{\underline{v}} \right) \frac{k_x}{k_t} + V_v^{TE} \left(-\tilde{\underline{M}}_{sy0}^{dip} \hat{\underline{y}} \cdot \hat{\underline{u}} \right) \frac{k_y}{k_t} \right] e^{-j(k_x x + k_y y)}, \quad (2.115)$$

$$\Rightarrow \tilde{\underline{E}}_x = \left[V_v^{TM} \left(-\tilde{\underline{M}}_{sy0}^{dip} \frac{k_x}{k_t} \right) \frac{k_x}{k_t} + V_v^{TE} \left(-\tilde{\underline{M}}_{sy0}^{dip} \frac{k_y}{k_t} \right) \frac{k_y}{k_t} \right] e^{-j(k_x x + k_y y)}, \quad (2.116)$$

$$\Rightarrow \tilde{\underline{E}}_x = -\frac{1}{k_t^2} \left[k_x^2 V_v^{TM} + k_y^2 V_v^{TE} \right] \tilde{\underline{M}}_{sy0}^{dip} e^{-j(k_x x + k_y y)}. \quad (2.117)$$

The x -directed component of the electric field inside the substrate due to the single magnetic dipole source under the $(0, 0)^{\text{th}}$ patch is therefore

$$\underline{E}_x^{inc}(x, y, z) = \frac{1}{(2\pi)^2} \int_{-\infty}^{\infty} \int_{-\infty}^{\infty} \left\{ -\frac{1}{k_t^2} \left[k_x^2 V_v^{TM}(z) + k_y^2 V_v^{TE}(z) \right] \tilde{\underline{M}}_{sy0}^{dip} e^{-j(k_x x + k_y y)} \right\} dk_x dk_y. \quad (2.118)$$

Next we try to find V_v^{TM} and V_v^{TE} at $z = 0$. In Fig. 2.10, the impedances for the TM_z and TE_z fields in the medium that is denoted by i (0 for air or free space, 1 for dielectric) are

$$Z_i^{TM} = \frac{k_{zi}}{\omega \epsilon_i} \quad (2.119)$$

and

$$Z_i^{TE} = \frac{\omega \mu_i}{k_{zi}}. \quad (2.120)$$

Here, $Z_L = 0$ for the microwave case, $Z_L = Z_0$ for the optical case. In these expressions

$$k_{zi}^2 = k_i^2 - k_x^2 - k_y^2, \quad (2.121)$$

where k_{zi} is always chosen to be proper (a decaying wave).

The impedance at the source in Fig. 2.10, looking up is

$$Z^+(-h_d) = Z_1 \left(\frac{Z_0 + jZ_1 \tan(k_{z1} h_d)}{Z_1 + jZ_0 \tan(k_{z1} h_d)} \right). \quad (2.122)$$

The impedance at the source, looking down is

$$Z^-(-h_d) = Z_1 \frac{Z_L + jZ_1 \tan(k_{z1}(h - h_d))}{Z_1 + jZ_L \tan(k_{z1}(h - h_d))}. \quad (2.123)$$

By the voltage divider rule, the total voltage just above the magnetic dipole source ($V_s = 1$ V) at $z = -h_d$ is

$$V_{vs}^+ = V_s \frac{Z^+(-h_d)}{Z^+(-h_d) + Z^-(-h_d)} = \frac{Z^+(-h_d)}{Z^+(-h_d) + Z^-(-h_d)}. \quad (2.124)$$

The reflection coefficient right below the surface of the substrate (looking up through the substrate) is

$$\Gamma = \frac{Z_0 - Z_1}{Z_0 + Z_1}. \quad (2.125)$$

Also,

$$V_{vs}^+ = V_s^+ (1 + \Gamma e^{-j2k_z h_d}), \quad (2.126)$$

where V_s^+ is the forward or upward-going wave at the source in Fig. 2.10.

The total voltage at the surface of the substrate i.e., $z = 0$ is

$$V_v(z=0) = V_s^+ e^{-jk_z h_d} (1 + \Gamma) = \left(\frac{Z^+}{Z^+ + Z^-} \right) \frac{e^{-jk_z h_d} (1 + \Gamma)}{(1 + \Gamma e^{-j2k_z h_d})}. \quad (2.127)$$

The incident field from the single magnetic dipole at the surface of the patches from Eq. (2.118) is

$$E_x^{inc} = \frac{1}{(2\pi)^2} \int_{-\infty}^{\infty} \int_{-\infty}^{\infty} \left\{ -\frac{\tilde{M}_{sy}^{dip}}{k_t^2} \left[k_x^2 V_v^{TM}(0) + k_y^2 V_v^{TE}(0) \right] \right\} e^{-j(k_x x + k_y y)} dk_x dk_y. \quad (2.128)$$

The incident field due to the infinite number of phased dipole sources is then given by

$$\begin{aligned} E_x^{inc,\infty} &= \frac{1}{ab} \sum_{p=-\infty}^{\infty} \sum_{q=-\infty}^{\infty} \left\{ -\frac{1}{k_{tpq}^2} \left[k_{xp}^2 V_v^{TM}(0) + k_{yq}^2 V_v^{TE}(0) \right] \right\} \tilde{M}_{sy}^{dip} e^{-j(k_{xp} x + k_{yq} y)} \\ &= \frac{1}{ab} \sum_{p=-\infty}^{\infty} \sum_{q=-\infty}^{\infty} \tilde{G}_{xy}^{EM} \tilde{M}_{sy}^{dip} e^{-j(k_{xp} x + k_{yq} y)}, \end{aligned} \quad (2.129)$$

so that

$$\tilde{G}_{xy}^{EM}(k_{xp}, k_{yq}) = \left\{ -\frac{1}{k_{tpq}^2} \left[k_{xp}^2 V_v^{TM}(0) + k_{yq}^2 V_v^{TE}(0) \right] \right\}. \quad (2.130)$$

Next, we solve for the basis function coefficients using the method of moments and Galerkin's Method where the testing function is taken to be same as the basis function.

The electric field integral equation (EFIE) is enforced over the patch (0, 0), i.e., $m = 0$, $n = 0$, as

$$E_x^{inc,\infty} + E_x^{sca,\infty} = 0, \quad (2.131)$$

$$\Rightarrow \int_{-W/2}^{W/2} \int_{-L/2}^{L/2} E_x^{sca,\infty} B_{l'}(x, y) dx dy = - \int_{-W/2}^{W/2} \int_{-L/2}^{L/2} E_x^{inc,\infty} B_{l'}(x, y) dx dy, \quad (2.132)$$

$$\begin{aligned} \Rightarrow \frac{1}{ab} \sum_{l=1}^{N_b} a_l \sum_{p=-\infty}^{\infty} \sum_{q=-\infty}^{\infty} \tilde{G}_{xx}^{EJ}(k_{xp}, k_{yq}) \tilde{B}_l(k_{xp}, k_{yq}) \tilde{B}_{l'}(-k_{xp}, -k_{yq}) \\ = -\frac{1}{ab} \sum_{p=-\infty}^{\infty} \sum_{q=-\infty}^{\infty} \tilde{G}_{xy}^{EM}(k_{xp}, k_{yq}) \tilde{M}_{sy}^{dp}(k_{xp}, k_{yq}) \tilde{B}_{l'}(-k_{xp}, -k_{yq}), \end{aligned} \quad (2.133)$$

$$\Rightarrow [Z_{l'l}][a_l] = [R_{l'}], \quad (2.134)$$

where

$$Z_{l'l} = \frac{1}{ab} \sum_{p=-\infty}^{\infty} \sum_{q=-\infty}^{\infty} \tilde{G}_{xx}^{EJ}(k_{xp}, k_{yq}) \tilde{B}_l(k_{xp}, k_{yq}) \tilde{B}_{l'}(-k_{xp}, -k_{yq}) e^{-jk_{xpq} \Delta z} \quad (2.135)$$

$$\text{and } R_{l'} = -\frac{1}{ab} \sum_{p=-\infty}^{\infty} \sum_{q=-\infty}^{\infty} \tilde{G}_{xy}^{EM}(k_{xp}, k_{yq}) \tilde{M}_{sy}^{dp}(k_{xp}, k_{yq}) \tilde{B}_{l'}(-k_{xp}, -k_{yq}). \quad (2.136)$$

Here Δz is the z -displacement between the current on the patches and the testing function.

We solve for the coefficients a_l in Eq. (2.134) for the (0, 0)th patch of the structure with an infinite number of magnetic dipole sources. This is later denoted as $a_l^{00,\infty}$. In the above

expressions the wavenumbers are defined as

$$k_{xp} = k_x + \frac{2\pi p}{a}, \quad k_{yq} = k_y + \frac{2\pi q}{b}. \quad (2.137)$$

We then find the far-field radiation from the structure, excited by a single magnetic dipole source embedded in the dielectric. The far-field radiation is given by

$$E_i^{FF}(r, \theta, \phi) = E_i^{FF,dip}(r, \theta, \phi) + E_i^{FF,patch}(r, \theta, \phi). \quad (2.138)$$

Here, i stands for θ or ϕ corresponding to TM_z and TE_z polarization, respectively,

$E_i^{FF,dip}(r, \theta, \phi)$ represents direct radiation from the magnetic dipole source, and

$E_i^{FF,patch}(r, \theta, \phi)$ represents the radiation from the patch currents.

The far-field radiation from the single magnetic dipole at $(0, 0, -h_d)$ is given by

$$E_i^{FF,dip} = H_y^{pw}(x_0, y_0, -h_d)(1 - \Gamma^{pw}), \quad (2.139)$$

$$\Rightarrow E_i^{FF,dip} = H_y^{pw}(x_0, y_0, 0)(1 - \Gamma^{pw}) \frac{e^{-jk_{z1}h_d} (1 - \Gamma_1 e^{-j2k_{z1}(h-h_d)})}{(1 - \Gamma_1 e^{-j2k_{z1}h})}, \quad (2.140)$$

$$\Rightarrow E_i^{FF,dip} = -\frac{E_x^{pw}(0, 0, 0)}{Z_0} e^{-jk_{x0}^{pw}(-a/2)} (1 - \Gamma^{pw}) \frac{e^{-jk_{z1}h_d} (1 - \Gamma_1 e^{-j2k_{z1}(h-h_d)})}{(1 - \Gamma_1 e^{-j2k_{z1}h})}, \quad (2.141)$$

where

$$\Gamma_1 = \frac{Z_L - Z_1}{Z_L + Z_1}, \quad (2.142)$$

where $Z_L = 0$ for the microwave case, $Z_L = Z_0$ for the optical case. We also have

$$\underline{E}^{pw} = \hat{\underline{p}} \left(-\frac{j\omega\mu}{4\pi r} e^{-jkr} \right) e^{-j\mathbf{k}\cdot\mathbf{r}'} = \hat{\underline{p}} E_0 e^{-j\mathbf{k}\cdot\mathbf{r}'}. \quad (2.143)$$

Here, $\underline{\hat{p}}$ stands for the unit vector $\underline{\hat{\theta}}$ or $\underline{\hat{\phi}}$ corresponding to the TM_z or TE_z polarization, respectively, r is the distance of the testing dipole from the origin, and \underline{r}' is the location of the observation point.

For the microwave case, Eq. (2.141) reduces to

$$E_i^{FF,dip} = -\frac{E_x^{pw}(0,0,0)}{Z_0} e^{-jk_{x0}^{pw}(-a/2)} (1 - \Gamma^{pw}) \frac{\sin(k_{z1}(h-h_d))}{\sin(k_{z1}h)}. \quad (2.144)$$

The coefficients of the basis functions, for the structure with a single magnetic dipole source, are calculated as

$$a_l^{mn} = \frac{ab}{(2\pi)^2} \int_{-\pi/b}^{\pi/b} \int_{-\pi/a}^{\pi/a} a_l^{mn,\infty} dk_x dk_y = \frac{ab}{(2\pi)^2} \int_{-\pi/b}^{\pi/b} \int_{-\pi/a}^{\pi/a} a_l^{00,\infty} e^{-j(k_x ma + k_y nb)} dk_x dk_y. \quad (2.145)$$

The far-field radiation from the array of patches is then given by

$$E_i^{FF,patch} = E_x^{pw}(0,0,0) (1 + \Gamma^{pw}) \sum_{l=1}^{N_b} \tilde{B}_l(k_{x0}^{pw}, k_{y0}^{pw}) \sum_m \sum_n \left(a_l^{mn} e^{j(k_{x0}^{pw} ma + k_{y0}^{pw} nb)} \right), \quad (2.146)$$

where

$$\Gamma^{pw} = \frac{Z_L^{pw} - Z_0}{Z_L^{pw} + Z_0}, \quad Z_L^{pw} = Z_1 \frac{Z_L + jZ_1 \tan(k_{z1}h)}{Z_1 + jZ_L \tan(k_{z1}h)}. \quad (2.147)$$

The wavenumbers k_{x0}^{pw} and k_{y0}^{pw} correspond to the wavenumbers of the radiated plane wave observed at an angle (θ, ϕ) .

2.4 Solving for the Wavenumber of the Leaky Wave on the 2D Periodic LWA Structure

From the ASM formulation, the determinant of the Z Matrix in Eqs. (2.134) and (2.135) is equated to zero for a guided wave, since there is no source, and therefore,

$$\text{Det}([Z_{ll}]) = \text{Det} \left(\left[\frac{1}{ab} \sum_{p=-\infty}^{\infty} \sum_{q=-\infty}^{\infty} \tilde{G}_{xx}^{EJ}(k_{xp}, k_{yq}) \tilde{B}_l(k_{xp}, k_{yq}) \tilde{B}_{l'}(-k_{xp}, -k_{yq}) e^{-jk_{zpq} \Delta z} \right] \right) = 0. \quad (2.148)$$

Here, Δz is the z -displacement between the current on the patches and the testing function, and

$$k_{xp} = k_x + \frac{2\pi p}{a}, \quad k_{yq} = k_y + \frac{2\pi q}{b}, \quad (2.149)$$

and

$$k_x = k_\rho^{LW} \cos \phi_{00}, \quad k_y = k_\rho^{LW} \sin \phi_{00}. \quad (2.150)$$

In the above expressions, k_ρ^{LW} is the wavenumber of the leaky wave along a radial direction, and ϕ_{00} is the angle of propagation that the fundamental Floquet wave makes with the x -axis in Fig. 2.7.

In solving for the wavenumber of the leaky wave, i.e. finding the leaky-wave pole, the value of the wavenumber $k_{zi}^2 = k_i^2 - k_x^2 - k_y^2$ for a given Floquet mode, where $k_x = k_{xp}$ and $k_y = k_{yq}$, is chosen by enforcing the wave to be physical. Therefore, the square root $k_{zi} = \sqrt{k_i^2 - k_x^2 - k_y^2}$ is chosen so that the following conditions are fulfilled [60]. Consider that

$$k_x = \beta_x - j\alpha_x, \quad k_y = \beta_y - j\alpha_y, \quad (2.151)$$

and
$$\underline{k}_t = k_x \hat{x} + k_y \hat{y} = \underline{\beta} - j\underline{\alpha}. \quad (2.152)$$

- a) If $\underline{\beta} \cdot \underline{\alpha} = 0$ (there is no attenuation, $\alpha_x = \alpha_y = 0$) then
- if $|\beta| < k_i$ (fast wave), then $\beta_z > 0$ and
 - if $|\beta| > k_i$ (slow wave), then $\alpha_z > 0$.
- b) If $\underline{\beta} \cdot \underline{\alpha} > 0$ (the wave is a forward wave in the transverse direction) then
- if $|\beta| < k_i$ (fast wave), then $\alpha_z < 0$ (improper) and
 - if $|\beta| > k_i$ (slow wave), then $\alpha_z > 0$.
- c) If $\underline{\beta} \cdot \underline{\alpha} < 0$ (the wave is a backward wave in the transverse direction) then
- if $|\beta| < k_i$ (fast wave), then $\alpha_z > 0$ (proper) and
 - if $|\beta| > k_i$ (slow wave), then $\alpha_z > 0$.

2.5 Enhancement Factor

The enhancement factor is defined here as the E-field magnitude radiated by the leaky-wave antenna at broadside or any other direction specified, divided by the maximum E-field magnitude radiated by the same magnetic dipole source in free space. This is a measure of how much the leaky-wave antenna structure enhances the power density of the radiation in a particular direction. It is also indirectly an indicator of the directivity of the antenna.

2.6 CAD Formula for Calculating the Radiation Pattern of a 1D Leaky-Wave Antenna

Antenna

A bi-directional 1D leaky-wave antenna with equal fields propagating in opposite directions away from a center point (the source of excitation of the LWA), can be modelled approximately as a travelling-wave source [61], which can be seen as a line source of current travelling along the two arms of the leaky-wave antenna, away from the center where it is excited. In the case of the 1D periodic leaky-wave antenna formed by periodic patches on a grounded dielectric substrate, it can be modelled as an electric current source. Let us assume a bi-directional electric line current source along the rotated x -axis, or x' -direction (for a particular $\phi = \phi'$ in the cylindrical coordinate system), radiating in free space as shown in Fig. 2.11 below. This line current source is polarized in the x -direction.

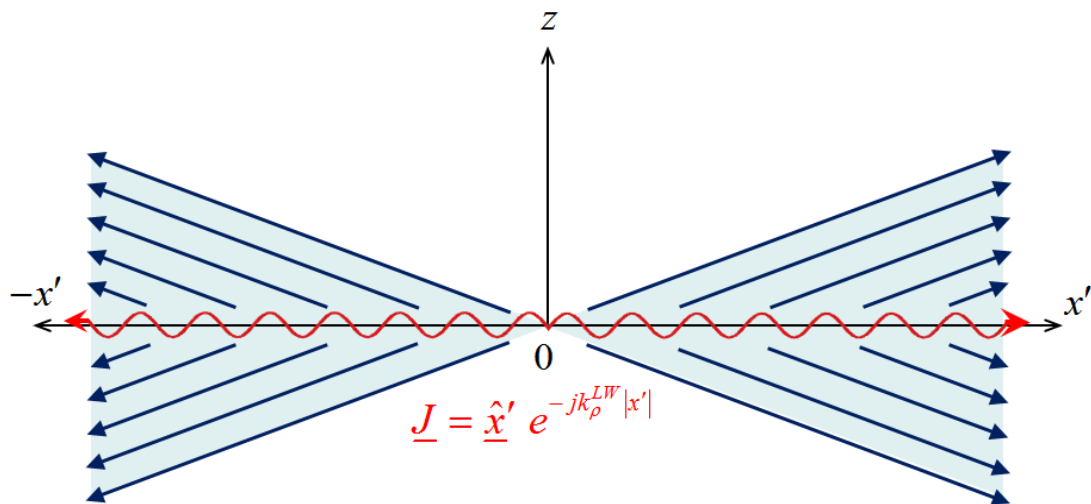


Fig. 2.11. Representation of current on a bi-directional 1D leaky-wave antenna in free space.

The current due to this line source is given by

$$\underline{J}(\rho, \phi, z) = \underline{\hat{x}}' \delta(\phi - \phi') \delta(z) e^{-jk_{\rho}^{LW}(\phi')|x'|}, \quad (2.153)$$

where $k_{\rho}^{LW}(\phi')$ is the wave number of the leaky wave along the ϕ' -direction. This can also be expressed as a bi-directional line current along the x' -direction,

$$I(x') = e^{-jk_{\rho}^{LW}(\phi')|x'|}. \quad (2.154)$$

The array factor due to this line current radiating in free space is given by

$$AF = \int_{-l/2}^{l/2} e^{-jk_{\rho}^{LW}(\phi')|x'|} e^{+jk_0 x' \sin \theta \cos(\phi - \phi')} dx'. \quad (2.155)$$

Here we have ignored the element pattern due to the patches and we have assumed that the length of the 1D leaky-wave antenna (aperture) is l . For an infinitely long leaky-wave antenna, Eq. (2.155) reduces to the closed-form expression

$$AF = \frac{-2jk_{\rho}^{LW}(\phi')}{(k_{\rho}^{LW}(\phi'))^2 - (k_0 \sin \theta \cos(\phi - \phi'))^2}. \quad (2.156)$$

This is the array factor of the 1D leaky-wave antenna and can be used to calculate the approximate radiation pattern of the beam due to the leaky wave.

This current as shown in Fig. 2.11 would produce two conical beams centered around the line source in free space. But when the current exists on the surface of a grounded dielectric substrate, the radiation pattern predicted by the CAD formula of Eq. (2.156) is valid only in the positive half space, i.e., for $z > 0$.

Since the CAD formula in Eq. (2.155) is applicable to 1D leaky-wave antennas, to formulate a CAD formula more applicable to the 2D leaky-wave antennas, a modified formula is proposed as

$$AF = \int_{-l/2}^{l/2} \frac{e^{-jk_{\rho}^{LW}(\phi)|x'|}}{\left(k_{\rho}^{LW}(\phi')(|x'| + c_2 p)\right)^{c_1}} e^{+jk_0 x' \sin \theta \cos(\phi - \phi')} dx'. \quad (2.157)$$

Here p is the period of the patches, a in the E-plane and b in the H-plane. Also, c_1 and c_2 are arbitrary constants whose values are determined by the nature of the leaky wave and could be different in the E-plane and the H-plane. The term in the denominator is included to account for the algebraic spreading due to some form of cylindrical wave propagating along the structure where the energy in the leaky wave spreads radially instead of transmitting along one linear direction as in the case of 1D leaky-wave antenna.

2.7 Grating Lobes

In the Fig. 2.12 below the red circles denote the boundaries for a Floquet mode to become radiative and produce a main beam or grating lobes. The axes are the normalized x component, $u = \beta_x / k_0 = \bar{\beta}_x$ and y component, $v = \beta_y / k_0 = \bar{\beta}_y$ of the wavenumber of propagation in the air region. The green curve denotes the rough values of the normalized phase constant of the leaky wave that is propagating in the radial direction for different angles ϕ . The Floquet modes $(-1, 0)$ and $(0, -1)$ produce the main beams in the E-plane and the H-plane, respectively. The condition for no grating lobes to exist due to any Floquet Mode $(p, q) \neq (-1, 0)$ or $(0, -1)$ is that the red circle corresponding to that mode should not intersect with the green curve. In the first quadrant in Fig. 2.12, the grating lobe could be produced by the $(-1, -1)$ circle intersecting with the green curve. When the main beam is optimized for maximum radiation at broadside, i.e., it is optimum in both the E-plane and H-plane to radiate maximum power density at broadside, the green curve

intersects with the x -axis near $2\pi/(a\lambda_0)$ and with the y -axis is near $2\pi/(b\lambda_0)$. Therefore there is very high chance that the $(-1, -1)$ circle would intersect with the green curve. Therefore it might not be possible to avoid grating lobes in the pattern. In the other quadrants in the above figure, due to symmetry, the other Floquet modes $(-1, 1)$, $(1, 1)$ and $(1, -1)$ would be radiative and produce grating lobes in conjunction with $(-1, -1)$.

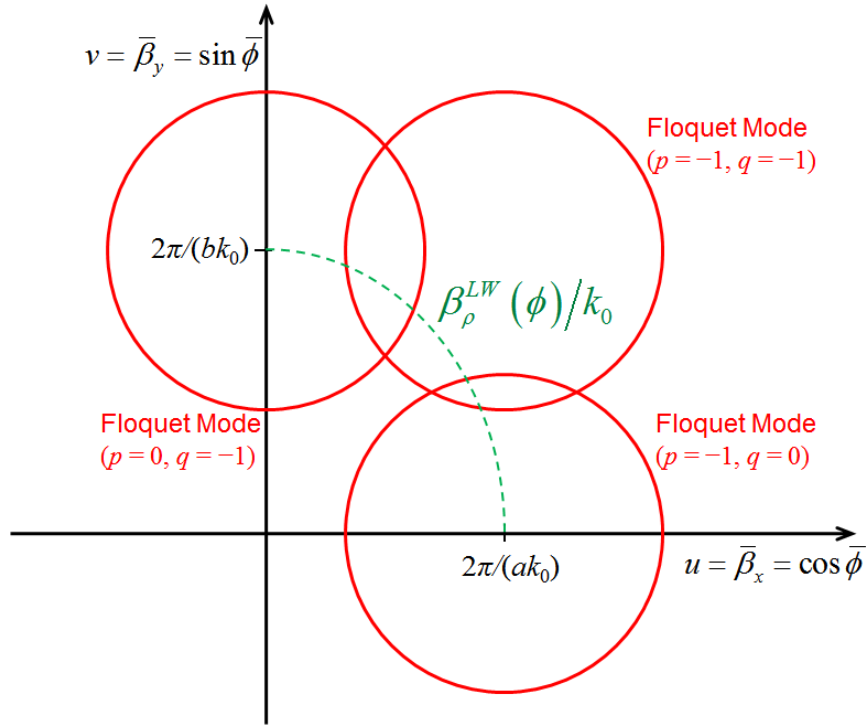


Fig. 2.12. Circle diagram to explain the grating lobes.

The equation for the red circles corresponding to the Floquet mode (p, q) is given by

$$\left(u + \frac{2\pi p}{ak_0}\right)^2 + \left(v + \frac{2\pi q}{bk_0}\right)^2 = 1. \quad (2.158)$$

The region inside the green curve represents the radiative region. When the red circle corresponding to any Floquet mode overlaps with the green curve and partially lies inside

the region enclosed by the green curve, the corresponding Floquet mode radiates. A couple of methods are discussed below to predict the occurrence and direction of the grating lobes in the radiation pattern.

Method A. Predicting the angle θ of the grating lobes in the radiation pattern for a given ϕ plane.

Figure 2.13 below shows a 2D Periodic LWA with a grounded dielectric slab having a periodic lattice of rectangular patches on the upper surface fed by a slot in the ground plane. Here, the vector $\underline{\rho}$ (at an angle ϕ with the x -axis) is in the azimuthal plane of observation in which the radiation pattern is considered, and we assume here that the grating lobes in the radiation pattern are at an angle θ_g with the z -axis.

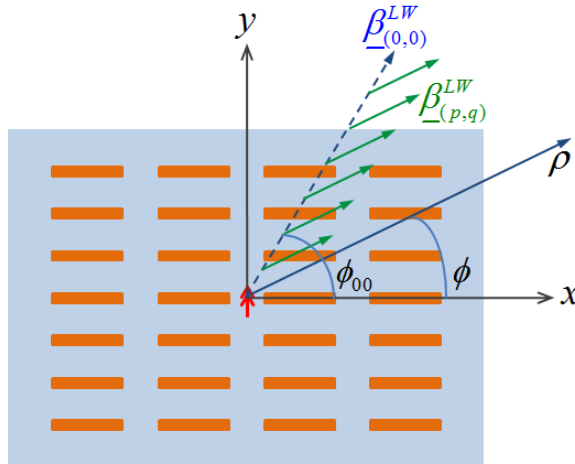


Fig. 2.13. Direction of the radial component of the leaky wave and the plane of observation.

The assumption here is that the grating lobes are caused by the $(p, q)^{\text{th}}$ Floquet harmonic. This means that in the radial direction at an angle ϕ_{00} with the x -axis, the fundamental Floquet mode with wavenumber $k_{(0,0)}^{LW}$ and phase constant $\underline{\beta}_{(0,0)}^{LW}$ is

propagating. Note that $\underline{\beta}_{(0,0)}^{LW}$ is a function of the angle ϕ_{00} along which it propagates. The phase constant vector of the $(p, q)^{\text{th}}$ Floquet harmonic $\underline{\beta}_{(p,q)}^{LW}$ corresponding to this is directed at an angle ϕ with respect to the x -axis, i.e. parallel to $\underline{\rho}$ (same as the plane of observation). Therefore, in order to test that assumption, the following conditions must be true,

$$\underline{\beta}_{(p,q)}^{LW} \times \underline{\hat{\rho}} = 0, \quad (2.159)$$

where

$$\underline{\beta}_{(p,q)}^{LW} = \left(\beta_{(0,0)}^{LW} \cos \phi_{00} + \frac{2\pi p}{a} \right) \underline{\hat{x}} + \left(\beta_{(0,0)}^{LW} \sin \phi_{00} + \frac{2\pi q}{b} \right) \underline{\hat{y}}. \quad (2.160)$$

From Eqs. (2.159) and (2.160) it follows that

$$\left(\frac{\beta_{(0,0)}^{LW} \sin \phi_{00} + 2\pi q/b}{\beta_{(0,0)}^{LW} \cos \phi_{00} + 2\pi p/a} \right) = \tan \phi, \quad (2.161)$$

and since the grating lobe is directed along the angle θ_g in the ϕ plane, we get

$$\left| \underline{\beta}_{(p,q)}^{LW} \right| = k_0 \sin \theta_g. \quad (2.162)$$

Method B. Using a modified CAD formula for an arbitrary ϕ plane.

For any angle ϕ , assume that part of the radiation pattern is formed by the $(p, q)^{\text{th}}$ Floquet harmonic radiated by a narrow strip section of the structure in the ϕ -direction. Also assume that in the radial direction at an angle ϕ_{00} with the x -axis, the fundamental Floquet harmonic with wavenumber $k_{(0,0)}^{LW}$ is propagating for which the corresponding phase constant vector $\underline{\beta}_{(p,q)}^{LW}$ is directed at an angle ϕ with respect to the x -axis, i.e.

parallel to $\underline{\rho}$, and the assumption here is that this mode is mainly responsible for the grating lobe in the radiation pattern in the ϕ plane. Then,

$$\underline{\beta}_{(p,q)}^{LW} \times \underline{\hat{\rho}} = 0, \quad (2.163)$$

where

$$\underline{\beta}_{(p,q)}^{LW} = \left(\beta_{(0,0)}^{LW} \cos \phi_{00} + \frac{2\pi p}{a} \right) \underline{\hat{x}} + \left(\beta_{(0,0)}^{LW} \sin \phi_{00} + \frac{2\pi q}{b} \right) \underline{\hat{y}}. \quad (2.164)$$

From Eqs. (2.163) and (2.164) it follows that

$$\left(\frac{\beta_{(0,0)}^{LW} \sin \phi_{00} + 2\pi q/b}{\beta_{(0,0)}^{LW} \cos \phi_{00} + 2\pi p/a} \right) = \tan \phi. \quad (2.165)$$

For the radiation pattern calculation, the narrow strip section of the structure is treated as a bi-directional line source. The phase constant vector $\underline{\beta}_{(p,q)}^{LW}$ is already parallel to $\underline{\rho}$ and along the line source. Therefore, the wavenumber of the leaky wave along the direction of the line source is

$$k_{\rho}^{LW} = \left| \underline{\beta}_{(p,q)}^{LW} \right| - j\alpha_{(0,0)}^{LW} \cos(\phi_{00} - \phi). \quad (2.166)$$

The normalized radiation pattern in the ϕ plane is then given by the array factor [61],

$$AF = \int_{-l/2}^{l/2} e^{-jk_{\rho}^{LW}|x'|} e^{jk_0 x' \sin \theta} dx'. \quad (2.167)$$

For an infinite aperture i.e. $l \rightarrow \infty$, this reduces to

$$AF = \frac{-2jk_{\rho}^{LW}}{(k_{\rho}^{LW})^2 - (k_0 \sin \theta)^2}. \quad (2.168)$$

The structure analyzed in this work is infinite, so l is always taken to be infinity and Eq. (2.168) is used for the calculations.

CHAPTER 3 RADIATION CHARACTERISTICS OF THE 2D PERIODIC MICROWAVE ANTENNA

This chapter investigates the radiation characteristics of the structure described in Section 1.4 of Chapter 1 and shown in Fig. 1.1 at microwave frequencies. It is a 2D periodic leaky-wave antenna (LWA) that consists of a grounded dielectric slab with periodic arrangement of narrow metal patches on top and a slot in the ground plane for excitation of the 2D leaky wave. All the results presented in this chapter have been computed with one basis function in Eq. (2.18) for the surface current distribution on the surface of the patches.

3.1 Optimization of the 2D Periodic Leaky-Wave Antenna

The 2D periodic leaky-wave antenna produces a three-dimensional conical beam that can be optimized to converge into a narrow directive beam at broadside, as shown in Fig. 3.1. The beam is optimized by adjusting the spatial period in the x -direction a to get the maximum power density at broadside, keeping all other parameters fixed for a given length L and width W of the patches, including the substrate properties. The spatial period in the y -direction b is either kept fixed or is taken to be a constant fraction of a (such as $b = a/1.2$). Figure 3.2 shows the contour plot of the power radiated (in dB) in the far field at broadside for a range of values of a and b . For this case the frequency is $f = 12$ GHz, the height of substrate is $h = 1.27$ mm, the relative permittivity of the substrate is $\epsilon_r = 9.8$, and the substrate is taken to be lossless. The length of the patch is $L = 0.25$ cm and width

is $W = L/5$. The power radiated is calculated using reciprocity as described in Section 2.2 of Chapter 2.

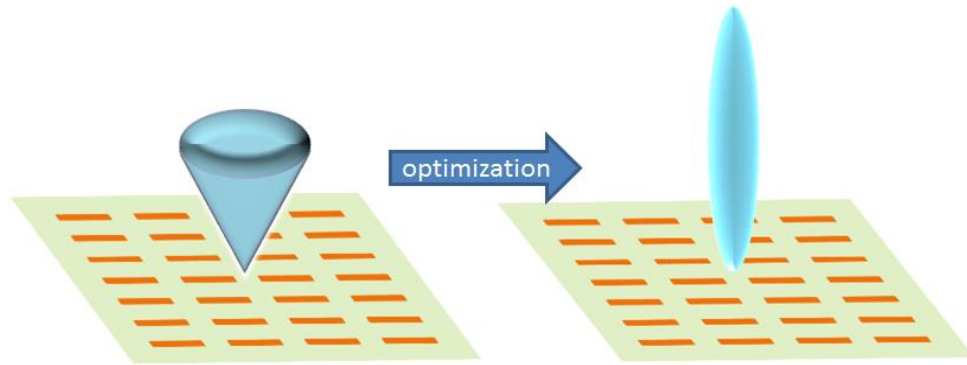


Fig. 3.1. Optimization of the beam at broadside.

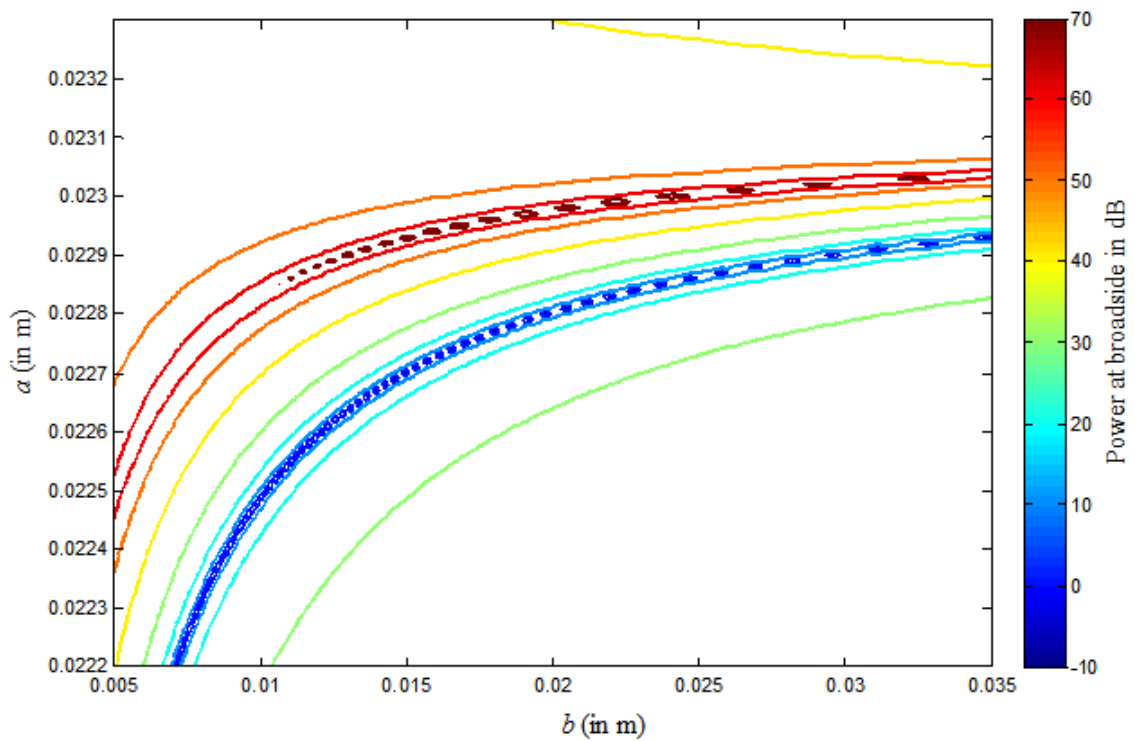


Fig. 3.2. Contour plot of the power radiated at broadside for different values of a and b .

In Fig. 3.2, the band of red is the region of highest power radiated and the plot shows that this region is like a ridge that runs across the whole range of values for b ; there is no

clear maxima seen on this color scale. Figure 3.3 gives the maximum E field at broadside plotted with respect to b , for which the power at broadside is maximized by adjusting a for the given b . For the field calculation, the magnetic dipole source is taken to be unit amplitude.

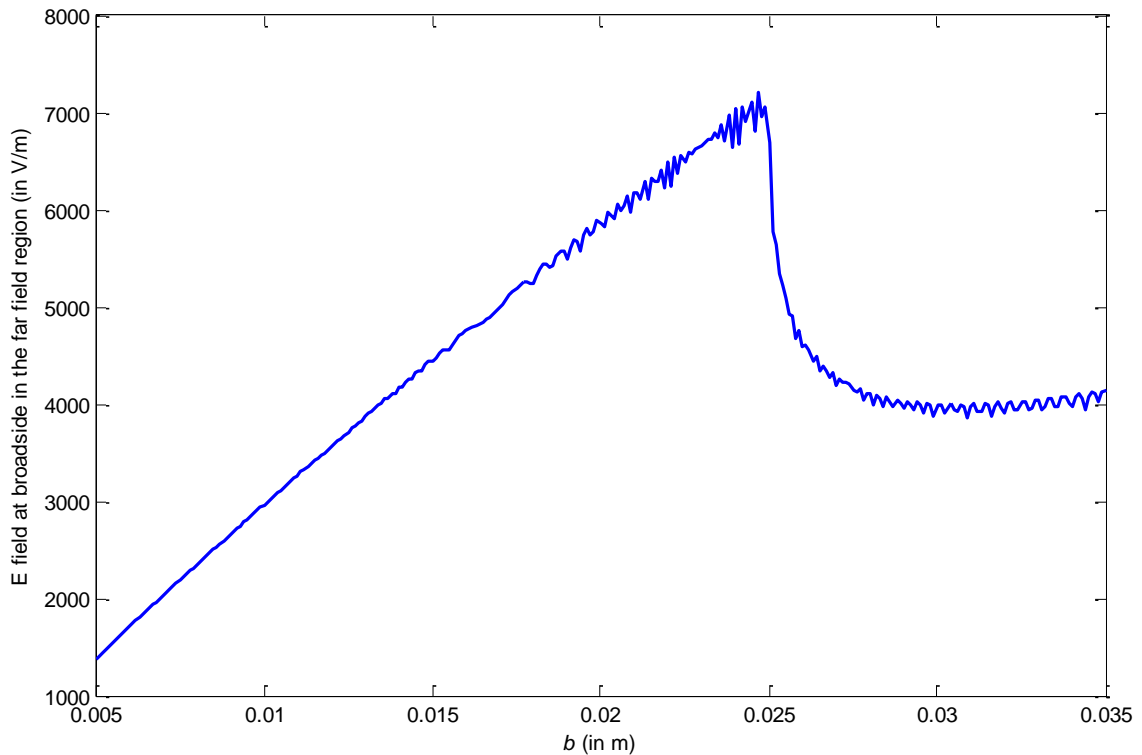


Fig. 3.3. Plot of optimized maximum electric field at broadside vs b .

Figure 3.2 shows that there is a value of b for which, when the value of a is optimized, gives the maximum power radiation at broadside; but this might not be considered a good design as there will be a lot of grating lobes in the radiation pattern. It has been observed that choosing a lower value of b reduces the grating lobes in the radiation pattern. So there is a trade-off in the design between power density radiated at broadside and grating lobes.

3.2 Radiation Patterns

For the microwave design, throughout the study, the frequency is taken to be $f = 12$ GHz. The substrate here is chosen to have a relative permittivity of $\epsilon_r = 9.8$, a loss tangent of $\tan\delta = 0.002$, and the height of substrate is $h = 1.27$ mm. The substrate is a grounded dielectric with the excitation provided by a narrow y -directed slot in the ground plane. The slot is centered at the location $(x_0 = a/2, y_0 = 0)$. The slot in the ground plane is modeled as an infinitesimal magnetic dipole. Radiation patterns for some typical cases with small patch sizes will be shown.

In the case in Fig. 3.4 the length of the patches is $L = 0.250$ cm, the width is $W = L/5$, and the dimensions of the unit cell are given by $a = 2.29705$ cm and $b = a/1.2$. Here the substrate is taken to be lossless. In this case the enhancement factor is 283.70. In the case presented in Fig. 3.5 the length of the patch is slightly larger, $L = 0.300$ cm, the width is $W = L/5$, and the dimensions of the unit cell are given by $a = 2.27271$ cm and $b = a/1.2$. The substrate is again taken to be lossless. In this case the enhancement factor is 110.89. In the case shown in Fig. 3.6 the length of the patch is $L = 0.250$ cm, the width is $W = L/5$, and the dimensions of the unit cell are given by $a = 2.29708$ cm and $b = a/1.2$. Here the substrate is taken to be lossy with a loss tangent $\tan\delta = 0.002$. In this case the enhancement factor is 78.68. In the case presented in Fig. 3.7 the length of the patch is $L = 0.300$ cm, the width is $W = L/5$, and the dimensions of the unit cell are given by $a = 2.27280$ cm and $b = a/1.2$. Here the substrate is taken to be lossy with loss tangent $\tan\delta = 0.002$. In this case the enhancement factor is 70.02.

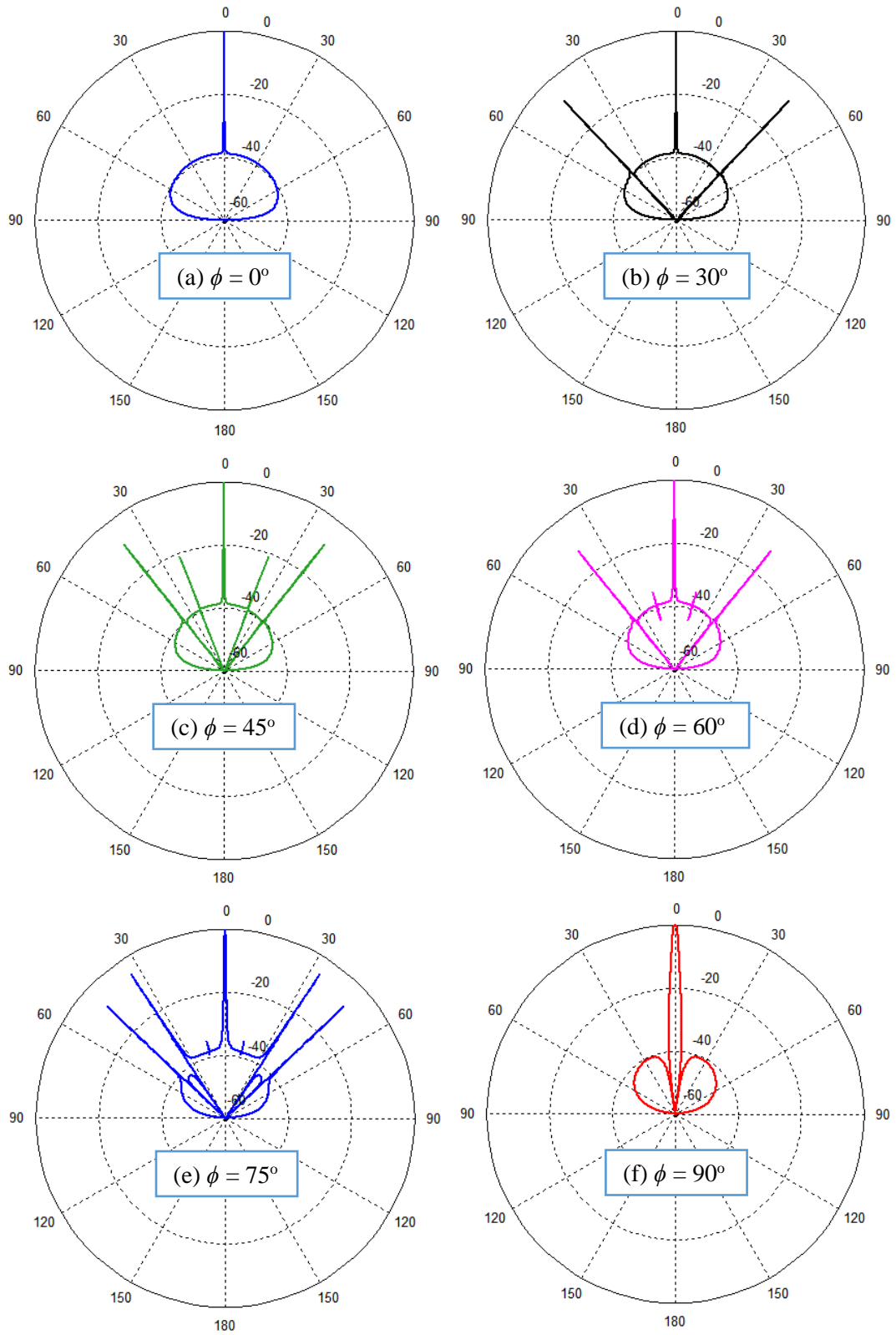


Fig. 3.4. (a)-(f) Radiation patterns in different ϕ planes for a lossless substrate with $L = 0.25$ cm.

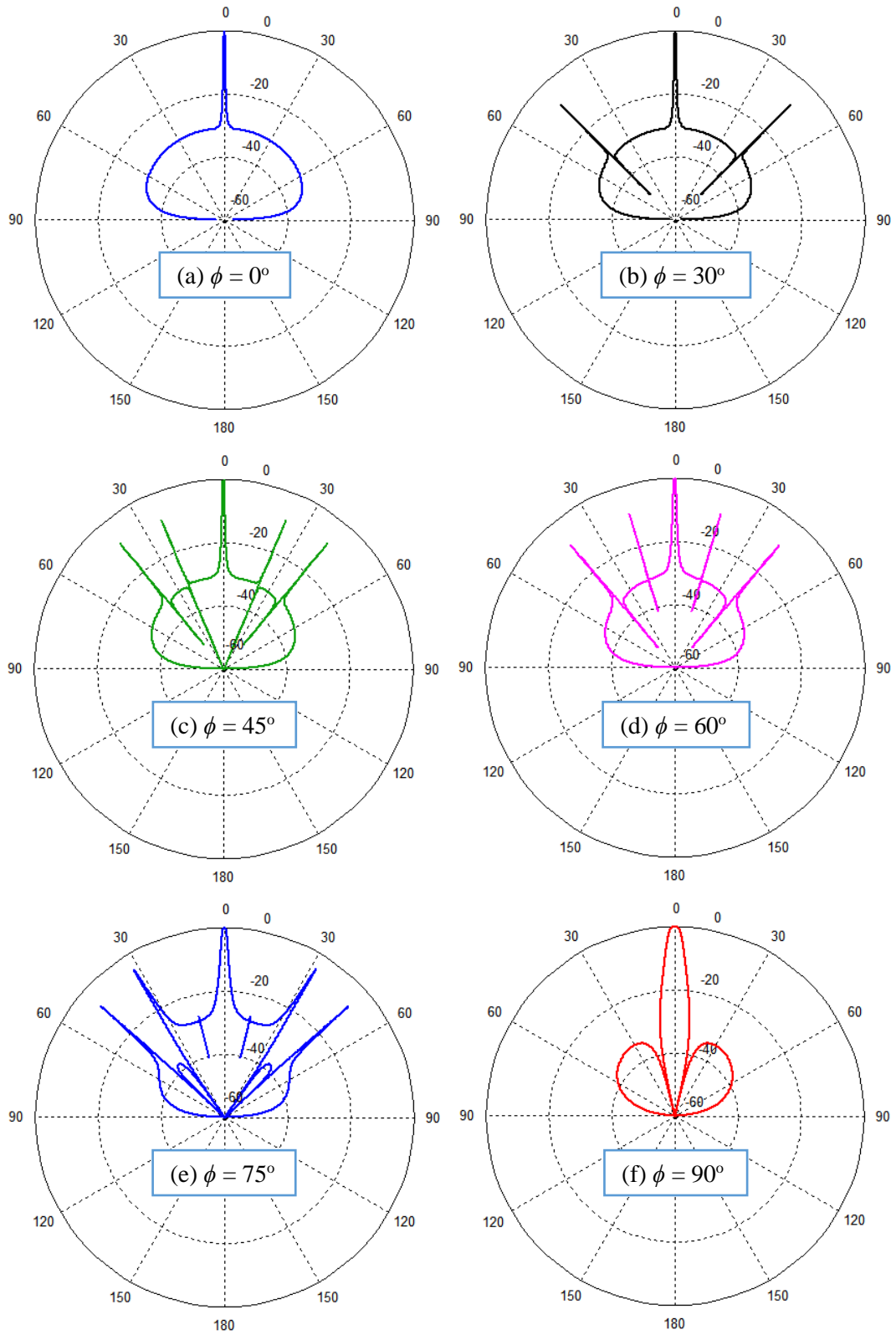


Fig. 3.5. (a)-(f) Radiation patterns in different ϕ planes for a lossless substrate with $L = 0.30$ cm.

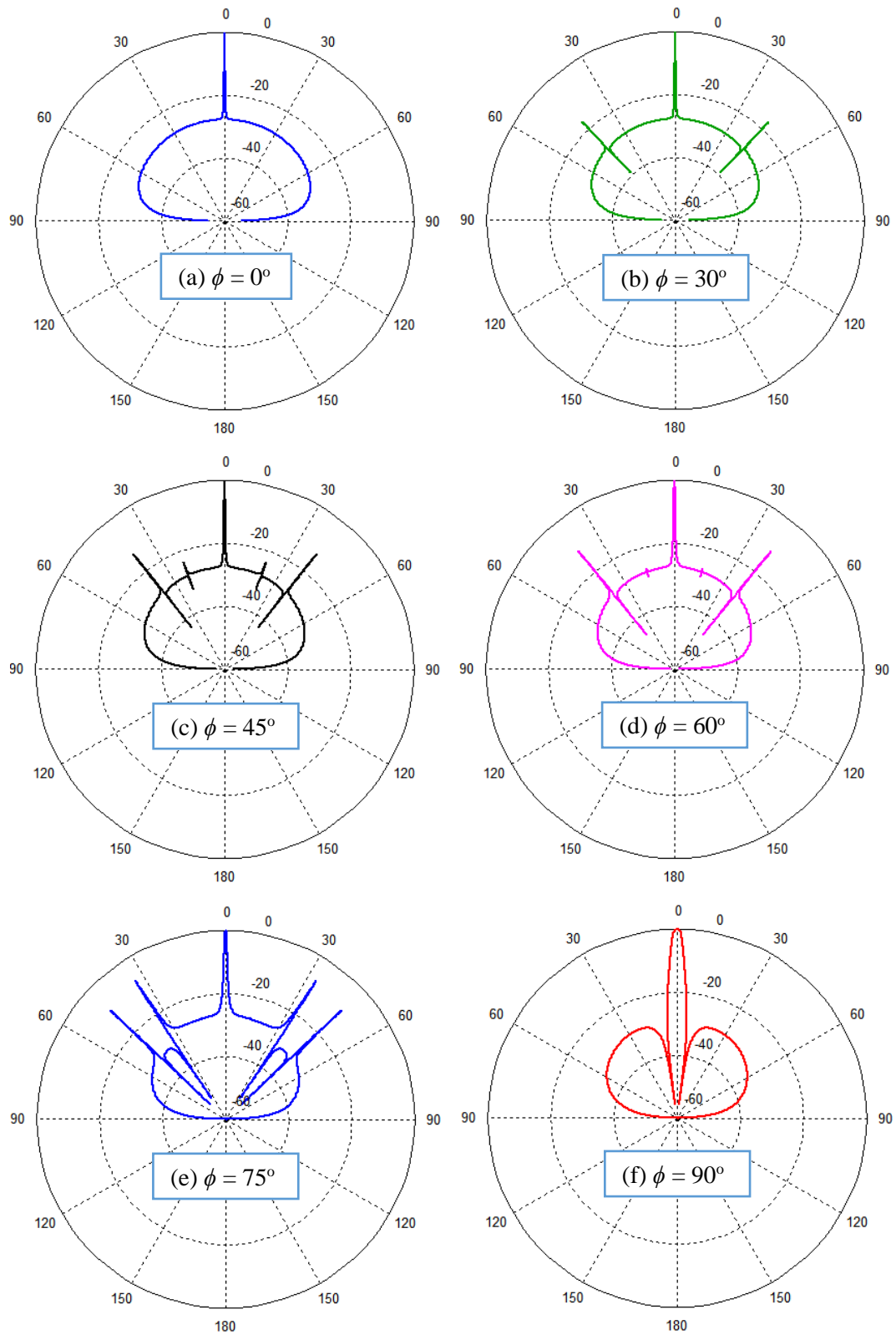


Fig. 3.6. (a)-(f) Radiation patterns in different ϕ planes for a lossy substrate with $L = 0.25$ cm.

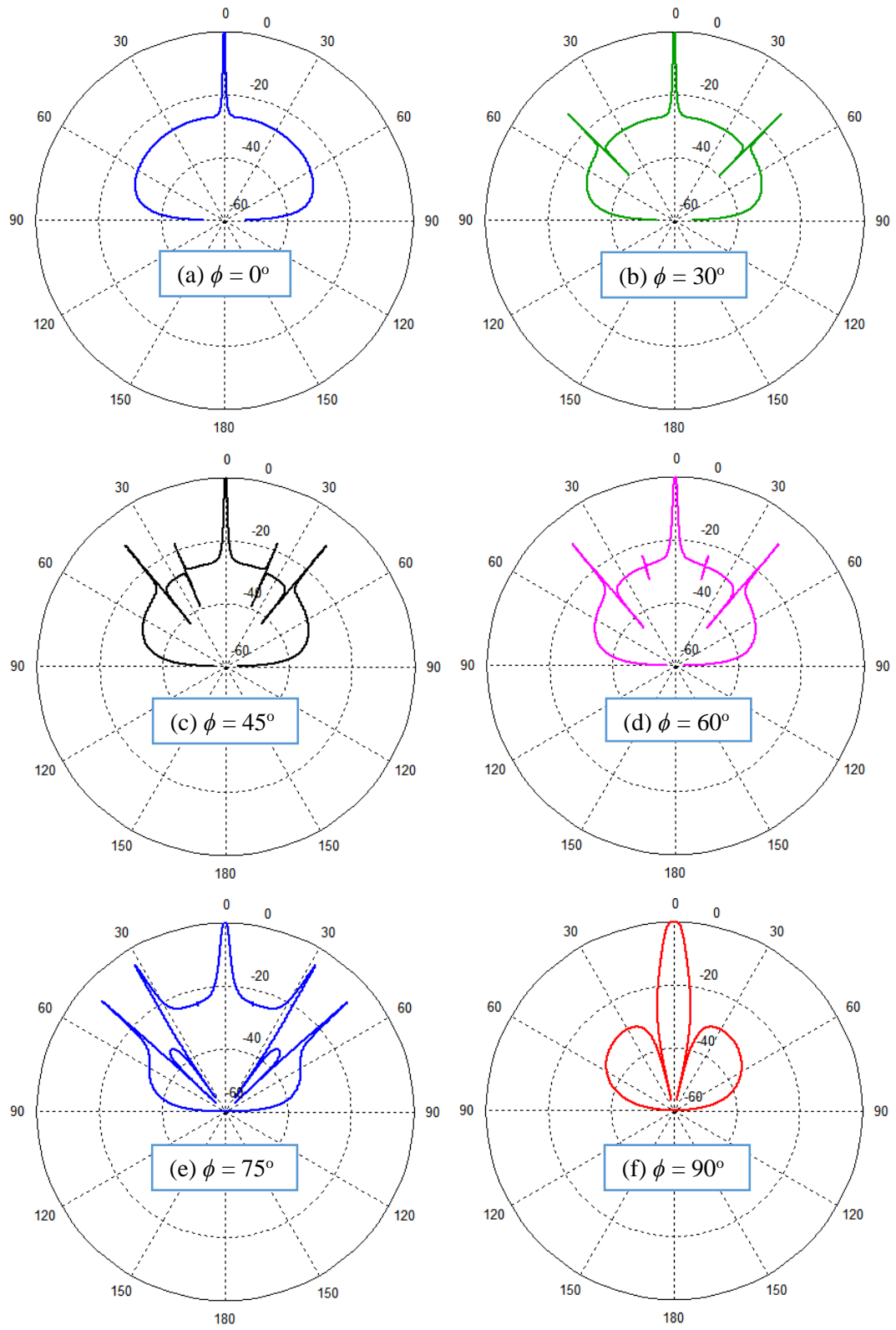


Fig. 3.7. (a)-(f) Radiation patterns in different ϕ planes for a lossy substrate with $L = 0.30$ cm.

3.3 Variation of the Main Beam with Frequency

At first the design is optimized for the frequency $f = 12$ GHz so that the power density at broadside is maximum. Once again, the substrate is chosen to have a relative permittivity of $\epsilon_r = 9.8$ and a loss tangent of $\tan\delta = 0.002$. The substrate is a grounded dielectric and the height is $h = 1.27$ mm, with the excitation provided by a narrow y -directed slot in the ground plane. The slot is centered at the location $(x_0 = a/2, y_0 = 0)$. Here the length of the patch is $L = 0.300$ cm, the width is $W = L/5$, and the dimensions of the unit cell are given by $a = 2.27280$ cm and $b = a/1.2$. Then the frequency is varied to 0.5 GHz above and below the optimum to see the effects on the radiation pattern in the E-plane and H-plane, shown in Fig. 3.8 and Fig. 3.9 respectively.

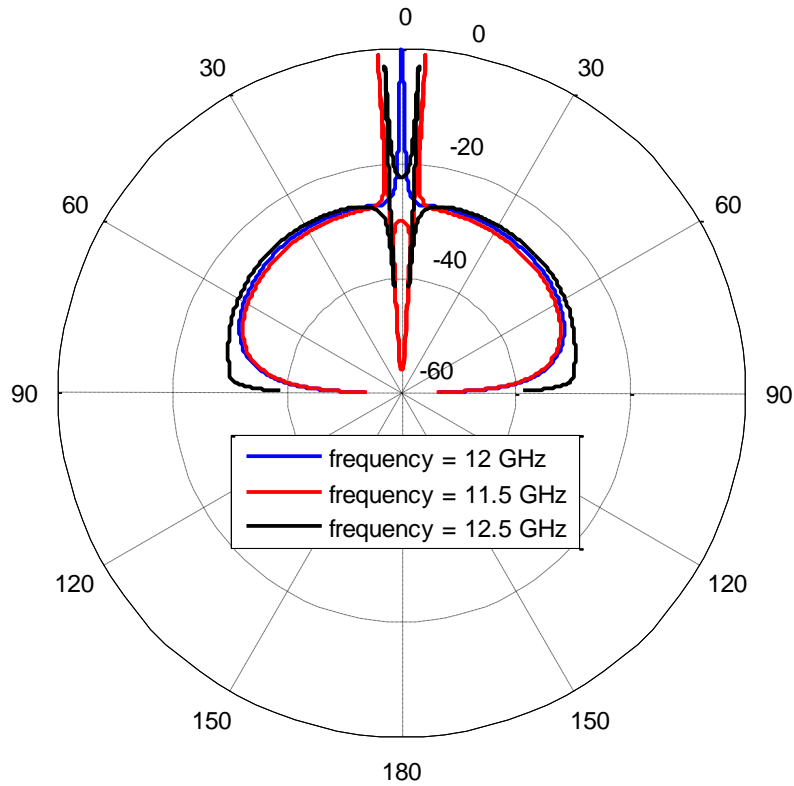


Fig. 3.8. Splitting of the beam in the E-plane, when the frequency is changed from the optimum frequency of 12 GHz.

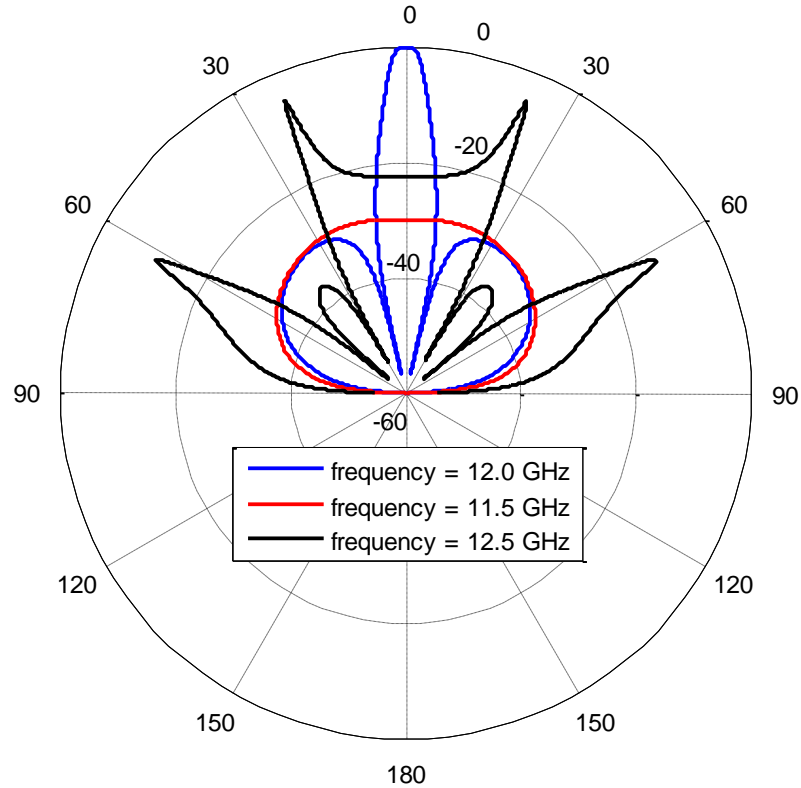


Fig. 3.9. Variation of the beam in the H-plane, when the frequency is changed from the optimum frequency of 12 GHz.

From Fig. 3.8 we see that for both increased and decreased frequency from the optimum frequency, the main beam splits in the E-plane. In the H-plane, as seen in Fig. 3.9, when the frequency is varied from the optimum the beam splits to a great extent for the higher frequency but completely disappears for the lower frequency.

3.4 CAD Formula for the Leaky-Wave Radiation Pattern

For the calculation of the pattern due to a leaky wave propagating in a radial direction, the CAD formula for a 1D leaky-wave antenna given in Eq. (2.156) works very well. Any attempts to improve this by trying different combinations of c_1 and c_2 in Eq. (2.157) in the E-plane and H-plane were unsuccessful. So the speculation is that though

the power spreads out radially for the 2D leaky wave, and the power in the radial direction diminishes, the width of the angular sector region contributing to the beam increases as the distance from the source increases. Therefore, henceforth, the CAD formula used to calculate the pattern due to the radial leaky wave in any direction for the 2D periodic leaky-wave antenna is the same as that for the 1D leaky-wave antenna given in Eq. (2.156).

A comparison of the radiation patterns from reciprocity and the CAD formula in the E-plane is shown in Fig. 3.10 and for the H-plane in Fig. 3.11. In the following case the length of the patches is $L = 0.300$ cm, the width is $W = L/5$, and the dimensions of the unit cell are given by $a = 2.27271$ cm and $b = a/1.2$. Here the substrate is taken to be lossless with a loss tangent $\tan\delta = 0$. The wavenumber of the radiating $(-1, 0)$ harmonic of the leaky-wave mode along the x -axis is $k_{\rho}^{LW} = (-6.0401 \times 10^{-4} - j5.7653 \times 10^{-4})k_0$, and the wavenumber of the radiating $(0, -1)$ harmonic of the leaky-wave mode along the y -axis is $k_{\rho}^{LW} = (0.01001408 - 0.010489)k_0$ where k_0 is the wavenumber of plane wave in free space at this frequency. The total radiation pattern of the 2D periodic LWA has two components. One is due to the radiation from the leaky wave supported by the structure, and this produces the main beam at broadside. This component is approximately described by the CAD formula. The rest of the radiation pattern is due to the space wave, which is direct radiation from the source dipole. There appears to be good agreement between the main beam from reciprocity and the leaky-wave beam given by the CAD formula as seen in Fig. 3.10 and Fig. 3.11, since the level of the space wave is fairly small (less than -30 dB relative to the peak of the main beam).

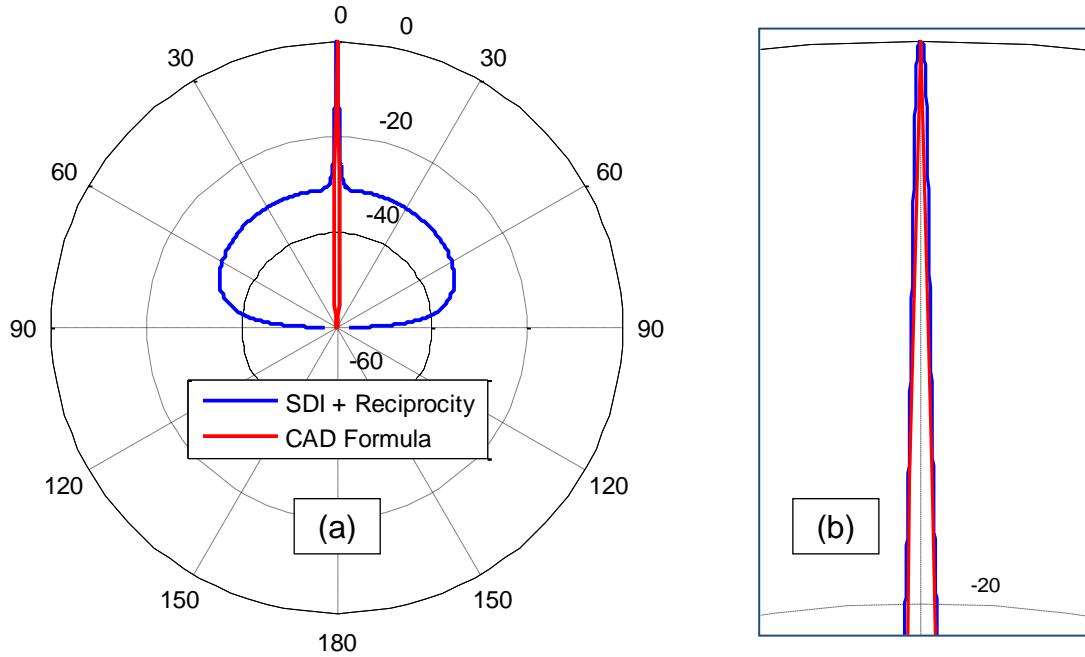


Fig. 3.10. (a) Pattern of the leaky-wave beam compared to the pattern from reciprocity in the E-plane. (b) An expanded view of the main beam around the -20 dB power level.

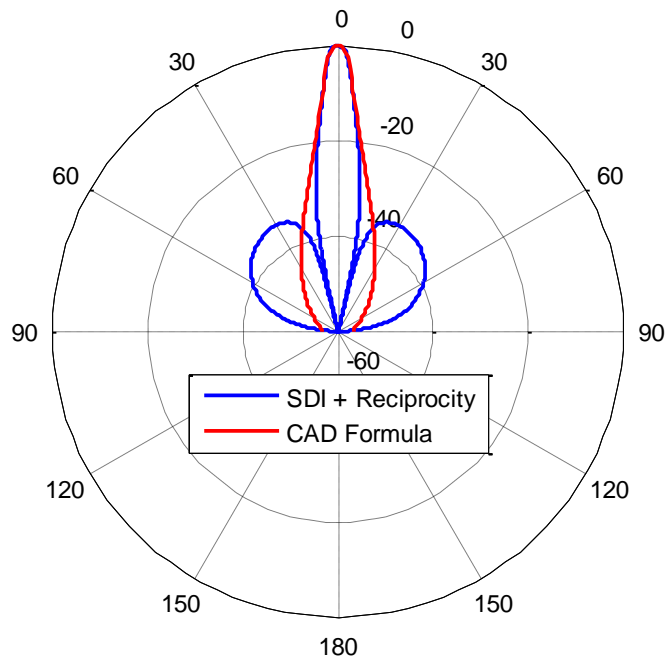


Fig. 3.11. Pattern of the leaky-wave beam compared to the pattern from reciprocity in the H-plane.

3.5 Designs for 2D Periodic Leaky-Wave Antenna with Different Practical Substrates

In the case shown in Fig. 3.12, the frequency is 24 GHz, the grounded dielectric slab has a relative permittivity of $\epsilon_r = 10.2$, a loss tangent of $\tan\delta = 0.0023$, and the height of substrate is $h = 0.635$ mm. The excitation, as before, is provided by a narrow y -directed slot in the ground plane. The slot is centered at the location $(x_0 = a/2, y_0 = 0)$. The slot in the ground plane is modeled as an infinitesimal magnetic dipole. The length of the patches is $L = 0.250$ cm, the width is $W = L/5$, the dimensions of the unit cell are given by $a = 1.17748$ cm and $b = a/1.2$. For these cases we take $\Delta z = 0$ in the method of moments calculation. For the next case with radiation patterns given in Fig. 3.13, the parameters are the same as before except that the length of the patches is $L = 0.300$ cm, the width is $W = L/5$, and the dimensions of the unit cell are given by $a = 1.17258$ cm and $b = a/1.2$.

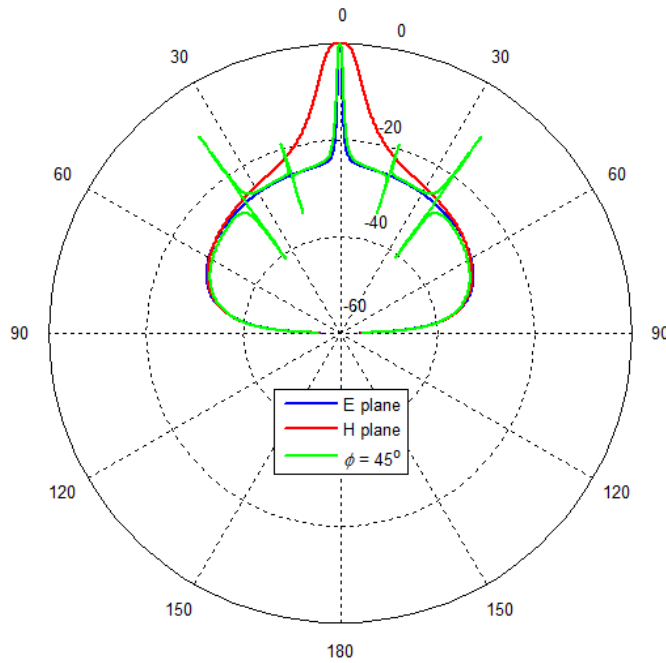


Fig. 3.12. Radiation patterns in E-plane, H-plane, and D-plane ($\phi = 45^\circ$).

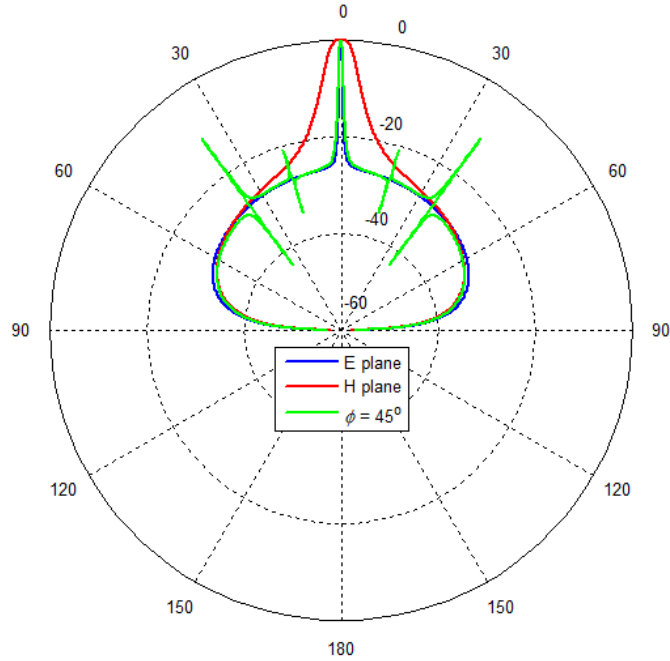


Fig. 3.13. Radiation patterns in E-plane, H-plane, and D-plane ($\phi = 45^\circ$).

For the case with radiation patterns given in Fig. 3.14, the parameters are the same as before except that the length of the patches is $L = 0.180$ cm, the width is $W = L/5$, and the dimensions of the unit cell are given by $a = 1.10804$ cm and $b = a/1.2$. For the next case with radiation patterns given in Fig. 3.15, the parameters are the same as before except that the length of the patch is $L = 0.190$ cm, the width is $W = L/5$, and the dimensions of the unit cell are given by $a = 1.03408$ cm and $b = a/1.2$.

For the case with radiation patterns given in Fig. 3.16, the parameters are the same as before except that the length of the patches is $L = 0.200$ cm, the width is $W = L/5$, and the dimensions of the unit cell are given by $a = 1.24716$ cm and $b = a/1.2$. For the following case with radiation patterns given in Fig. 3.17, the parameters are the same as before except that the length of the patch is $L = 0.210$ cm, the width is $W = L/5$, and the dimensions of the unit cell are given by $a = 1.20828$ cm and $b = a/1.2$.

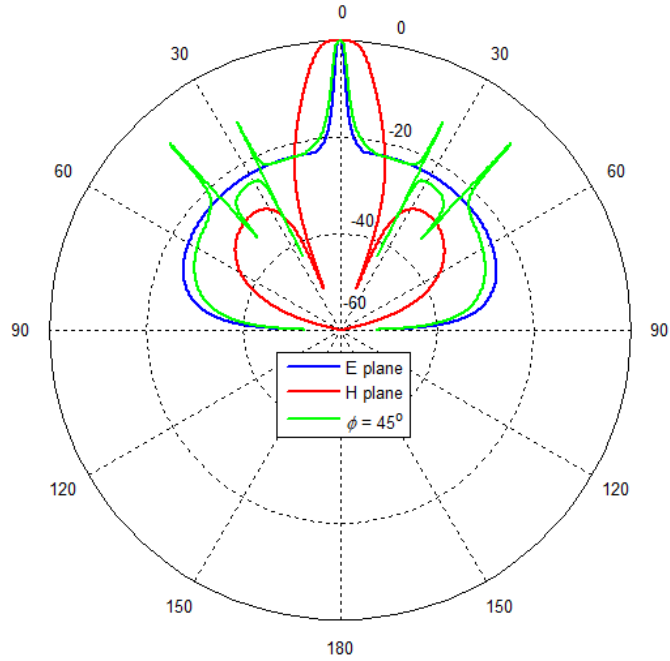


Fig. 3.14. Radiation patterns in E-plane, H-plane, and D-plane ($\phi = 45^\circ$).

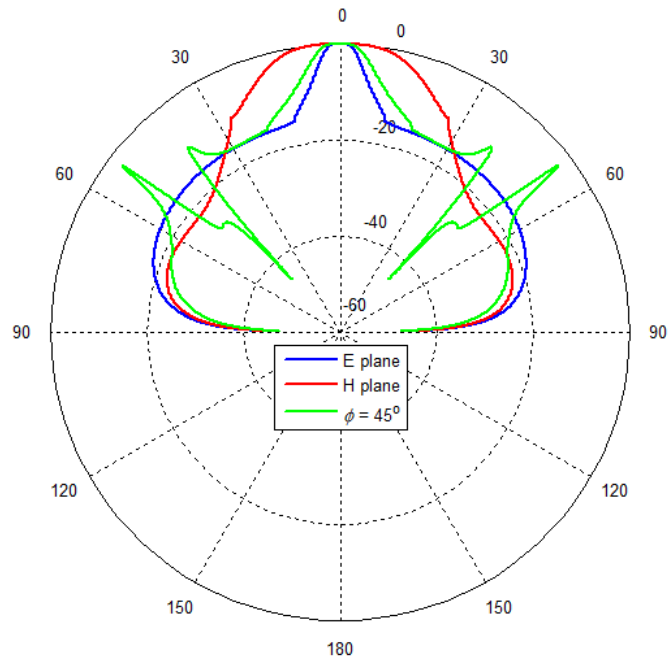


Fig. 3.15. Radiation Patterns in E-plane, H-plane, and D-plane ($\phi = 45^\circ$).

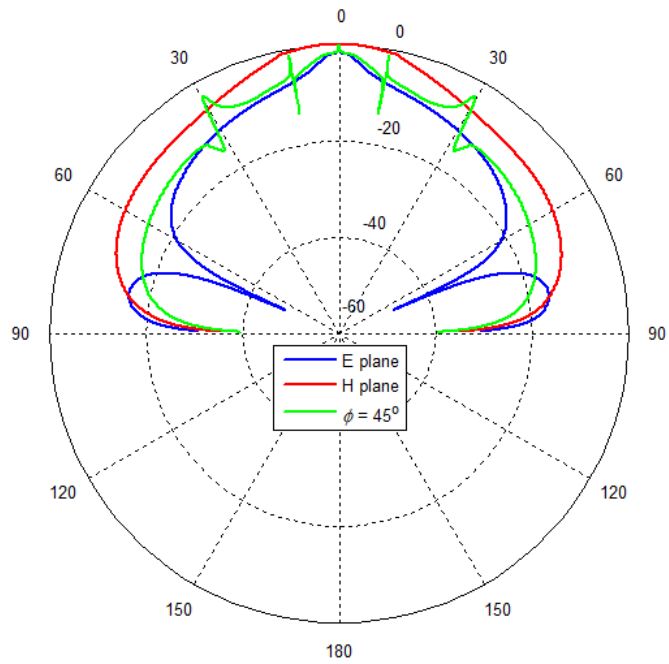


Fig. 3.16. Radiation patterns in E-plane, H-plane, and D-plane ($\phi = 45^\circ$).

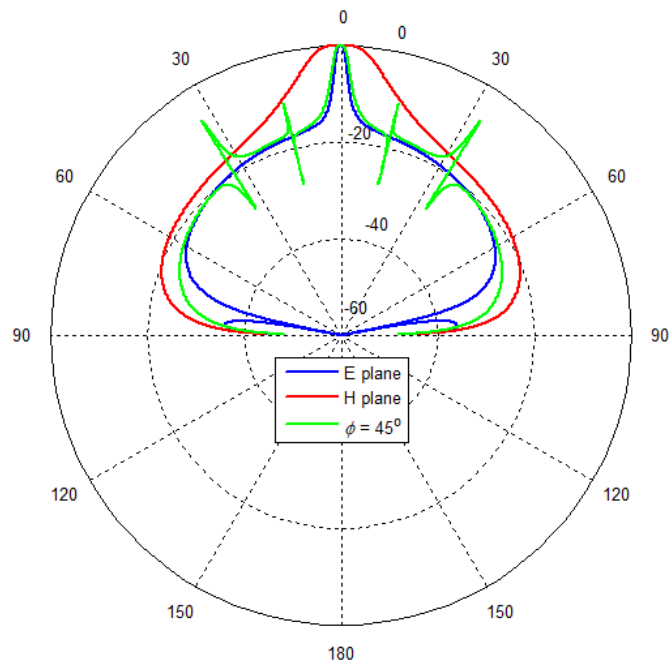


Fig. 3.17. Radiation patterns in E-plane, H-plane, and D-plane ($\phi = 45^\circ$).

In the case shown in Fig. 3.18, the frequency is 24 GHz, the grounded dielectric slab has a relative permittivity of $\epsilon_r = 2.2$, a loss tangent of $\tan\delta = 0.0009$, and the height of substrate is $h = 1.575$ mm. The excitation, as before, is provided by a narrow y -directed slot in the ground plane. The slot is centered at the location $(x_0 = a/2, y_0 = 0)$. The slot in the ground plane is modeled as an infinitesimal magnetic dipole. The length of the patch is $L = 0.250$ cm, the width is $W = L/5$, and the dimensions of the unit cell are given by $a = 1.12997$ cm and $b = a/1.2$. For the next case with radiation patterns given in Fig. 3.19, the parameters are the same as before except that the length of the patch is $L = 0.300$ cm, the width is $W = L/5$, and the dimensions of the unit cell are given by $a = 1.12162$ cm and $b = a/1.2$.

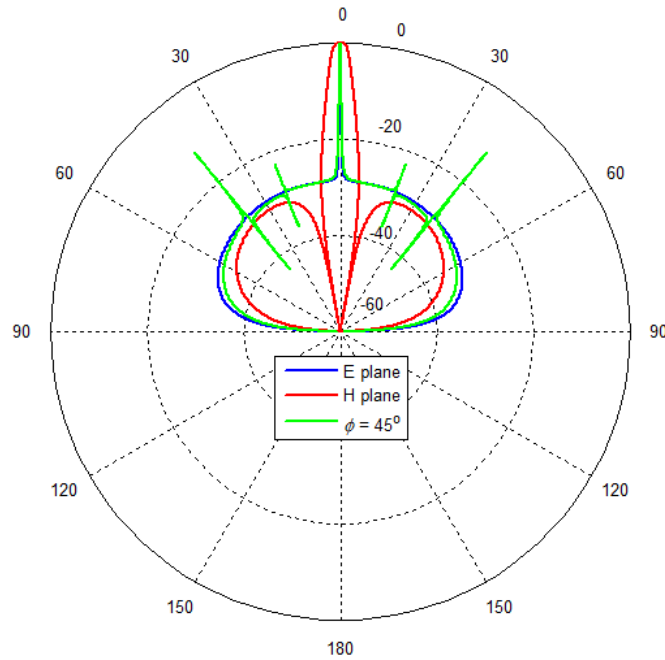


Fig. 3.18. Radiation patterns in E-plane, H-plane, and D-plane ($\phi = 45^\circ$).

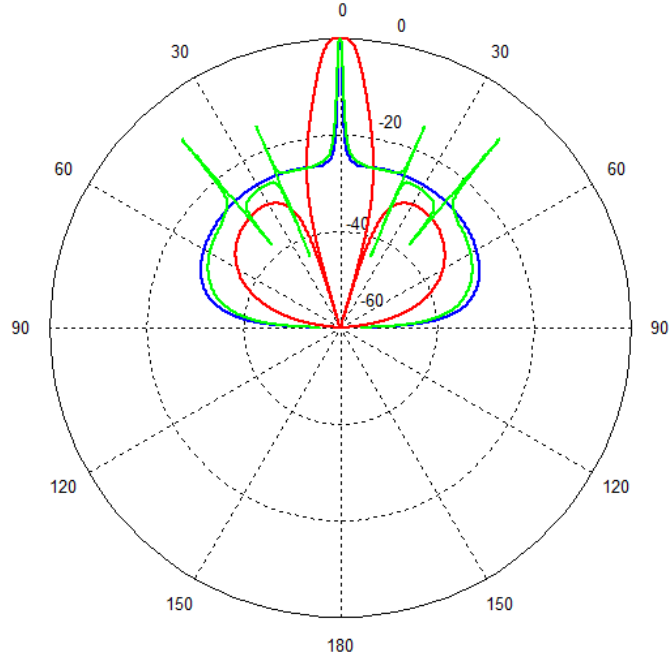


Fig. 3.19. Radiation patterns in E-plane, H-plane, and D-plane ($\phi = 45^\circ$).

In the following case as shown in Fig. 3.20, the frequency is 24 GHz, grounded dielectric slab with relative permittivity of $\epsilon_r = 9.2$, loss tangent of $\tan\delta = 0.0022$ and the height of substrate is $h = 0.635$ mm. The excitation, as before is provided by a narrow y -directed slot in the ground plane. The slot is centered at the location $(x_0 = a/2, y_0 = 0)$. The slot in the ground plane is modeled as an infinitesimal magnetic dipole. The length of the patch is $L = 0.250$ cm, the width is $W = L/5$, the dimensions of the unit cell are given by $a = 1.18979$ cm and $b = a/1.2$. For the next case with radiation patterns given in Fig. 3.21, the parameters are the same as before except that the length of the patches is $L = 0.300$ cm, the width is $W = L/5$, and the dimensions of the unit cell are given by $a = 1.18230$ cm and $b = a/1.2$.

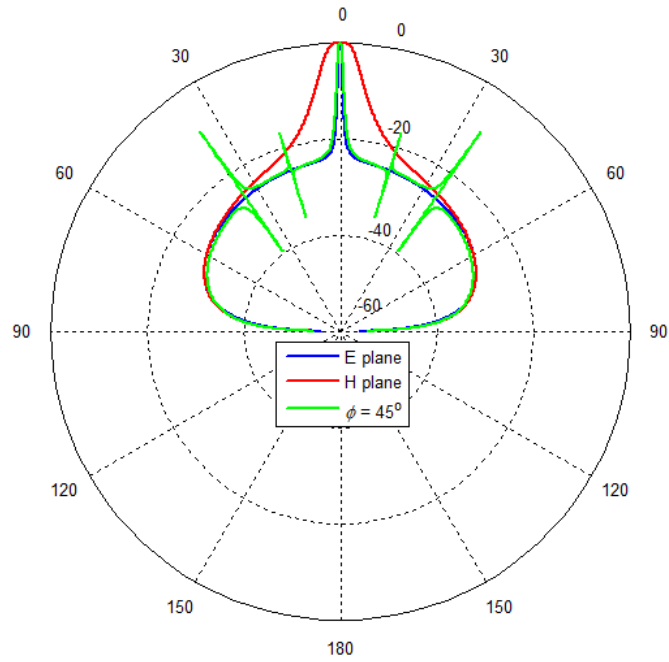


Fig. 3.20. Radiation patterns in E-plane, H-plane, and D-plane ($\phi = 45^\circ$).

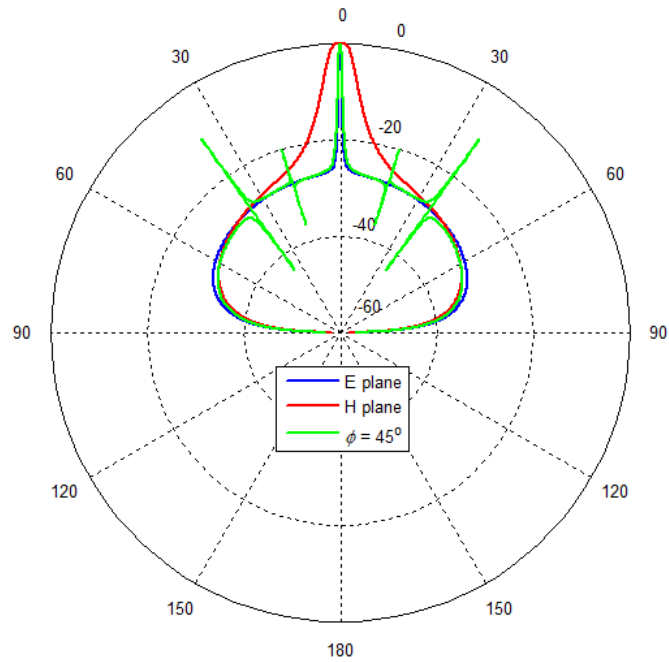


Fig. 3.21. Radiation patterns in E-plane, H-plane, and D-plane ($\phi = 45^\circ$).

In the following case shown in Fig. 3.22, the frequency is 24 GHz, the grounded dielectric slab has a relative permittivity of $\epsilon_r = 3.66$, a loss tangent of $\tan\delta = 0.004$, and the height of substrate is $h = 0.813$ mm. The excitation, as before, is provided by a narrow y -directed slot in the ground plane. The slot is centered at the location $(x_0 = a/2, y_0 = 0)$. The slot in the ground plane is modeled as an infinitesimal magnetic dipole. The length of the patch is $L = 0.250$ cm, the width is $W = L/5$, and the dimensions of the unit cell are given by $a = 1.17633$ cm and $b = a/1.2$. For the next case with radiation patterns given in Fig. 3.23, the parameters are again the same as before except that the length of the patch is $L = 0.300$ cm, the width is $W = L/5$, and the dimensions of the unit cell are given by $a = 1.14608$ cm and $b = a/1.2$.

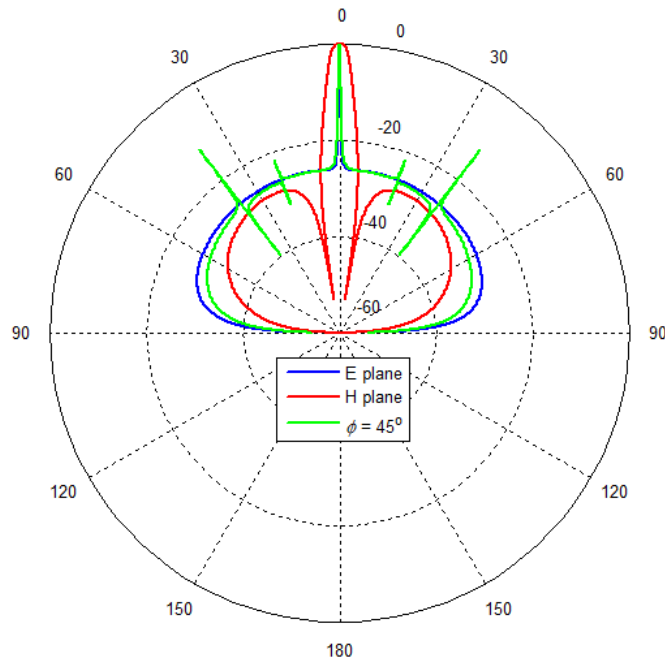


Fig. 3.22. Radiation patterns in E-plane, H-plane, and D-plane ($\phi = 45^\circ$).

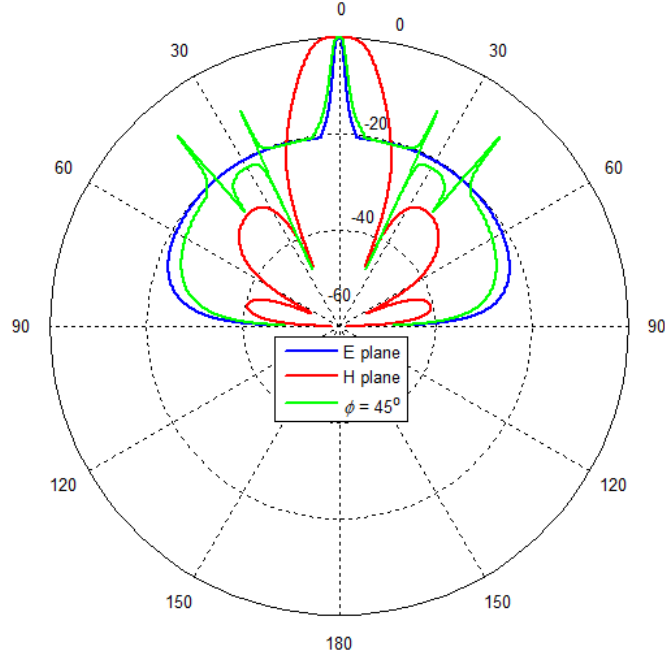


Fig. 3.23. Radiation patterns in E-plane, H-plane, and D-plane ($\phi = 45^\circ$).

3.6 Cross-Section of the Main Beam for Different Power Levels

In this section we take a close look at the cross-section of the beam at power levels of -3 dB in Fig. 3.24, -6 dB in Fig. 3.25, -9 dB in Fig. 3.26, and -12 dB in Fig. 3.27. The frequency here is taken to be $f = 12$ GHz. The substrate is chosen to have a relative permittivity of $\epsilon_r = 9.8$, a loss tangent of $\tan\delta = 0$, and the height of the substrate is $h = 1.27$ mm. The substrate is a grounded dielectric with the excitation provided by a narrow y -directed slot in the ground plane. The slot is centered at the location $(x_0 = a/2, y_0 = 0)$. The slot in the ground plane is modeled as an infinitesimal magnetic dipole. The length of the patch is $L = 0.250$ cm, the width is $W = L/5$, and the dimensions of the unit cell are given by $a = 2.28859$ cm and $b = 1.22367$ cm. We can see from Figs. 3.24 – 3.27 that there are spikes extending out of the cross-section around $\phi \approx 85^\circ$; this is due to the

grating lobes in the pattern. The cross-section of the main beam is highly elliptical with the beam much wider in the H-plane than in the E-plane.

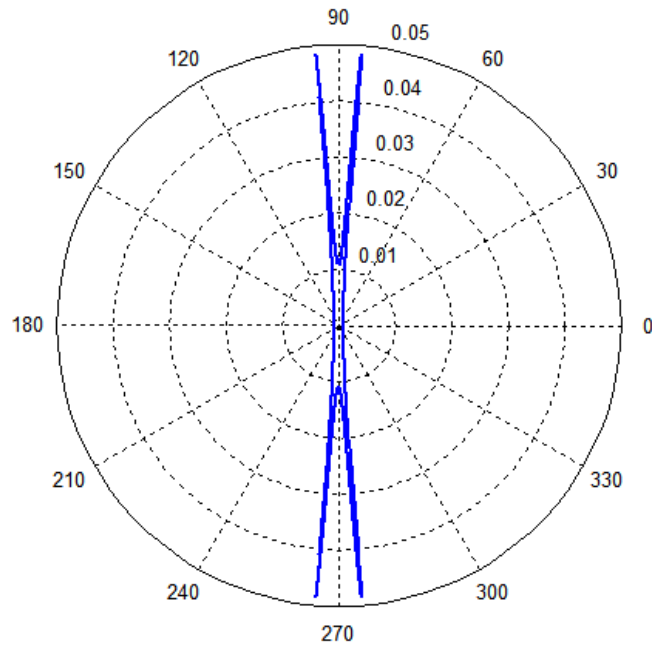


Fig. 3.24. Cross-section of beam at a power level of -3 dB.

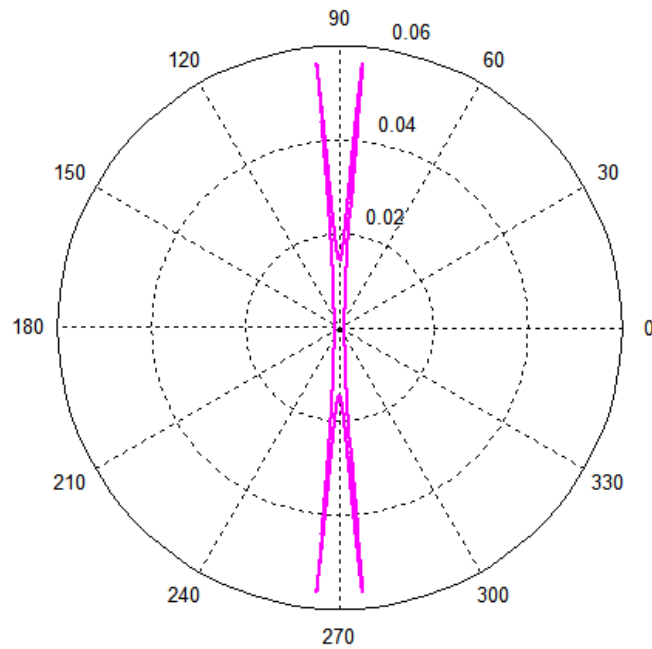


Fig. 3.25. Cross-section of beam at a power level of -6 dB.

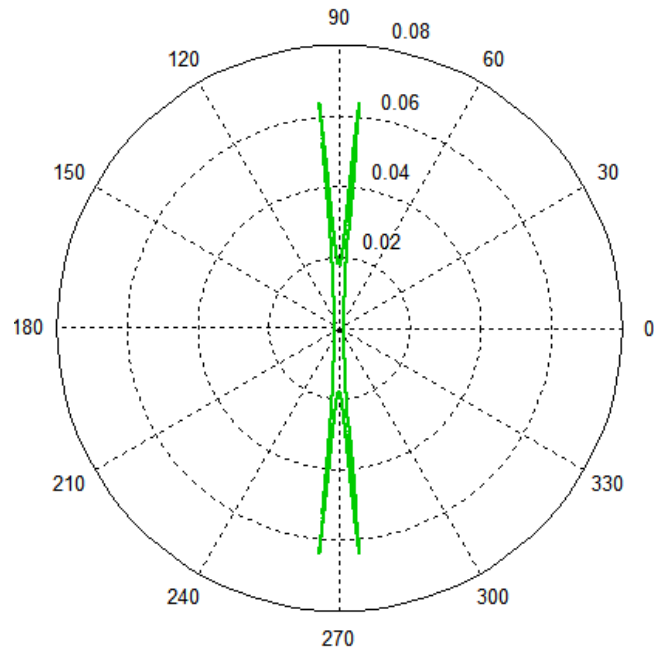


Fig. 3.26. Cross-section of beam at a power level of -9 dB.

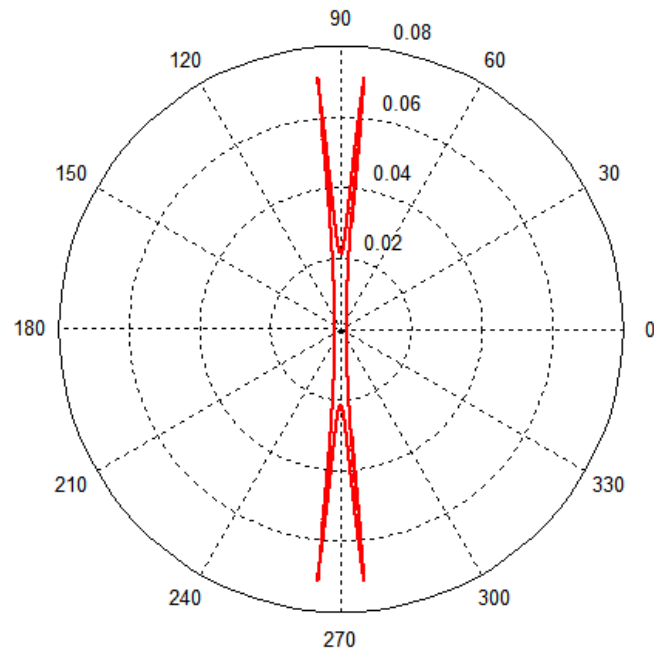


Fig. 3.27. Cross-section of beam at a power level of -12 dB.

3.7 Variation of Beamwidth and Enhancement Factor with the Length of the Patches

The dependence of the beamwidth of the radiation patterns in the E-plane and the H-plane and the Enhancement Factor (EF) on the dimensions of the patches of the 2D periodic LWA are explored here. The parameters of the 2D periodic LWA are as follows: The frequency is $f = 12$ GHz, the substrate has a relative permittivity of $\epsilon_r = 9.8$, a loss tangent of $\tan\delta = 0.002$, and the height of substrate is $h = 1.27$ mm. The substrate is a grounded dielectric with the excitation provided by a narrow y -directed slot in the ground plane. The slot is centered at the location $(x_0 = a/2, y_0 = 0)$. The slot in the ground plane is modeled as an infinitesimal magnetic dipole. The length of the patches L is varied, while the width is $W = L/5$. For each different length of patch L , the length of the unit cell a is adjusted for maximum power density at broadside while maintaining the width of unit cell as $b = a/1.2$. The plot of variation of the beamwidths and enhancement factor with respect to length of the patches for the lossy case is given in Fig. 3.28 and the same plot for the lossless case is given in Fig. 3.29. Note that the enhancement factor for the lossless case in Fig. 3.28 is plotted on a log scale.

In Fig. 3.28, for the lossy case, the enhancement factor and the beamwidths decrease as the dimensions of the patches are made very small. Although the beam becomes very narrow for very small lengths of patches, the proportion of the space wave increases and therefore the enhancement factor decreases. In Fig. 3.29 on the other hand, as the length of patches becomes very small, the beamwidths decrease rapidly and the enhancement factor increases monotonically.

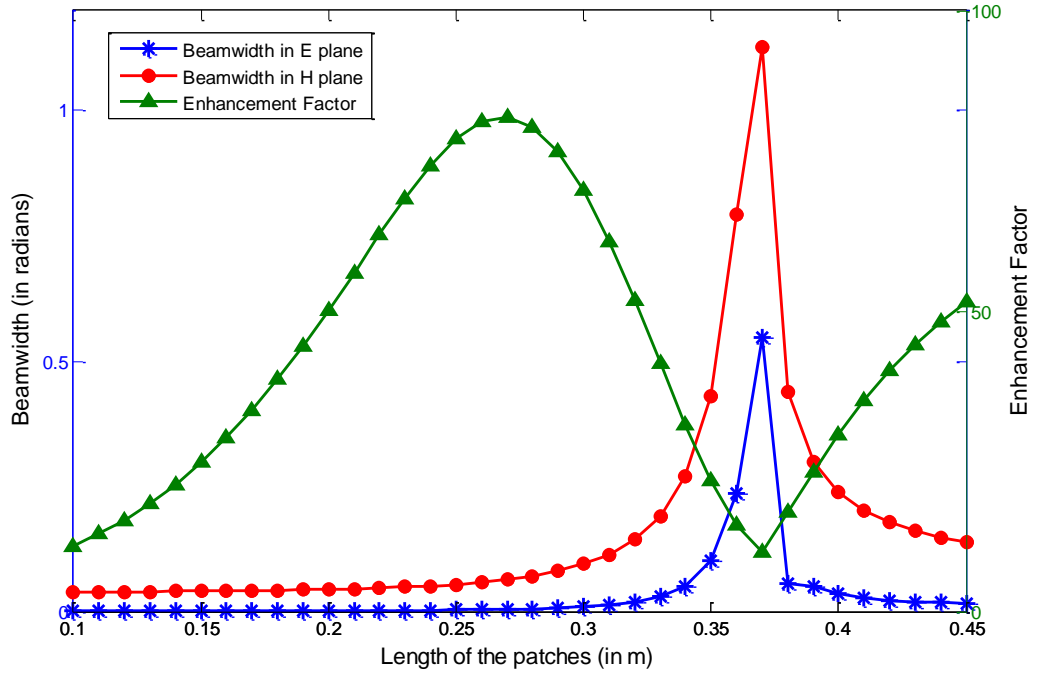


Fig. 3.28. Beamwidths and enhancement factors vs. length of patches for a lossy substrate.

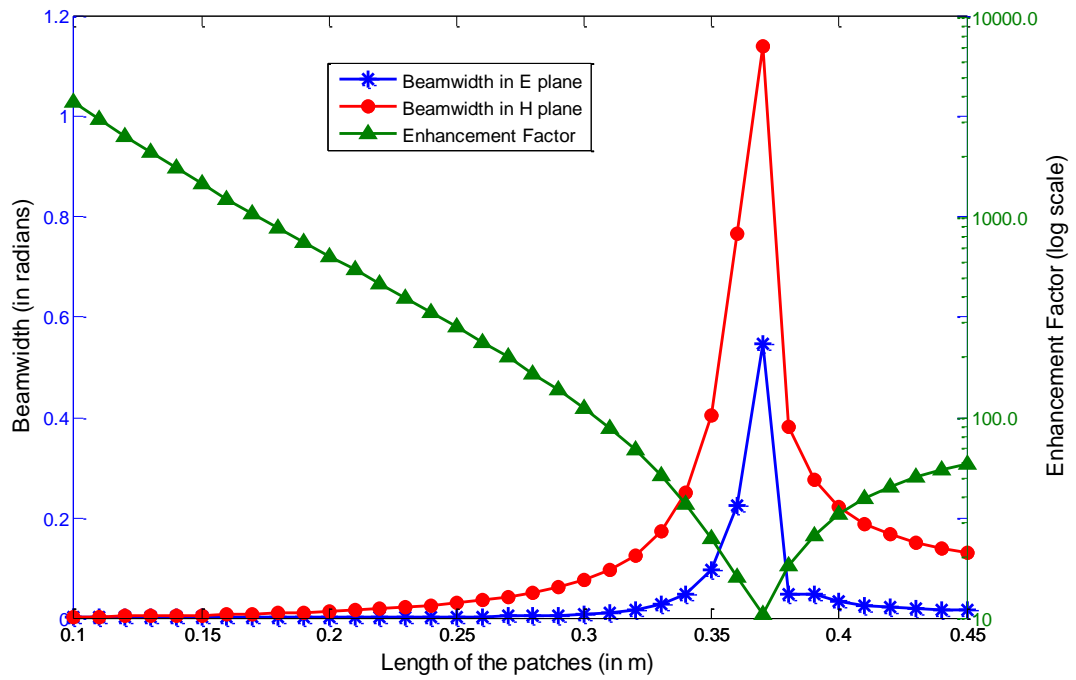


Fig. 3.29. Beamwidths and enhancement factors vs. length of patches for a lossless substrate.

3.8 Bandwidth, Figure of Merit, and Normalized Tolerance of the 2D Periodic Leaky-Wave Antenna

The bandwidth of the 2D periodic LWA for both lossy and lossless substrates is calculated here. The parameters of the 2D periodic LWA taken in this section are as follows: The frequency is $f = 12$ GHz, the substrate has a relative permittivity of $\epsilon_r = 9.8$, and the height of substrate is $h = 1.27$ mm. The substrate is a grounded dielectric with the excitation provided by a narrow y -directed slot in the ground plane. The slot is centered at the location $(x_0 = a/2, y_0 = 0)$. The slot in the ground plane is modeled as an infinitesimal magnetic dipole. The length of the patches L is varied, while the width is $W = L/5$. For each different length of patch L , the length of the unit cell a is adjusted for maximum power density at broadside while maintaining the width of unit cell as $b = a/1.2$.

The figure of merit of the structure is defined as the fractional bandwidth times the maximum directivity of the structure, and is usually calculated for the lossless substrate. The normalized tolerance of the 2D periodic leaky-wave antenna is defined as the difference in the upper and lower values of a (length of the unit cell) at which the power level at broadside drops by 3 dB from maximum (or optimum), divided by the optimum a , expressed as a percentage. It is a measure of the degree to which the beam is sensitive to the length of the unit cell a . For the percentage bandwidth, the upper and lower bounds of frequency are taken to be the points where the power level at broadside drops by 3 dB from maximum (or optimum).

The exact directivity D_0 of the structure at broadside is calculated by integrating over the radiated power density, calculated using the reciprocity method. The approximate

directivity of a planar array is sometimes calculated from the beamwidths in the E-plane and H-plane using the formula [62]

$$D_0^A = \frac{\pi^2}{\Theta_E \Theta_H}, \quad (3.1)$$

where Θ_E is the beamwidth in the E-plane and Θ_H is the beamwidth in the H-plane (both in radians).

Table 3.1 lists the bandwidth, the figure of merit, the exact and approximate directivities, and the beamwidths in the E-plane and the H-plane for different lengths L of the patches. Here the substrate is lossless. The Table 3.1 also gives the optimized a for maximum power density at broadside for each given length L of the patches.

Table 3.1. Bandwidth, figure of merit, exact directivity, approximate directivity, and beamwidths in the E-plane and the H-plane for the 2D periodic leaky-wave antenna for different lengths L of the patches, for a lossless substrate.

Length of the patches L (cm)	Length of the unit cell a (cm)	Bandwidth (%)	D_0	Figure of merit	Beamwidth in the E-plane (radians)	Beamwidth in the H-plane (radians)	D_0^A
0.25	2.2970	0.013667	11297	1.5439	0.001679	0.02884	203823
0.30	2.2727	0.085417	1672.9	1.4289	0.007288	0.07558	17918
0.40	2.4180	0.53525	221.87	1.1875	0.03248	0.2216	1371.2

From Table 3.1 we see that the approximate directivity formula, which is based on the beamwidths in the E-plane and the H-plane, does not work well. This is because the

beam is highly asymmetric and, even more importantly, there is a lot of space wave radiation and grating lobes in the pattern. Also, it is seen that the figure of merit decreases slightly as the length of the patches is increased.

Table 3.2 lists the bandwidth, normalized tolerance, and beamwidths in the E-plane and the H-plane for a lossy substrate with loss tangent $\tan\delta = 0.002$, for different lengths L of the patches. Table 3.2 also gives the optimized a for maximum power density at broadside for each given length L of the patches.

Table 3.2. Bandwidth, normalized tolerance, and beamwidths in the E-plane and the H-plane for the 2D periodic leaky-wave antenna for different lengths L of the patches, for a lossy substrate.

Length of the patches L (cm)	Length of the unit cell a (cm)	Bandwidth (%)	Normalized Tolerance (%)	Beamwidth in the E-plane (radians)	Beamwidth in the H-plane (radians)
0.25	2.2971	0.049333	0.06554	0.003196	0.05404
0.30	2.2728	0.13592	0.19613	0.0092	0.0944
0.40	2.4176	0.60583	0.88194	0.03466	0.2376

From Table 3.2 we observe that the normalized tolerance of the 2D periodic leaky-wave antenna is quite low but increases when the beam is broader (which usually occurs when the size of the patches is larger). From Tables 3.1 and 3.2 we see that the bandwidth increases with the length of the patches and is larger for the lossy substrate, compared to the lossless substrate with the same length of patches, especially for smaller patches.

CHAPTER 4 PROPERTIES OF THE LEAKY WAVE IN THE 2D PERIODIC MICROWAVE ANTENNA

In this chapter we delve deeper into the nature and characteristics of the leaky wave in different azimuthal directions, i.e., angles ϕ . Here, we have tried to understand the basic physics of the leaky wave and explain how the leaky wave leads to the formation of the main beam and the grating lobes. All of the results presented in this chapter have been computed with one basis function in Eqs. (2.18) and (2.83) for the surface current distribution on the surface of the patches.

4.1 Current Distribution on the Patches

The current at the center of the patches in the 2D periodic leaky-wave antenna is calculated using the array scanning method (ASM) discussed in Section 2.3 of Chapter 2 and is plotted in Fig. 4.1 and Fig. 4.2 for the E-plane (along the x -axis) and H-plane (along the y -axis), respectively. The magnitude of the current distribution on the patches, given by the red curve in Fig. 4.1 and Fig. 4.2, is normalized. The blue curve gives the asymptotic distribution of the leaky wave based on the exponential decay of the fundamental harmonic of the leaky wave, and an appropriate algebraic decay is also added. For the E-plane the leaky-wave field distribution over the surface of the dielectric is $e^{-\alpha_E x} / x^{1/2}$ and for the H-plane it is $e^{-\alpha_H y} / y^{3/2}$, where α_E and α_H are the attenuation constants of the leaky wave in the E-plane (along the x -axis) and H-plane (along the y -axis), respectively. Along the surface of the dielectric, the leaky wave interferes with the space wave, therefore the current distribution on the patches is not smooth and displays

an interference pattern. In the absence of interference with the space wave, the current distribution from ASM (the red curve) would closely match the blue curve in Fig. 4.1 and Fig. 4.2. In this case the design parameters for the 2D periodic leaky-wave antenna are as follows. The frequency is $f = 12$ GHz. The substrate has a relative permittivity of $\epsilon_r = 9.8$, the loss tangent is $\tan\delta = 0.002$, and the height of substrate is $h = 1.27$ mm. The substrate is a grounded dielectric with the excitation provided by a narrow y -directed slot in the ground plane, which is centered at the location $(x_0 = a/2, y_0 = 0)$. The length of each patch is $L = 0.40$ cm, the width is $W = L/5$, and the dimensions of the unit cell are given by $a = 2.41758$ cm and $b = a/1.2$. The design has been optimized for maximum power density radiated at broadside. In this case the attenuation constants in the E-plane and H-plane are $\alpha_E = 3.04402 = 0.0121034k_0$ and $\alpha_H = 20.6845 = 0.082244k_0$ respectively, where k_0 is the wavenumber in free space at this frequency.

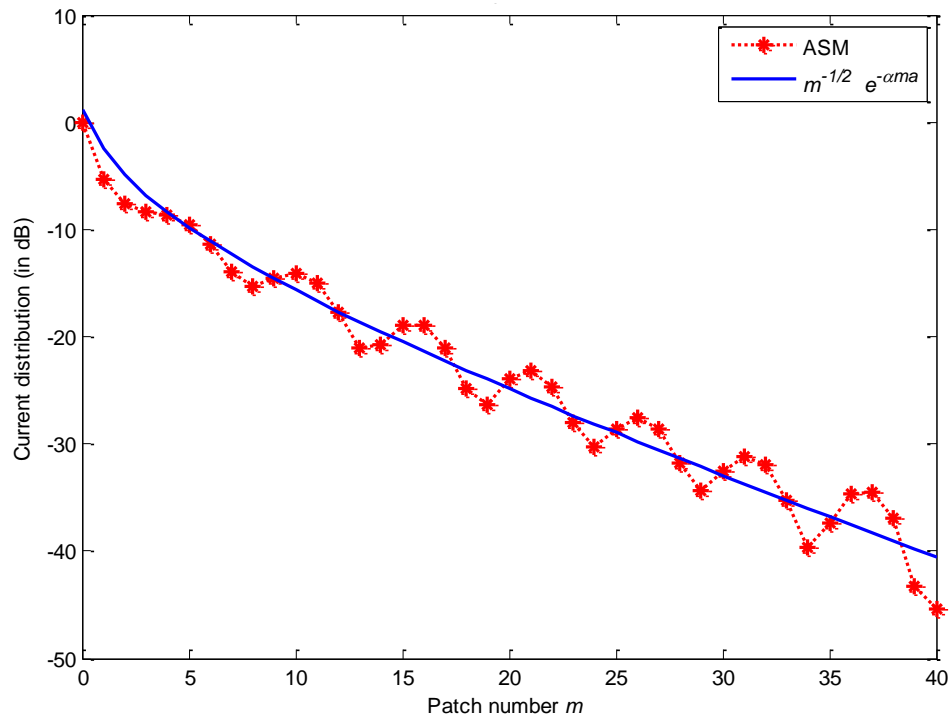


Fig. 4.1. Current distribution from ASM on the patches in the E-plane.

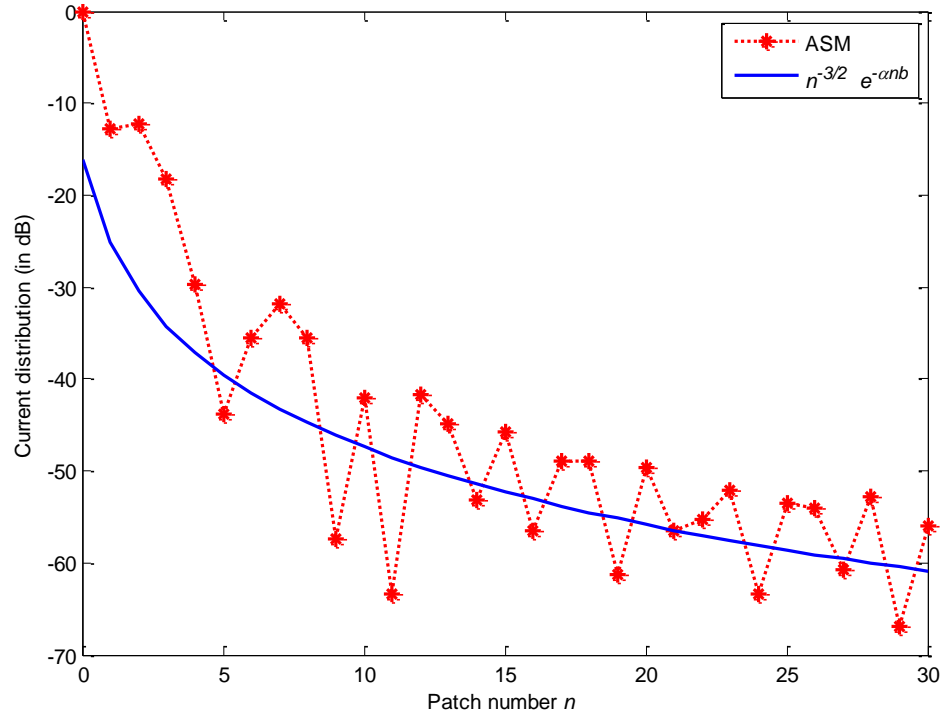


Fig. 4.2. Current distribution from ASM on the patches in the H-plane.

In Fig. 4.3, the current distribution obtained from simulation in Ansys Designer is compared with the current distribution obtained from ASM in the E-plane (along the x -axis). The current distribution obtained from both Designer and ASM show a similar interference pattern with the same beat period. The agreement is fairly good down to a level of about -30 dB. For the case presented in Fig. 4.3, the design parameters for the 2D periodic leaky-wave antenna are as follows. The frequency is $f = 12$ GHz. The substrate has a relative permittivity of $\epsilon_r = 10$, the loss tangent is $\tan\delta = 0.05$, and the height of substrate is $h = 1.24915$ mm. The substrate is grounded dielectric with the excitation provided by a narrow y -directed slot in the ground plane which is centered at the location $(x_0 = a/2, y_0 = 0)$. The length of each patch is $L = 0.370$ cm, the width is $W = L/4.8$, and the dimensions of the unit cell are given by $a = 2.39825$ cm and $b = a/1.2$.

The design has been optimized for maximum power density radiated at broadside. In this case the attenuation constant in the E-plane is $\alpha_E = 10.3674 = 0.041222k_0$.

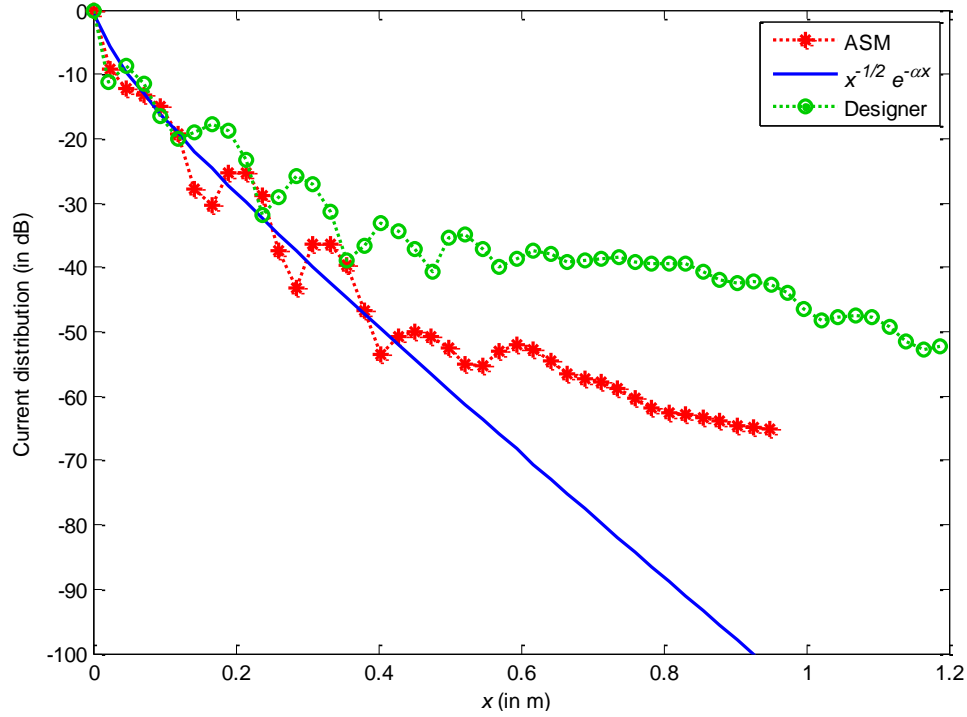


Fig. 4.3. Current distribution from ASM and Designer on the patches in the E-plane.

4.2 Relation Between the Propagation and Attenuation Constants of the Leaky Mode and the Radiation at Broadside

The wavenumber of the leaky wave for a given azimuthal angle of propagation ϕ with the x -axis is calculated using the method described in Section 2.4 of Chapter 2. The real part of the wavenumber is the propagation constant β , and the negative of the imaginary part of the wavenumber is the attenuation constant α . In the E-plane (along the x -axis), the $(-1, 0)$ Floquet harmonic of the leaky mode produces the radiation and is the dominant radiating wave, whereas for the H plane (along the y -axis), the $(0, -1)$ Floquet

harmonic of the leaky mode is the radiating wave. The normalized values of the propagation constant β and attenuation constant α of the radiating waves ($(-1, 0)$ for the E-plane and $(0, -1)$ for the H-plane) are plotted along with the power density radiated in the far field at broadside with respect to a variation of the spacing between the patches a in the E-plane (along the x -axis) in Fig. 4.4, and the spacing between the patches b in the H-plane (along the y -axis) in Fig. 4.5. The following design parameters for the 2D periodic leaky-wave antenna have been assumed: the frequency is $f = 12$ GHz, the substrate is chosen to have a relative permittivity of $\epsilon_r = 9.8$, the substrate is lossless, i.e., the loss tangent is $\tan\delta = 0$, and the height of the substrate is $h = 1.27$ mm. The substrate is a grounded dielectric with the excitation provided by a narrow y -directed slot in the ground plane. The slot is centered at the location $(x_0 = a/2, y_0 = 0)$. The length of each patch is $L = 0.250$ cm, the width is $W = L/5$, and the dimensions of the unit cell are given by $a = 2.29705$ cm and $b = a/1.2$. This design has been optimized for maximum power density radiated at broadside.

In Fig. 4.4, it can be observed that when the power radiated in the far field region at broadside is maximum, the normalized propagation constant and the normalized attenuation constant have the same magnitude. Also, a region of open stopband can be observed where the phase constant is very low and decreases to zero while the attenuation constant has a much higher value than usual. This is the exact behavior that has been observed in 1D periodic leaky-wave antennas [63].

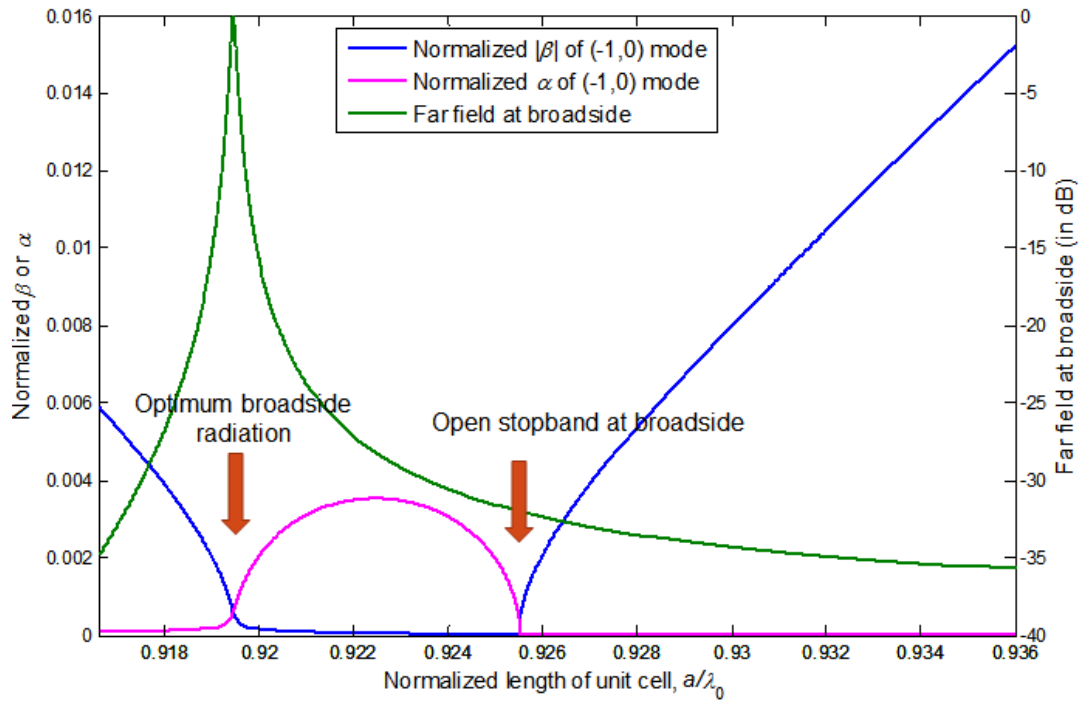


Fig. 4.4. Plot of normalized α and β along the x -axis and the power radiated at broadside vs. a .

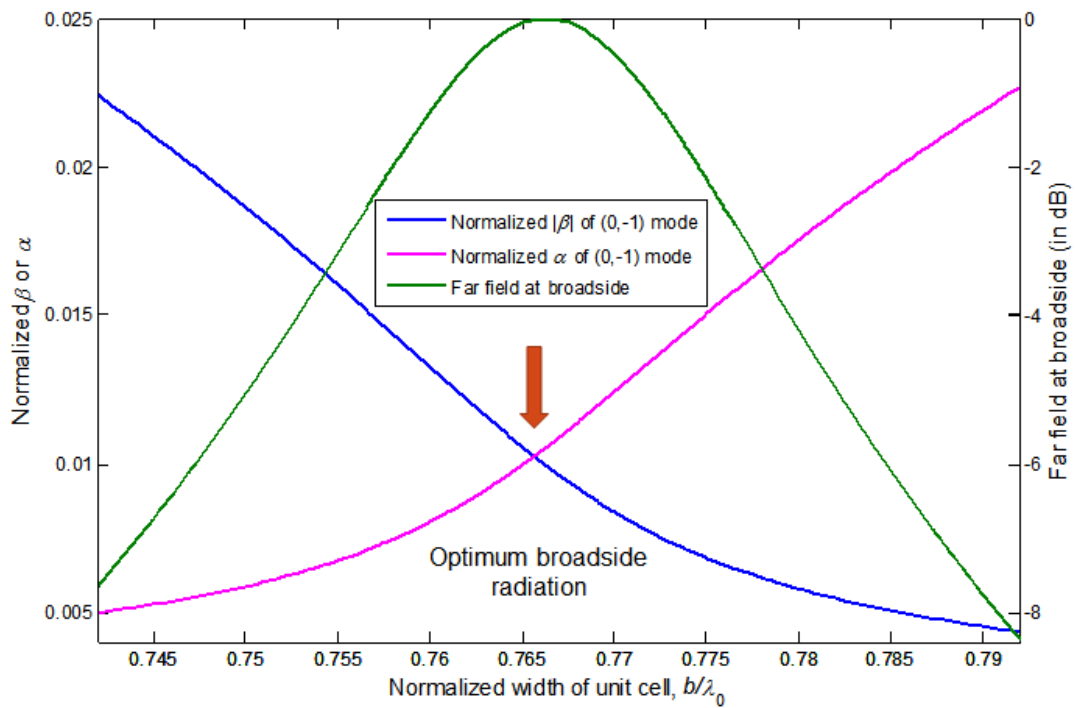


Fig. 4.5. Plot of normalized α and β along the y -axis and the power radiated at broadside vs. b .

In Fig. 4.5, it can again be observed that when the power radiated in the far field region at broadside is maximum, the normalized propagation constant and the normalized attenuation constant have the same magnitude. This is the same property as the leaky mode along the x -axis observed in Fig. 4.4; but unlike the leaky mode along the x -axis, no open stopband region is observed for the leaky mode along the y -axis.

4.3 Dispersion Behaviour – Variation of Leaky-Mode Wavenumber as a Function of the Azimuthal Angle ϕ

The wavenumber of the leaky mode that produces the radiation in the 2D periodic leaky-wave antenna varies with the radial angle of propagation ϕ . We take the following design parameters for the 2D periodic leaky-wave antenna: the frequency is $f = 12$ GHz, the substrate is chosen to have a relative permittivity of $\epsilon_r = 9.8$, the substrate is lossless, i.e., the loss tangent is $\tan\delta = 0$ and the height of the substrate is $h = 1.27$ mm. The substrate is a grounded dielectric with the excitation provided by a narrow y -directed slot in the ground plane. The slot is centered at the location $(x_0 = a/2, y_0 = 0)$. The length of each patch is $L = 0.250$ cm, the width is $W = L/5$, and the dimensions of the unit cell are given by $a = 2.29705$ cm and $b = a/1.2$. This design has been optimized for maximum power density radiated at broadside. The normalized propagation constant of the fundamental harmonic of the leaky mode is plotted in Fig. 4.6 with respect to the angle ϕ . Similarly, the normalized attenuation constant of the fundamental harmonic of the leaky mode is plotted in Fig. 4.7 with respect to the angle ϕ .

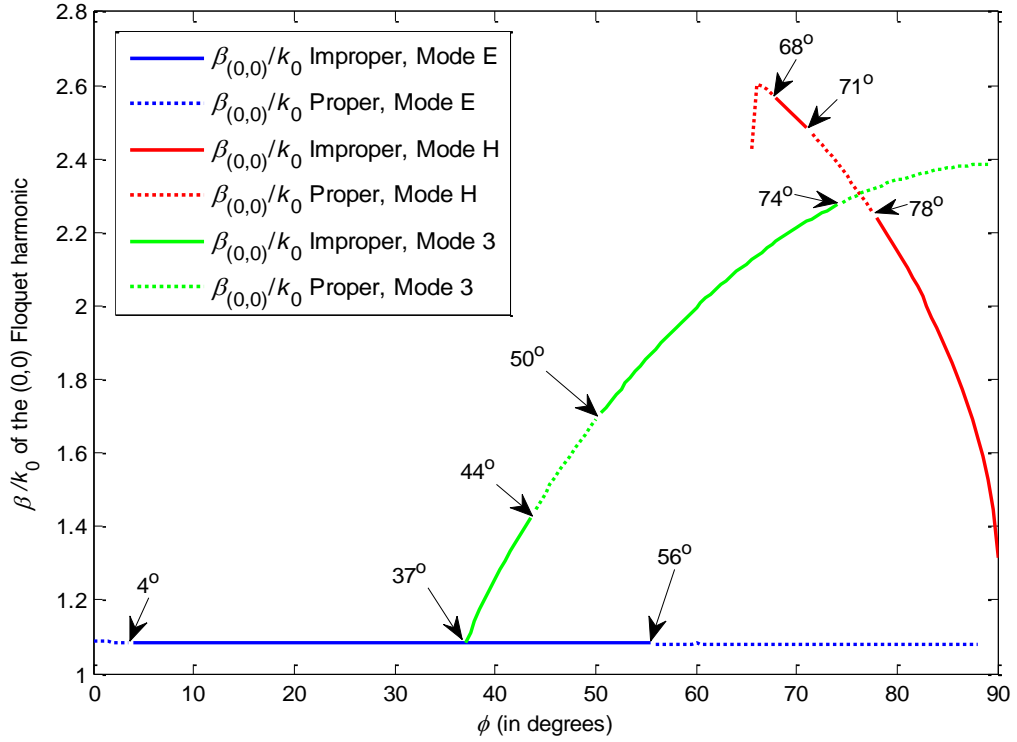


Fig. 4.6. Dispersion diagram showing the variation of the phase constant with ϕ .

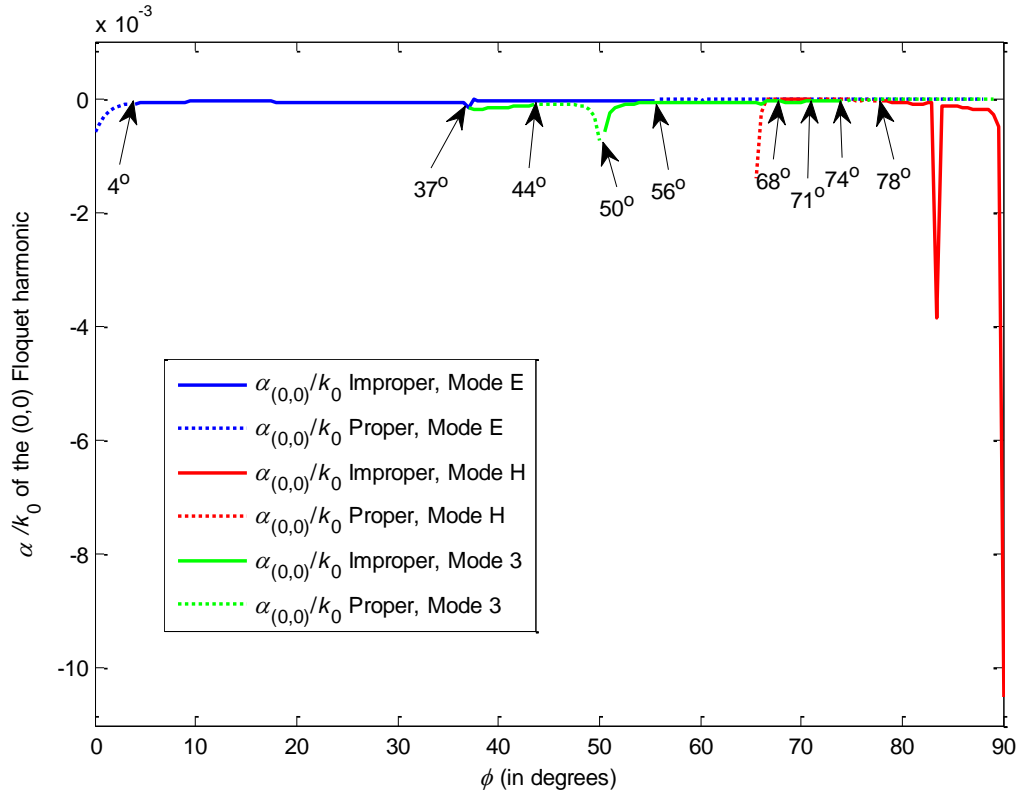


Fig. 4.7. Dispersion diagram showing the variation of the attenuation constant with ϕ .

From Figs. 4.6 and 4.7, we see that there are three separate leaky modes. The one that is dominant along the x -axis, i.e., in the E-plane, is shown in blue and is termed the E-plane mode. The one that is dominant along the y -axis, i.e., in the H-plane is shown in red and is termed the H-plane mode. Then there is the third somewhat more mysterious mode that is shown in green. The E-plane leaky mode produces the beam in the E-plane and the H-plane leaky mode produces the beam in the H-plane.

4.4 CAD Formula to Predict the Shape of the Main Beam at Arbitrary Angle ϕ

The CAD formula for calculating the radiation pattern due to the leaky wave in Section 2.6 of Chapter 2 can be used to plot the shape of the main beam for arbitrary angle ϕ . We take the following design parameters for the 2D periodic leaky-wave antenna: the frequency is $f = 12$ GHz, the substrate is chosen to have a relative permittivity of $\epsilon_r = 9.8$, the substrate is lossless, i.e., the loss tangent is $\tan\delta = 0$, and the height of the substrate is $h = 1.27$ mm. The substrate is a grounded dielectric with the excitation provided by a narrow y -directed slot in the ground plane. The slot is centered at the location $(x_0 = a/2, y_0 = 0)$. The length of each patch is $L = 0.250$ cm, the width is $W = L/5$, and the dimensions of the unit cell are given by $a = 2.29705$ cm and $b = a/1.2$. This design has been optimized for maximum power density radiated at broadside. The wavenumber of the radiating $(-1, 0)$ harmonic of the leaky wave along the x -axis is $k_p^{LW} = (-6.0401 \times 10^{-4} - j5.7653 \times 10^{-4})k_0$, where k_0 is the wavenumber of free space at this frequency. The leaky-wave beam pattern from the CAD formula for the E-plane mode is compared with the exact radiation pattern from reciprocity in Figs. 4.8, 4.9, 4.10 and 4.11 for $\phi = 45^\circ$, $\phi = 60^\circ$, $\phi = 75^\circ$, and $\phi = 85^\circ$ respectively.

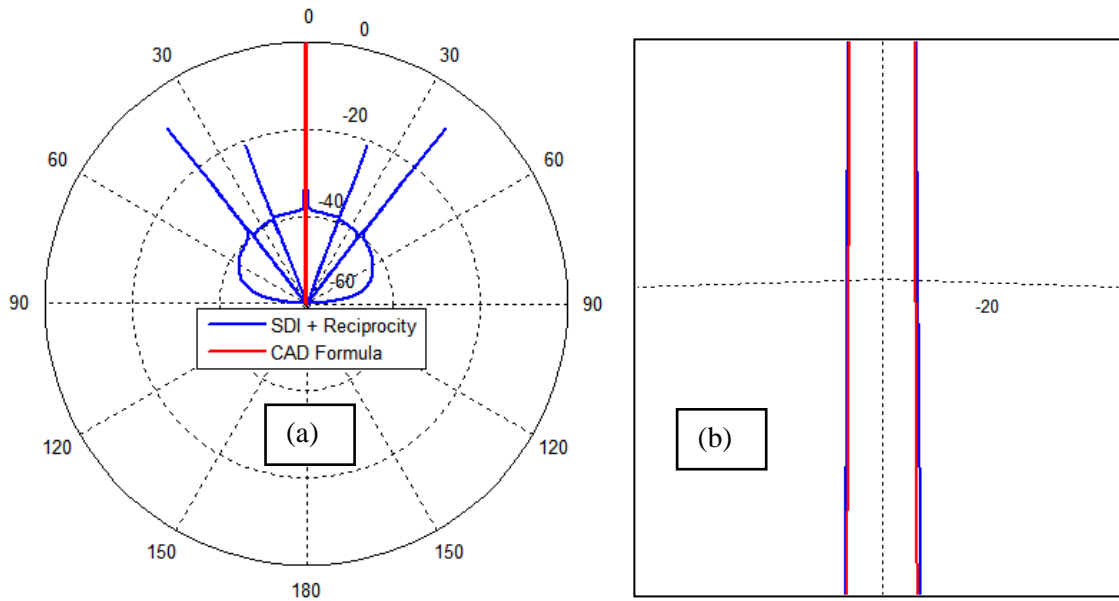


Fig. 4.8. (a) Comparison of the main beam from reciprocity and the CAD formula for an angle $\phi = 45^\circ$. (b) An expanded view of the main beam around the -20 dB power level.

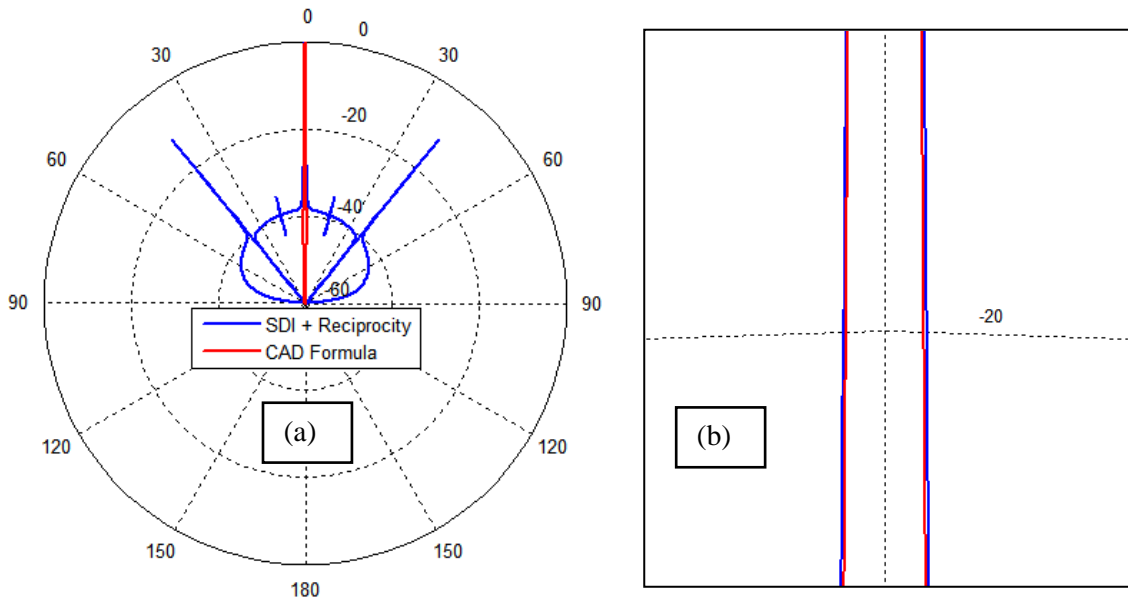


Fig. 4.9. (a) Comparison of the main beam from reciprocity and the CAD Formula for an angle $\phi = 60^\circ$. (b) An expanded view of the main beam around the -20 dB power level.

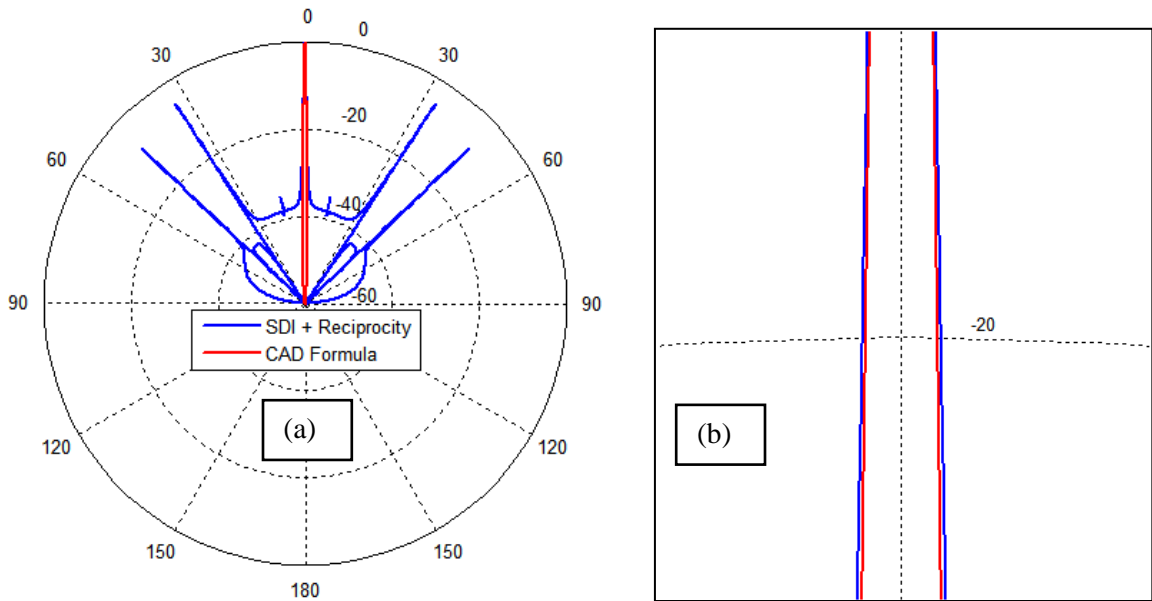


Fig. 4.10. (a) Comparison of the main beam from reciprocity and the CAD formula for an angle $\phi = 75^\circ$. (b) An expanded view of the main beam around the -20 dB power level.

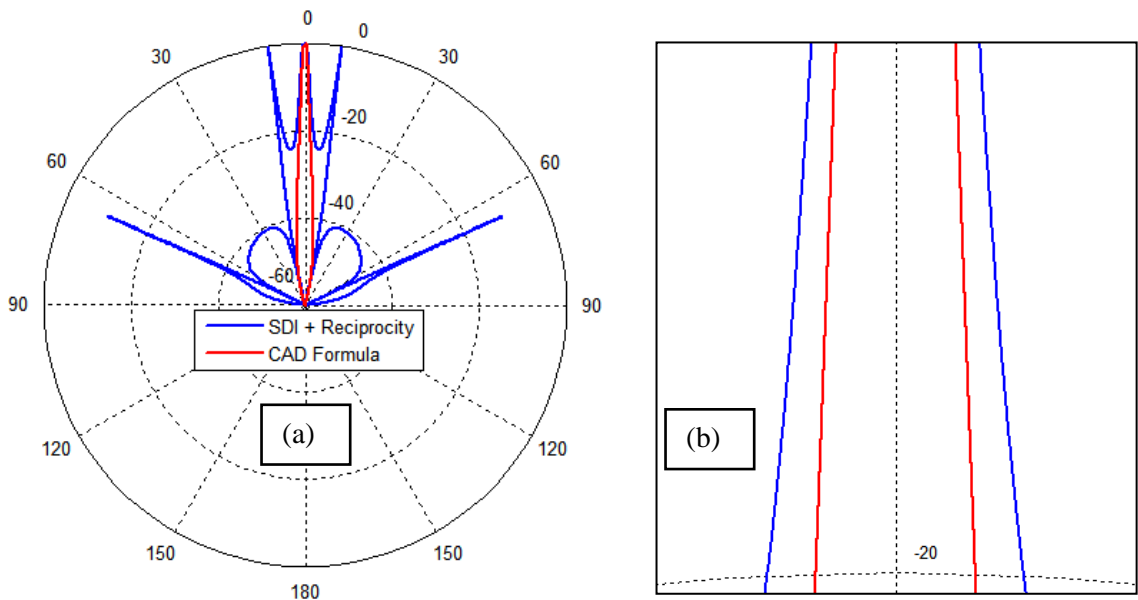


Fig. 4.11. (a) Comparison of the main beam from reciprocity and the CAD formula for an angle $\phi = 85^\circ$. (b) An expanded view of the main beam around the -20 dB power level.

It can be observed from Figs. 4.8, 4.9, 4.10 and 4.11 that the main beam is mainly due to the bi-directional leaky wave travelling along the x -axis and for smaller values of ϕ

(less than 85° in this case), the leaky-wave beam pattern can be predicted accurately by applying the CAD formula with the E-plane leaky mode. However, for ϕ close to 90° (beyond 85° in this case), the leaky mode travelling along the y -axis starts to dominate and mainly influences the shape of the main beam. The patterns from the CAD formula and reciprocity agree very well at the -20 dB power level and even better near the 0 dB power level. The agreement is very good until $\phi = 85^\circ$.

4.5 Formation of the Grating Lobes and Predicting their Location

Methods A and B described in Section 2.7 of Chapter 2 are applied here to explore the origins of the narrow grating lobes that are often observed in the radiation pattern. We take the following design parameters for the 2D periodic leaky-wave antenna: the frequency is $f = 12$ GHz, the substrate is chosen to have a relative permittivity of $\epsilon_r = 9.8$, the substrate is lossless, i.e., the loss tangent is $\tan\delta = 0$, and the height of the substrate is $h = 1.27$ mm. The substrate is a grounded dielectric with the excitation provided by a narrow y -directed slot in the ground plane. The slot is centered at the location ($x_0 = a/2$, $y_0 = 0$). The length of each patch is $L = 0.250$ cm, the width is $W = L/5$, and the dimensions of the unit cell are given by $a = 2.29705$ cm and $b = a/1.2$. This design has been optimized for maximum power density radiated at broadside.

Usually there are up to three grating lobes that can be observed in the radiation pattern. A few cases are presented next that successfully predict the occurrence of grating lobes in the pattern using Methods A and B and give us some idea about the mechanism of formation of the grating lobes in the radiation pattern.

Case 1

Here the leaky wave travelling radially along the angle $\phi_{00} = 50^\circ$ is considered, and the $(-1, -1)$ Floquet harmonic of the E-plane mode (the perturbed surface-wave mode) is considered, which has a wavenumber for the fundamental Floquet harmonic as

$$k_{(0,0)}^{LW} = (1.0819 - j0.00004638)k_0 = 272.11303 - j0.011664.$$

Then, from Eq. (2.161), the phase constant vector of the $(-1, -1)$ Floquet harmonic is at an angle

$$\phi = \tan^{-1} \left(\frac{\beta_{(0,0)}^{LW} \sin \phi_{00} - 2\pi/b}{\beta_{(0,0)}^{LW} \cos \phi_{00} - 2\pi/a} \right) = 50.53^\circ. \quad (4.1)$$

From Eq. (2.160), the magnitude of the phase constant vector of the $(-1, -1)$ Floquet harmonic is

$$|\beta_{(-1,-1)}^{LW}| = \sqrt{\left(\beta_{(0,0)}^{LW} \cos \phi_{00} - \frac{2\pi}{a} \right)^2 + \left(\beta_{(0,0)}^{LW} \sin \phi_{00} - \frac{2\pi}{b} \right)^2} = 155.1632. \quad (4.2)$$

The wavenumber of the $(-1, -1)$ Floquet harmonic is therefore

$$k_{(-1,-1)}^{LW} = 155.1632 - j0.011664 \cos(50^\circ - 50.53^\circ). \quad (4.3)$$

From Eq. (2.162), the angle of the grating lobe with the vertical axis due to the $(-1, -1)$ Floquet harmonic is

$$\theta_g = 0.6649 \text{ rad} = 38.09^\circ. \quad (4.4)$$

Method A works well here since the actual grating lobes are at roughly around $\theta = 38.09^\circ$ and 15° . The Method B CAD formula is also very successful in predicting the location of the grating lobes as well, as can be seen from the radiation patterns for $\phi = 50.53^\circ$ shown in Fig. 4.12.

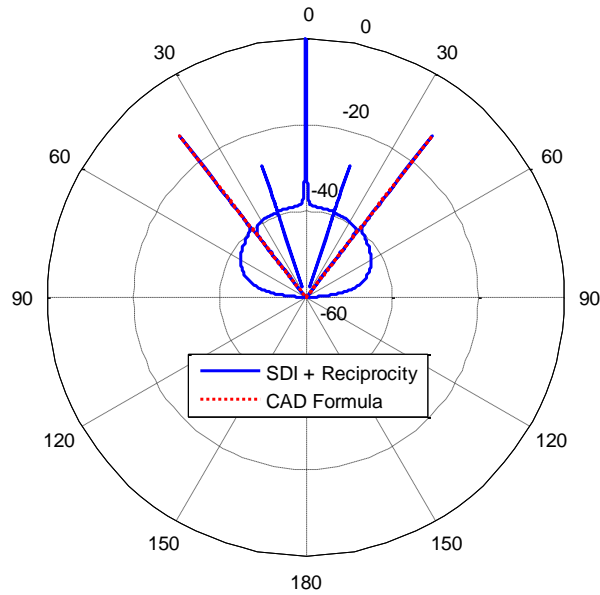


Fig. 4.12. Grating lobe predicted using the CAD formula for case 1.

Case 2

Here the leaky wave travelling radially along the angle $\phi_{00} = 18^\circ$ is considered, and the $(-1, -1)$ Floquet harmonic of the E-plane mode (the perturbed surface-wave mode) is considered, which has a wavenumber for the fundamental Floquet harmonic as

$$k_{(0,0)}^{LW} = (1.0838 - j0.000058205)k_0 = 272.5841 - j0.01464.$$

Then, from Eq. (2.161), the phase constant vector of the $(-1, -1)$ Floquet harmonic is at an angle

$$\phi = \tan^{-1} \left(\frac{\beta_{(0,0)}^{LW} \sin \phi_{00} - 2\pi/b}{\beta_{(0,0)}^{LW} \cos \phi_{00} - 2\pi/a} \right) = 86.65^\circ. \quad (4.5)$$

From Eq. (2.160), the magnitude of the phase constant vector of the $(-1, -1)$ Floquet harmonic is

$$|\underline{\beta}_{(-1,-1)}^{LW}| = \sqrt{\left(\beta_{(0,0)}^{LW} \cos \phi_{00} - \frac{2\pi}{a} \right)^2 + \left(\beta_{(0,0)}^{LW} \sin \phi_{00} - \frac{2\pi}{b} \right)^2} = 244.424. \quad (4.6)$$

The wave number of the $(-1, -1)$ Floquet harmonic is therefore

$$k_{(-1,-1)}^{LW} = 244.424 - j0.01464 \cos(18^\circ - 86.65^\circ). \quad (4.7)$$

From Eq. (2.162) the angle of the grating lobe with the vertical axis due to the $(-1, -1)$ Floquet harmonic is

$$\theta_g = 1.333 \text{ rad} = 76.37^\circ. \quad (4.8)$$

Method A works well here since the actual grating lobes are at roughly $\theta = 76^\circ$. The Method B CAD formula is also very successful in predicting the location of the grating lobes, as can be seen from the radiation patterns for $\phi = 86.65^\circ$ shown in Fig. 4.13.

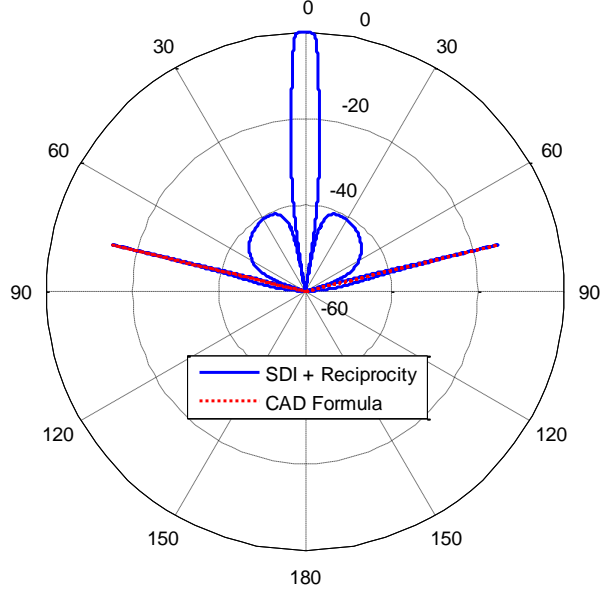


Fig. 4.13. Grating lobe predicted using the CAD formula for case 2.

Case 3

Here the leaky wave travelling radially along the angle $\phi_{00} = 18^\circ$ is considered, and the $(-1, 0)$ Floquet harmonic of the E-plane mode (the perturbed surface-wave mode) is considered, which has a wavenumber for the fundamental Floquet harmonic as

$$k_{(0,0)}^{LW} = (1.0838 - j0.000058205)k_0 = 272.58407 - j0.01464.$$

Then, from Eq. (2.161) the phase constant vector of the $(-1, 0)$ Floquet harmonic is at an angle

$$\phi = \tan^{-1} \left(\frac{\beta_{(0,0)}^{LW} \sin \phi_{00}}{\beta_{(0,0)}^{LW} \cos \phi_{00} - 2\pi/a} \right) = -80.37^\circ. \quad (4.9)$$

From Eq. (2.160), the magnitude of the phase constant vector of the $(-1, 0)$ Floquet harmonic is

$$|\underline{\beta}_{(-1,0)}^{LW}| = \sqrt{\left(\beta_{(0,0)}^{LW} \cos \phi_{00} - \frac{2\pi}{a}\right)^2 + \left(\beta_{(0,0)}^{LW} \sin \phi_{00}\right)^2} = 85.4366. \quad (4.10)$$

The wavenumber of the $(-1, 0)$ Floquet harmonic is therefore

$$k_{(-1,0)}^{LW} = 85.4366 - j0.01464 \cos(18^\circ + 80.37^\circ). \quad (4.11)$$

From Eq. (2.162), the angle of the grating lobe with the vertical axis due to the $(-1, 0)$ Floquet harmonic is

$$\theta_g = 0.3466 \text{ rad} = 19.86^\circ. \quad (4.12)$$

Method A works well here since the actual grating lobes are at $\theta = 19.86^\circ$ and 53.33° . The Method B CAD formula is also very successful in predicting the location of the grating lobes, as well as can be seen from the radiation patterns for $\phi = -80.37^\circ$ shown in the Fig. 4.14.

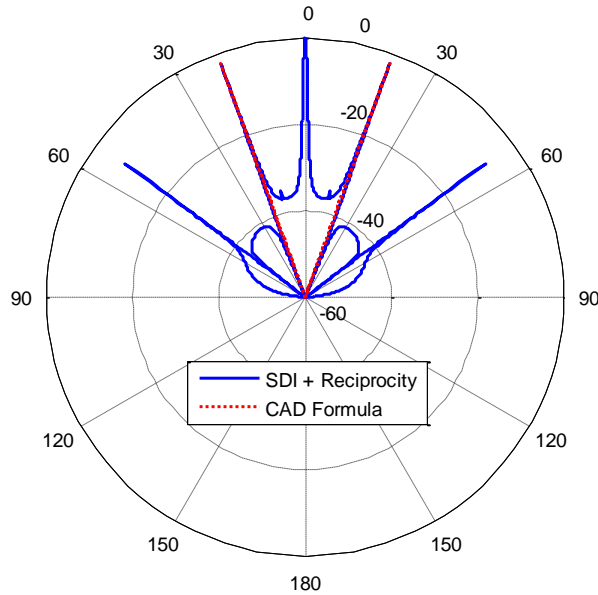


Fig. 4.14. Grating lobe predicted using the CAD formula for case 3.

Case 4

Here the leaky wave travelling radially along the angle $\phi_{00} = 30^\circ$ is considered, and the $(-1, 0)$ Floquet harmonic of the E-plane mode (the perturbed surface-wave mode) is considered, which has a wavenumber for the fundamental Floquet harmonic as

$$k_{(0,0)}^{LW} = (1.08324 - j0.00006053)k_0 = 272.436 - j0.01522.$$

Then, from Eq. (2.161), the phase constant vector of the $(-1, 0)$ Floquet harmonic is at an angle

$$\phi = \tan^{-1} \left(\frac{\beta_{(0,0)}^{LW} \sin \phi_{00}}{\beta_{(0,0)}^{LW} \cos \phi_{00} - 2\pi/a} \right) = -74.57^\circ. \quad (4.13)$$

From Eq. (2.160), the magnitude of the phase constant vector of the $(-1, 0)$ Floquet harmonic is

$$|\underline{\beta}_{(-1,0)}^{LW}| = \sqrt{\left(\beta_{(0,0)}^{LW} \cos \phi_{00} - \frac{2\pi}{a} \right)^2 + \left(\beta_{(0,0)}^{LW} \sin \phi_{00} \right)^2} = 141.3111. \quad (4.14)$$

The wavenumber of the $(-1, 0)$ Floquet harmonic is therefore

$$k_{(-1,0)}^{LW} = 141.3111 - j0.01522 \cos(30^\circ + 74.57^\circ). \quad (4.15)$$

From Eq. (2.162), the angle of the grating lobe with the vertical axis due to the $(-1, 0)$ Floquet harmonic is

$$\theta_g = 0.5966 \text{ rad} = 34.18^\circ. \quad (4.16)$$

Method A works well here since the actual grating lobes are at roughly $\theta = 46^\circ$ and 34° .

The Method B CAD formula is also very successful in predicting the location of the

grating lobes as well, as can be seen from the radiation patterns for $\phi = -74.57^\circ$ shown in Fig. 4.15.

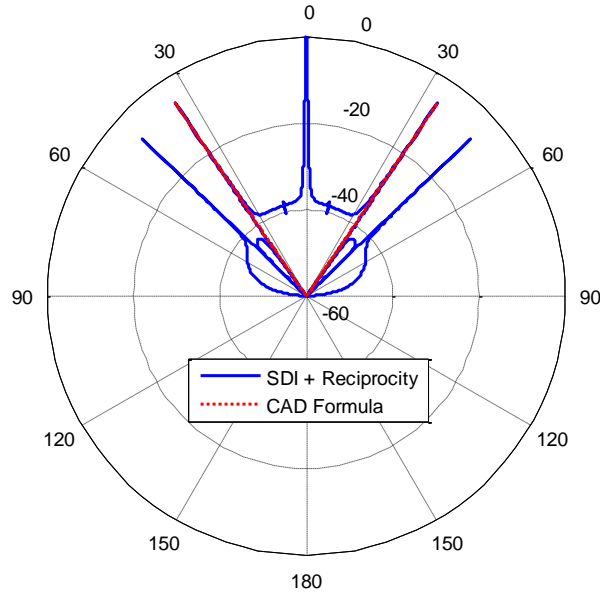


Fig. 4.15. Grating lobe predicted using the CAD formula for case 4.

It has been observed that there are up to three grating lobes in the radiation pattern of the 2D periodic leaky-wave antenna. The grating lobes are very narrow in θ (angle with the vertical axis) but much more spread-out in ϕ (azimuthal angle). The grating lobes are due to the $(-1, 0)$ and $(-1, -1)$ harmonics of the E-plane leaky mode and the $(0, -1)$ harmonic of the H-plane leaky mode, and these components each produce a grating lobe in the radiation pattern. Tables 4.1, 4.2, and 4.3 show the tracking of these components of the leaky mode using Method A to see what part of the structure produces the grating lobes. The angle of propagation of the fundamental harmonic of the leaky mode ϕ_{00} is gradually varied over a range in the tables below and the columns list the intermediate calculated values of the following: the wavenumber of the fundamental harmonic of the

leaky wave $k_{(0,0)}^{LW}$, the angle $\phi = \phi_{pq}$ at which the phase constant of the $(p, q)^{\text{th}}$ harmonic has its radiation directed, the magnitude of the phase constant of the $(p, q)^{\text{th}}$ harmonic $\beta_{(p,q)}^{LW}$, and the angle of the grating lobe with the vertical axis θ_g .

Table 4.1. Tracking the grating lobe due to the $(-1, 0)$ Floquet harmonic of the E-plane leaky mode (perturbed surface-wave mode).

ϕ_{00}	$k_{(0,0)}^{LW}$ (in m^{-1})	ϕ (i.e. ϕ_{pq}) (in degrees)	$\beta_{(-1,0)}^{LW}$ (in m^{-1})	θ_g predicted (in degrees)
5°	272.84625 - j0.019974	-85.8515	23.84259	5.43987
10°	272.68787 - j0.014068	-83.9871	47.61371	10.91298
15°	272.61756 - j0.012224	-81.7707	71.29270	16.46732
20°	272.56016 - j0.015464	-79.4213	94.83288	22.15212
25°	272.49924 - j0.015815	-77.0108	118.18727	28.02955
30°	272.43620 - j0.015224	-74.5705	141.31114	34.18523
35°	272.38935 - j0.015001	-72.1194	164.16557	40.74867
40°	272.25387 - j0.010652	-69.6311	186.67390	47.92241
45°	272.19028 - j0.014018	-67.1597	208.84286	56.13825
50°	272.11303 - j0.011664	-64.6803	230.60348	66.47806
55°	272.03659 - j0.007300	-62.1982	251.91940	Complex number. No grating lobe.
60°	272.03038 - j0.009039	-59.7267	272.78469	Complex number. No grating lobe.
65°	271.90439 - j0.004247	-57.2315	293.06640	Complex number. No grating lobe.

Table 4.2. Tracking the grating lobe due to the $(-1, -1)$ Floquet harmonic of the E-plane mode (perturbed surface-wave mode).

ϕ_{00}	$k_{(0,0)}^{LW}$ (in m^{-1})	ϕ (i.e. ϕ_{pq}) (in degrees)	$\beta_{(-1,-1)}^{LW}$ (in m^{-1})	θ_g predicted (in degrees)
5°	272.84625 – j0.019974	89.6754	304.46411	Complex number. No grating lobe.
10°	272.68787 – j0.014068	88.9827	280.93187	Complex number. No grating lobe.
15°	272.61756 – j0.012224	87.7322	257.88270	Complex number. No grating lobe.
20°	272.56016 – j0.015464	85.7633	235.66226	69.55725
25°	272.49924 – j0.015815	82.8935	214.72573	58.62472
30°	272.43620 – j0.015224	78.9221	195.66713	51.07747
35°	272.38935 – j0.015001	73.6671	179.23651	45.45225
40°	272.25387 – j0.010652	67.0226	166.44372	41.43732
45°	272.19028 – j0.014018	59.1598	158.13138	38.95792
50°	272.11303 – j0.011664	50.5354	155.16316	38.09356
55°	272.03659 – j0.0072997	41.8930	157.84544	38.87420
60°	272.03038 – j0.009039	33.9706	165.81881	41.24770
65°	271.90439 – j0.004247	27.2828	178.47564	45.20569
70°	271.84761 – j0.002790	21.9555	194.67431	50.71885
75°	271.80214 – j0.001609	17.9183	213.54284	58.11089
80°	271.76871 – j0.000713	14.9886	234.31256	68.69430
85°	271.74808 – j0.000089	12.9659	256.38522	Complex number. No grating lobe.
88.364°	271.74130 – j0.0000000004766	12.0241	271.73650	Complex number. No grating lobe.

Table 4.3. Tracking the grating lobe due to the (0, -1) Floquet harmonic of the H-plane mode.

ϕ_{00}	$k_{(0,0)}^{LW}$ (in m^{-1})	ϕ (i.e. ϕ_{pq}) (in degrees)	$\beta_{(0,-1)}^{LW}$ (in m^{-1})	θ_g predicted (in degrees)
88.5°	399.90317 - j0.050847	81.6736	72.28877	16.70409
85°	472.20717 - j0.033488	73.8553	148.00796	36.05046
80°	540.90273 - j0.019732	65.3249	224.98966	63.45531
75°	592.31881 - j0.006187	57.8482	288.07556	Complex number. No grating lobe.
70°	632.01157 - j0.001262	50.8653	342.48975	Complex number. No grating lobe.
66.1°	656.11189 - j0.000000	45.6178	380.04374	Complex number. No grating lobe.

We see from Tables 4.1, 4.2, and 4.3 that the E-plane mode and the H-plane mode produce the grating lobes. The third (somewhat mysterious) mode does not seem to be producing the grating lobes. There are usually up to three grating lobes in the region ($0 < \theta < 90^\circ$) which seem to be due to the (-1, 0) and (-1, -1) Floquet waves of the E-plane mode (perturbed surface-wave mode) and the (0, -1) Floquet harmonic of the H-plane mode. The main beam seems to be produced by a narrow sector of the structure along the x -axis and also the H-plane mode along the y -axis.

The grating lobes here should not be confused with grating lobes in antenna arrays. The grating lobes occurring in the 2D periodic leaky wave antenna are originating from

the $(-1, 0)$, $(0, -1)$ and $(-1, -1)$ Floquet modes, interacting with different sectors of the structure other than the narrow wedge regions along the x -axis and y -axis.

4.6 Radiation Efficiency of the 2D Periodic Leaky-Wave Antenna

The approximate radiation efficiency of the 2D periodic leaky wave antenna can be calculated as

$$e_r = \frac{\alpha_{rad}}{\alpha_{total}} = \frac{\alpha_{rad}}{\alpha_{rad} + \alpha_{loss}}, \quad (4.17)$$

where α_{rad} is the attenuation constant due to the radiation from the leaky wave and α_{loss} is the attenuation constant due to the material loss. The attenuation term α_{loss} is a sum of the dielectric loss (α_d) and the conductor loss (α_c). The conductor loss is a sum of the loss in the patches (α_p) and loss in the ground plane (α_g). This gives us the relation

$$\alpha_{loss} = \alpha_d + \alpha_p + \alpha_g. \quad (4.18)$$

The attenuation constant of the surface wave is equal to $(\alpha_d + \alpha_g)$ and here the ground is treated as lossy with the finite conductivity of copper. The attenuation constant due to radiation (α_{rad}) is calculated by making the dielectric and conductor completely lossless and calculating the attenuation constant of the leaky wave. The total attenuation constant α_{total} ($= \alpha_{rad} + \alpha_{loss}$) is the attenuation constant of the leaky wave. Therefore, α_{rad} can also be calculated as

$$\alpha_{rad} = \alpha_{total} - \alpha_{loss}. \quad (4.19)$$

The loss in the patches α_p can be calculated by modifying the determinant equation for calculating the leaky wave wavenumber in Eq. (2.148), to account for the loss due to the patches. In order to do this we go back to the EFIE (electric field integral equation) as implemented in Section 2.3 of Chapter 2. Here we assume that there are no magnetic dipole sources but only a surface current on the surface of the dielectric to represent the patch currents, given by the surface current density

$$J_{sx}(x, y) = \sum_{l=1}^{N_b} a_l f_l(x) g(y) = \sum_{l=1}^{N_b} a_l B_l(x, y), \quad (4.20)$$

where

$$f_l(x) = \sin\left[\frac{l\pi}{L}\left(x + \frac{L}{2}\right)\right], \quad g(y) = \frac{1/\pi}{\sqrt{(W/2)^2 - y^2}}. \quad (4.21)$$

The EFIE is then enforced over the patch (0, 0) as

$$E_x^{sca} = Z_s J_{sx}, \quad (4.22)$$

where Z_s is the surface impedance of copper with conductivity $\sigma = 3 \times 10^7$ S/m. The above equality is enforced in the average sense by multiplying by a testing function and integrating over the area of the patch. The testing function on the left hand side is taken to be the same as the basis function. On the right hand side, doing the same would result in an integral that is too singular to be integrated. Therefore, on the right hand side we pick a testing function that has no variation along the y -direction and has the same y integral (i.e., the same current on the patch), given by

$$T_r(x, y) = f_r(x) \left(\frac{1}{W}\right) = \left(\frac{1}{W}\right) \sin\left[\frac{l'\pi}{L}\left(x + \frac{L}{2}\right)\right]. \quad (4.23)$$

Therefore, by testing Eq. (4.22) in this way we obtain

$$\int_{-W/2-L/2}^{W/2} \int_{-L/2}^{L/2} E_x^{sca} B_r(x, y) dx dy = \int_{-W/2-L/2}^{W/2} \int_{-L/2}^{L/2} Z_s J_{sx} T_r(x, y) dx dy. \quad (4.24)$$

Similar to the derivation leading up to Eq. (2.89), the scattered field E_x^{sca} due to the surface current J_{sx} is

$$E_x^{sca} = \frac{1}{ab} \sum_{p=-\infty}^{\infty} \sum_{q=-\infty}^{\infty} \tilde{G}_{xx}^{EJ}(k_{xp}, k_{yq}) \tilde{J}_{sx}(k_{xp}, k_{yq}) e^{-j(k_{xp}x + k_{yq}y)}. \quad (4.25)$$

Substituting from Eqs. (4.20) and (4.25) in Eq. (4.24) and integrating, we obtain

$$\frac{1}{ab} \sum_{l=1}^{N_b} a_l \sum_{p=-\infty}^{\infty} \sum_{q=-\infty}^{\infty} \tilde{G}_{xx}^{EJ}(k_{xp}, k_{yq}) \tilde{B}_l(k_{xp}, k_{yq}) \tilde{B}_l(-k_{xp}, -k_{yq}) = \sum_{l=1}^{N_b} a_l Z_s \left(\frac{L}{2}\right) \delta_{l'l} \left(\frac{1}{W}\right). \quad (4.26)$$

This gives us the matrix equation

$$[Z_{l'l}] - Z_s \left(\frac{L}{2W}\right) [U] = 0. \quad (4.27)$$

Here, $[U]$ is the identity matrix, L is the length of the patches, W is the width of the patches, and $[Z_{l'l}]$ is the Z Matrix defined in Eqs. (2.134) and (2.135). The determinant of the left hand side in Eq. (4.27) is equated to zero and we then have

$$\text{Det} \left([Z_{l'l}] - Z_s \left(\frac{L}{2W}\right) [U] \right) = 0. \quad (4.28)$$

Solving this equation gives us the complex wavenumber of the leaky wave supported by the 2D periodic LWA structure that has patches with finite conductivity.

The attenuation constant of the leaky wave obtained by solving Eq. (4.28) while assuming the ground plane to have finite conductivity is α_{total} . The attenuation constant

of the leaky-wave wavenumber obtained by solving Eq. (2.148) while assuming the ground plane to have finite conductivity gives $\alpha_{total} - \alpha_p$ since Eq. (2.148) assumes lossless PEC patches. The attenuation constant due to leaky-wave radiation (α_{rad}) was calculated by solving Eq. (2.148) while assuming a lossless ground and lossless substrate.

In this section we take the following design parameters for the 2D periodic leaky-wave antenna: the frequency is $f = 12$ GHz, the substrate is chosen to have a relative permittivity of $\epsilon_r = 9.8$, the substrate is lossy with a loss tangent $\tan\delta = 0.002$, and the height of the substrate is $h = 1.27$ mm. The substrate is a grounded dielectric with the excitation provided by a narrow y -directed slot in the ground plane. The slot is centered at the location $(x_0 = a/2, y_0 = 0)$. The length of each patch L is varied, the width is $W = L/5$, and the design has been optimized for maximum power density radiated at broadside by adjusting the length of the unit cell a while keeping the width $b = a/1.2$. The attenuation constant of the surface wave with lossy, copper ground plane is $0.00030942k_0$, where k_0 is the wavenumber in free space.

Table 4.4 gives the radiation efficiency for three different cases with different lengths of patches. Table 4.4 also lists the optimum length of the unit cell a for maximum power density at broadside, the attenuation constant of the E-plane leaky mode with and without considering the loss from the patches, and the attenuation constant due to the radiation from the E-plane leaky mode. From Table 4.4 we see that the radiation efficiency increases as the length of the patches is increased.

Table 4.4. Radiation efficiency vs. length of patches.

Length of the patches, L (in cm)	Optimized length of the unit cell, a (in cm)	Attenuation constant of the E-plane leaky mode with patch loss α_{total}	Attenuation constant of the E-plane leaky mode without patch loss $\alpha_{total} - \alpha_p$	Attenuation constant due to leaky-wave radiation α_{rad}	Radiation efficiency
0.25	2.2968	$0.0014148k_0$	$0.0013600k_0$	$0.00057653k_0$	40.750 %
0.30	2.2725	$0.0037817k_0$	$0.0035224k_0$	$0.0025556k_0$	67.578 %
0.35	2.1204	$0.038145k_0$	$0.035159k_0$	$0.034023k_0$	89.194 %

CHAPTER 5 PLASMONIC STRUCTURE – DIRECTIVE BEAMING AT OPTICAL FREQUENCIES

The phenomena of directive beaming is observed at optical frequencies in a plasmonic structure that consists of a thin silver (or similar plasmonic material) film with a subwavelength aperture surrounded by periodic corrugations. Silver is a plasmonic material and behaves like a lossy dielectric with a negative permittivity at optical frequencies. Usually the transmission of light through a subwavelength aperture in a silver film without corrugations produces a broad radiation pattern as the aperture radiates. But when periodic corrugations are present and optimized, directive beaming occurs where the beam emerges on the other side of the aperture as a very focused narrow beam of light. Figure 5.1 shows the silver film with periodic corrugations on its upper surface and a subwavelength hole in the center through which the incident energy is coupled into the surface plasmon wave.

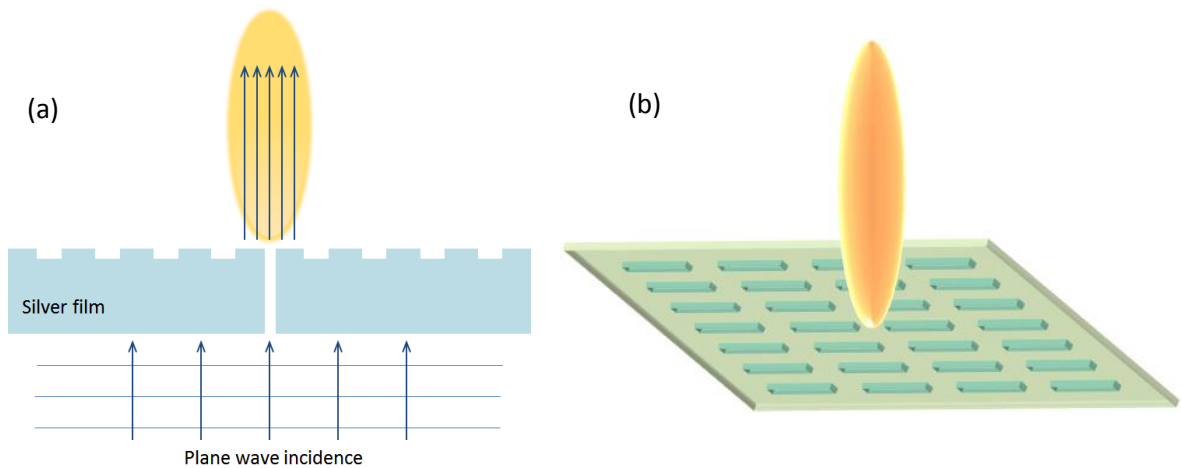


Fig. 5.1. Directive beaming in a silver film with corrugations around a subwavelength aperture. (a) Cross-section view, (b) 3D view of the plasmonic structure.

This structure has the same operating principle as a 2D periodic leaky-wave antenna at microwave frequencies. The silver film supports a surface plasmon wave that is similar to a TM surface wave in a grounded dielectric substrate at microwave frequencies. Due to the presence of corrugations, the surface plasmon waves get perturbed into leaky plasmon waves which radiate producing the narrow beam.

In the plasmonic structure, for the purpose of analysis, the corrugations on the surface of the silver film can be modeled as conducting patches and the subwavelength aperture can be modeled as a magnetic dipole at the upper surface of the silver film, as shown below in Fig. 5.2. In this case there is no ground plane and the media above and below the silver layer is air.

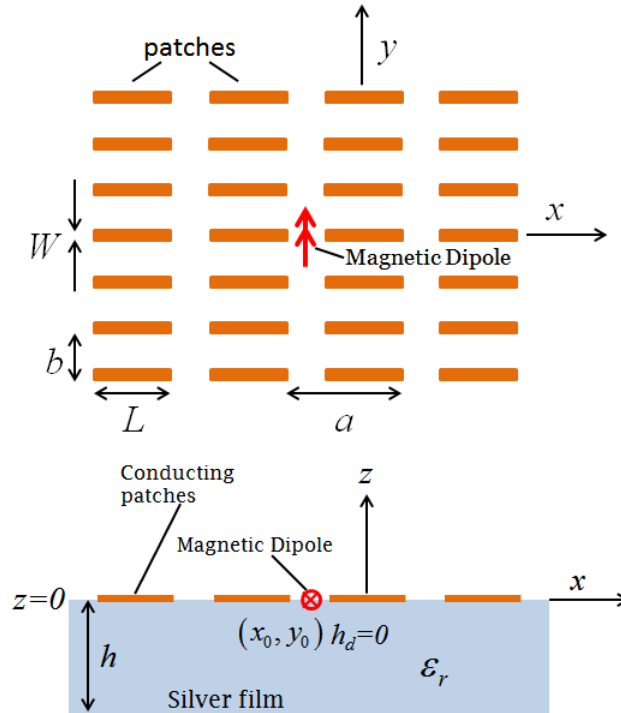


Fig. 5.2. Top view and cross-sectional view of the silver film, with the grooves modeled as perfectly conducting patches and the aperture modeled as a magnetic dipole.

As shown in Fig. 5.2, the grooves (modeled here as perfectly conducting patches) are arranged on the surface of the silver film in a rectangular lattice. The dimensions of the patches are L for the length and W for the width, and the dimensions of the unit cell are a in the x -direction and b in the y -direction. The height or thickness of the silver film is h , the relative permittivity of silver is $\epsilon_r = -4.5$, and the loss tangent is $\tan \delta = 0.04545$. The subwavelength aperture that is modeled as the magnetic dipole source is located at $z = -h_d$, $x = -a/2$ and $y = 0$. For the plasmonic structure $h_d = 0$. Similar to the microwave case, the plasmonic structure is optimized by adjusting the period a .

5.1 Radiation Patterns and Radiation Properties

The radiation patterns are obtained from reciprocity, applied along with the spectral domain immittance method as discussed in detail in Section 2.2 of Chapter 2. For the optical plasmonic structure the frequency is taken to be $f = 750$ THz. The substrate here is silver, which has a relative permittivity of $\epsilon_r = -4.5$ and a loss tangent of $\tan \delta = 0.04545$, and the height of the substrate is $h = 300$ nm. The substrate is a slab of lossy dielectric (silver), with the excitation provided by a subwavelength aperture through the dielectric slab. The aperture is centered at the location, $x_0 = a/2$, $y_0 = 0$. The subwavelength aperture in the silver layer is modeled as an infinitesimal y -directed magnetic dipole at the upper surface of the silver layer. Figure 5.3 shows a contour plot of the power radiated (in dB) in the far field at broadside for a range of values of a and b . This plot is similar to what we have seen in the microwave case (in Fig. 3.2). The band of red is the region of highest power radiated and the plot shows that this region is like a ridge that

runs across the whole range of values for b ; there is no clear maxima seen on this color scale.

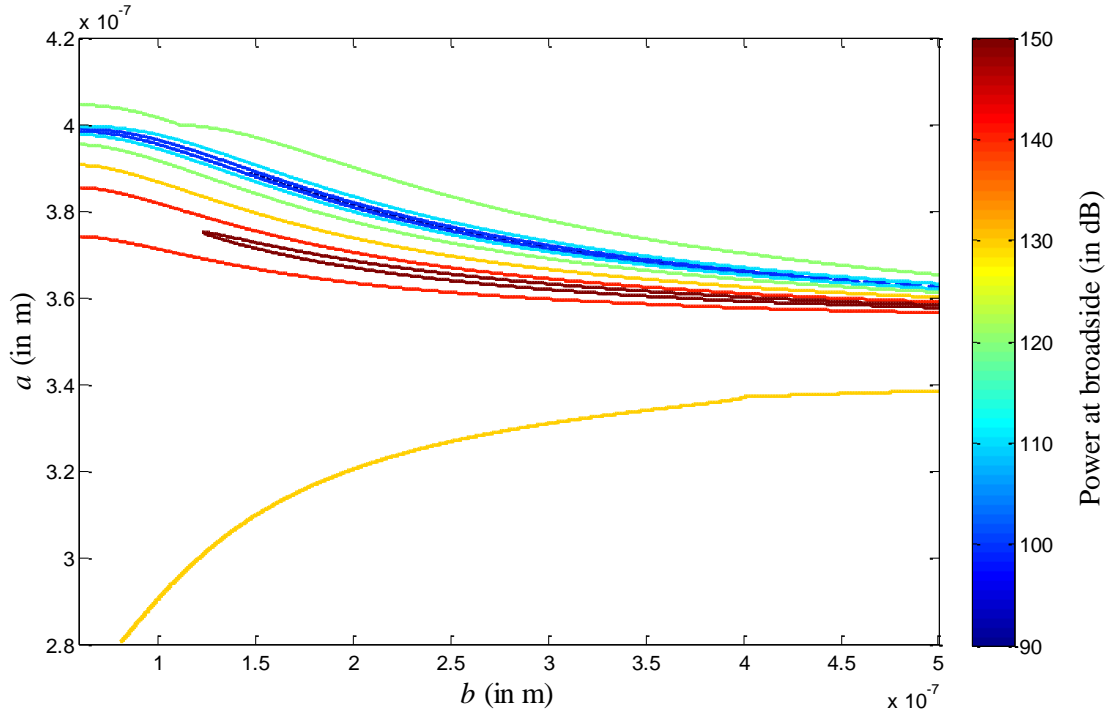


Fig. 5.3. Contour plot of the power radiated at broadside for different values of a and b .

Some of the typical radiation patterns for the plasmonic case are given next. In the following case, shown in Fig. 5.4, the length of the patches is $L = 140$ nm, the width is $W = 50$ nm, and the dimension of the unit cell in the y -direction is $b = 90$ nm. The number of basis functions assumed for modeling the currents on the patches (given in Eq. (2.18)) is five. Here the design is optimized by keeping all other parameters fixed and varying the spacing a between the unit cells in the x -direction to get maximum power density radiated at broadside. Based on this, the dimension of the unit cell in the x -direction is given by $a = 380.114$ nm.

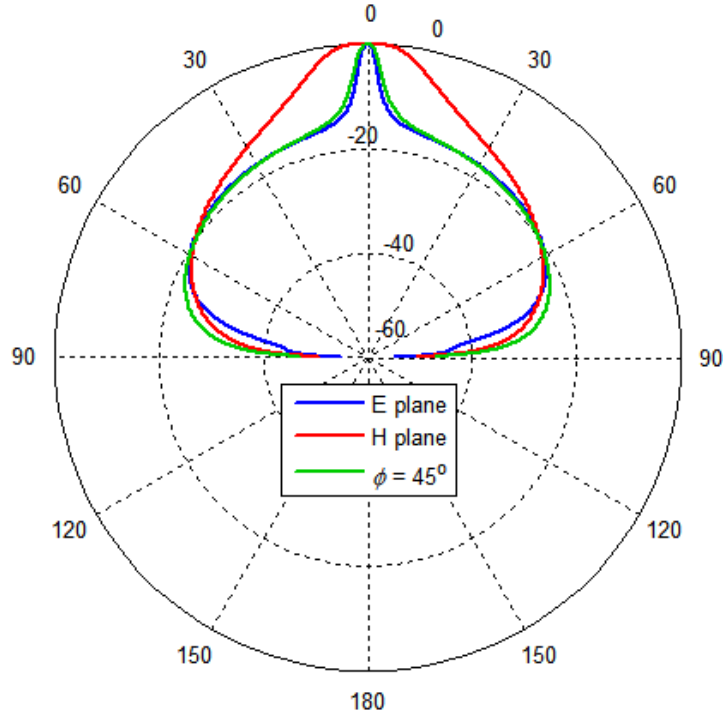


Fig. 5.4. Radiation patterns for different angles ϕ , calculated with 5 basis functions.

In the following case, shown in Fig. 5.5, all of the physical parameters are kept the same as before. The length of the patches is $L = 140$ nm, the width is $W = 50$ nm, and the dimension of the unit cell in the y -direction is $b = 90$ nm. The number of basis functions assumed for modeling the currents on the patches (given in Eq. (2.18)) is now taken to be one. Once again the design is optimized by keeping all other parameters fixed and varying the spacing a between the unit cells in the x -direction to get maximum power density radiated at broadside. Based on this, the dimension of the unit cell in the x -direction is given by $a = 378.824$ nm.

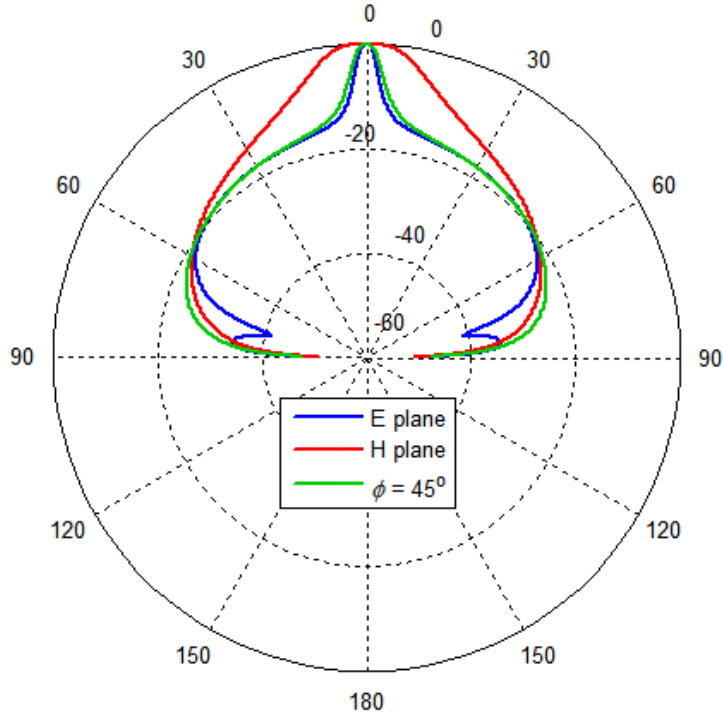


Fig. 5.5. Radiation patterns for different angles ϕ , calculated with 1 basis function.

Comparing Figs. 5.4 and Fig. 5.5, the radiation pattern calculated using five basis functions is slightly different from that obtained using one basis function. Using five basis functions is slightly more accurate than using one basis function, but it requires much more time to compute the results. Therefore in all other calculations done here, only one basis function has been used.

The dependence of the beamwidths of the radiation pattern in the E-plane and the H-plane and the enhancement factor (EF) on the dimensions of the patches of the plasmonic structure is examined in Fig. 5.6. The parameters of the plasmonic structure are as follows. The frequency is $f = 750$ THz, the substrate is silver, which has a relative permittivity of $\epsilon_r = -4.5$ and a loss tangent of $\tan\delta = 0.04545$, and the height of the substrate is $h = 300$ nm. The excitation is provided by a subwavelength aperture through

the dielectric slab. The aperture is centered at the location, $x_0 = a/2$, $y_0 = 0$. The subwavelength aperture in the silver layer is modeled as an infinitesimal y -directed magnetic dipole at the upper surface of the silver layer. The length of the patches L is varied while the width is chosen as $W = L/2.8$. For each different length of patch L , the length of the unit cell a is adjusted for maximum power density at broadside while maintaining the width of unit cell as $b = a/4$. The variation of the beamwidths and enhancement factor with respect to the length of the patches is given in Fig. 5.6.

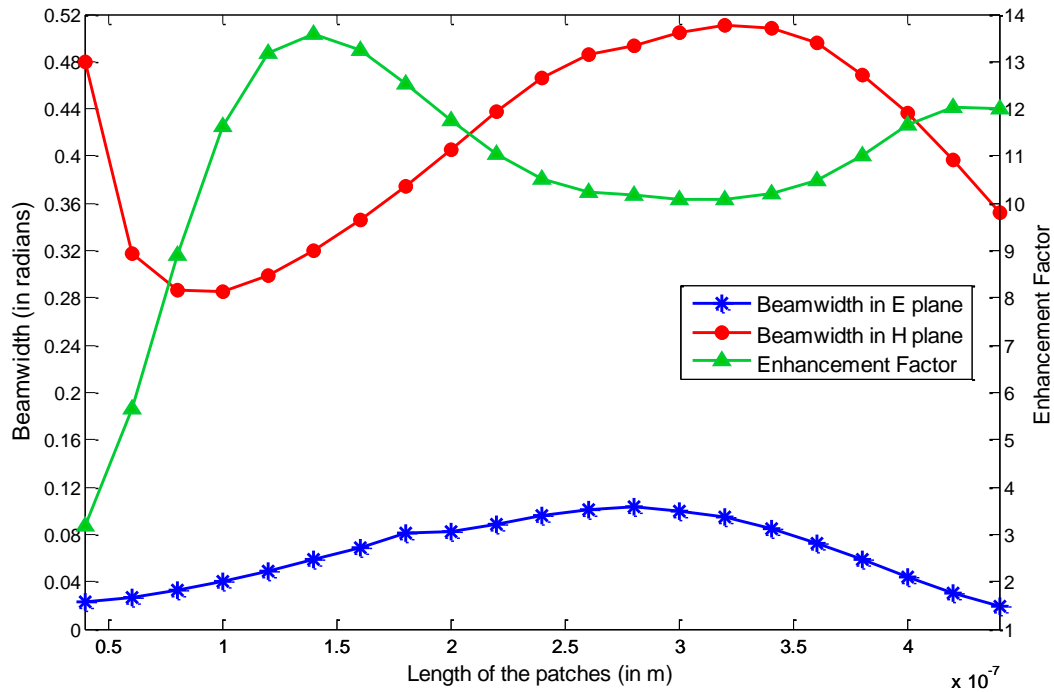


Fig. 5.6. Beamwidths and enhancement factor vs. the length of the patches.

From Fig. 5.6 we see that as the length of the patches is made very small, the beamwidths decrease but so does the enhancement factor. If the beamwidths decrease then the enhancement factor is normally expected to increase, but in this case it decreases because the space wave field increases relative to the leaky-wave field to a great extent as

the patches are made very small. As the patches get larger, the beamwidths increase and then decrease whereas the enhancement factor shows an opposite trend as the beamwidth – it increases when the beamwidth decreases. This is very similar to the behavior seen at microwave frequencies, as shown in Fig. 3.28.

5.2 CAD Formula to Calculate the Radiation Pattern of the Leaky-Wave Beam

In this section the CAD formula for calculating the radiation pattern due to the leaky wave, discussed in Section 2.6 of Chapter 2, is compared to the radiation pattern obtained from reciprocity and the spectral domain immittance method (SDI) as discussed in Section 2.2 of Chapter 2. The reciprocity technique along with the SDI method gives the total radiation pattern, which is a superposition of the radiation due to the leaky wave as well as the space wave radiated directly by the magnetic dipole source.

The frequency here is taken to be $f = 750$ THz. The substrate is silver which has a relative permittivity of $\epsilon_r = -4.5$ and a loss tangent of $\tan\delta = 0.04545$, and the height of the substrate is $h = 300$ nm. The substrate is a layer of lossy dielectric (silver) with the excitation provided by a subwavelength aperture through the dielectric layer. The aperture is centered at the location, $x_0 = a/2$, $y_0 = 0$. The subwavelength aperture in the silver layer is modeled as an infinitesimal y -directed magnetic dipole at the upper surface of the silver layer. In the following case shown in Figs. 5.7 and 5.8, the length of the patch is $L = 140$ nm, the width is $W = 50$ nm, and the dimension of the unit cell in the y -direction is $b = 90$ nm. The number of basis functions assumed for modeling the currents on the patches (given in Eq. (2.18)) is one. Here the design is optimized by keeping all other parameters fixed and varying the spacing a between unit cells in the x -direction to

get maximum power density radiated at broadside. Based on this, the dimension of the unit cell in the x -direction is $a = 378.824$ nm. Figure 5.7 shows the comparison of the CAD formula and the reciprocity method using the spectral domain immittance method (which gives a numerically exact pattern) for the E-plane ($\phi = 0^\circ$), and the Fig. 5.8 shows the same comparison for the H-plane ($\phi = 90^\circ$). The leaky mode wavenumbers in the E-plane and the H-plane are $k_\rho^{LW} = 2.79 \times 10^5 - j3.58 \times 10^5 = (0.0177 - j0.0228)k_0$ for the $(-1,0)$ Floquet harmonic and $k_\rho^{LW} = 1.515 \times 10^6 - j1.78 \times 10^6 = (0.0964 - j0.113)k_0$ for the $(0,-1)$ Floquet harmonic respectively, where k_0 is the wavenumber of free space for the same frequency (750 THz).

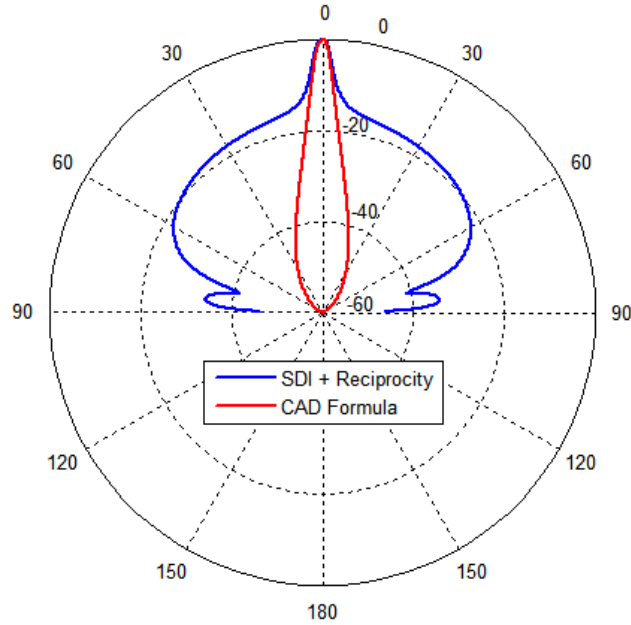


Fig. 5.7. Pattern of the leaky-wave beam compared to the pattern from reciprocity in the E-plane for a lossy silver substrate.

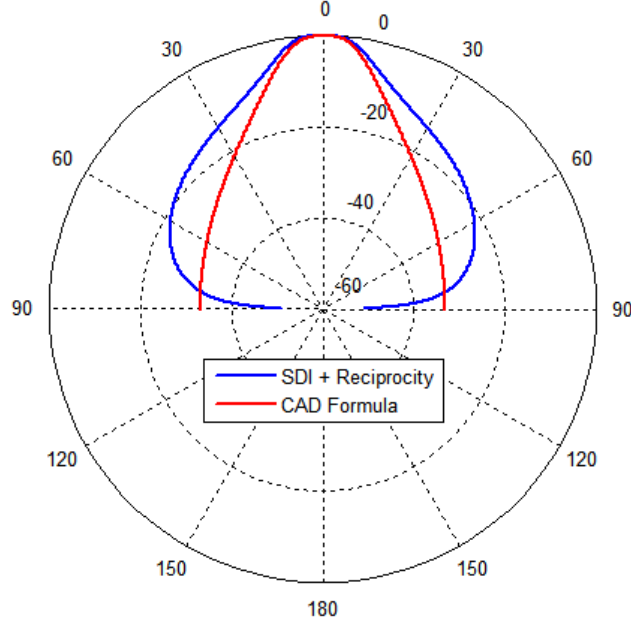


Fig. 5.8. Pattern of the leaky-wave beam compared to the pattern from reciprocity in the H-plane for a lossy silver substrate.

Similarly, Fig. 5.9 and Fig. 5.10 show the comparison of the CAD formula and the reciprocity method using the spectral domain immittance method for the E-plane ($\phi = 0^\circ$), and the H-plane ($\phi = 90^\circ$) respectively, for the case of lossless silver (relative permittivity of $\epsilon_r = -4.5$ and a loss tangent of $\tan\delta = 0$). The dimension of the unit cell in the x -direction a is optimized for maximum power density at broadside, and therefore $a = 378.959$ nm. The leaky mode wavenumbers in the E-plane and the H-plane are $k_\rho^{LW} = 2.44 \times 10^5 - j2.67 \times 10^5 = (0.0155 - j0.0170)k_0$ for the $(-1,0)$ Floquet harmonic and $k_\rho^{LW} = 1.25 \times 10^6 - j1.377 \times 10^6 = (0.0795 - j0.0876)k_0$ for the $(0,-1)$ Floquet harmonic respectively, where k_0 is the wavenumber of free space for the same frequency (750 THz).

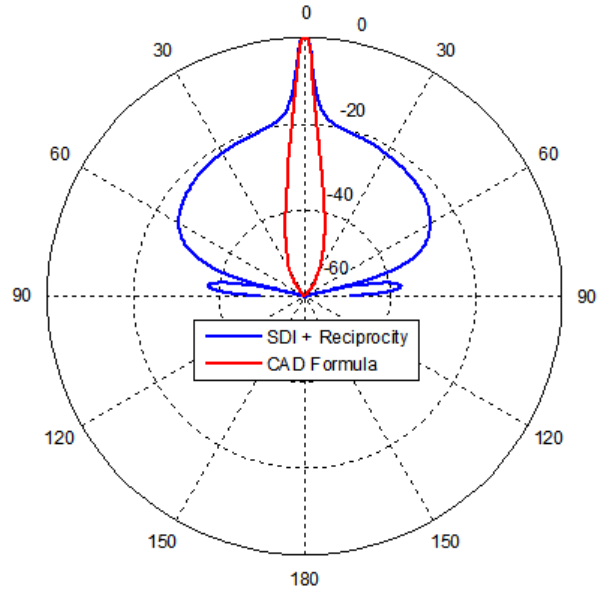


Fig. 5.9. Pattern of the leaky-wave beam compared to the pattern from reciprocity in the E-plane for a lossless silver substrate.

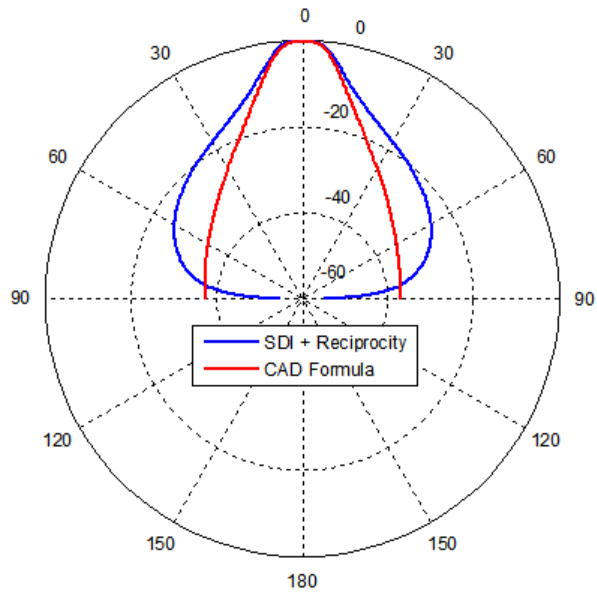


Fig. 5.10. Pattern of the leaky-wave beam compared to the pattern from reciprocity in the H-plane for a lossless silver substrate.

The CAD formula when applied to the E-plane works quite well to predict the shape of the leaky-wave beam, as seen in Fig. 5.7 and Fig. 5.9. For the H-plane shown in Fig. 5.8 and Fig. 5.10, the leaky-wave beam from reciprocity is less clearly defined due to the

large amount of space wave, though the agreement is still fairly good near the peak of the beam.

5.3 Current Distribution on the Patches from the Array Scanning Method

The current at the center of the patches, which models the grooves in the plasmonic directive beaming structure, is calculated using the array scanning method (ASM) discussed in Section 2.3 of Chapter 2 and is plotted in Figs. 5.11 and 5.12 for the E-plane (along the x -axis) and H-plane (along the y -axis), respectively. The magnitude of the current distribution on the patches, given by the red curve in Figs. 5.11 and 5.12, is normalized. The blue curve gives the asymptotic distribution of the leaky wave based on the exponential decay of the leaky mode and an appropriate algebraic decay that is also added. For the E-plane the leaky mode field distribution over the surface of the dielectric is $e^{-\alpha_E x} / x^{1/2}$ and for the H-plane it is $e^{-\alpha_H y} / y^{3/2}$, where α_E and α_H are the attenuation constants of the leaky mode in the E-plane (along the x -axis) and H-plane (along the y -axis), respectively. Along the surface of the dielectric, the leaky mode interferes with the space wave, and therefore the current distribution on the patches is not smooth and displays an interference pattern. In the absence of interference with the space wave, the current distribution from ASM (the red curve) would closely match the blue curve in Figs. 5.11 and 5.12.

In this case the design parameters of the plasmonic structure are as follows: The frequency is $f = 750$ THz. The substrate is silver which has a relative permittivity of $\epsilon_r = -4.5$ and a loss tangent of $\tan\delta = 0.04545$, and the height of the substrate is $h = 300$ nm. The substrate is a layer of lossy dielectric (silver) with the excitation provided by a

subwavelength aperture through the dielectric layer. The aperture is centered at the location, $x_0 = a/2$, $y_0 = 0$. The subwavelength aperture in the silver layer is modeled as an infinitesimal y -directed magnetic dipole at the upper surface of the silver layer. The length of the patches is $L = 140$ nm, the width is $W = 50$ nm, and the dimension of the unit cell in the y -direction is $b = 90$ nm. The number of basis functions assumed for modeling the currents on the patches (given in Eq. (2.83)) is one. Here the design is optimized by keeping all other parameters fixed and varying the spacing a between unit cells in the x -direction to get maximum power density radiated at broadside. Based on this, the dimension of the unit cell in the x -direction is $a = 378.824$ nm. The values of the attenuation constants are $\alpha_E = 3.58 \times 10^5 = 0.0228k_0$ and $\alpha_H = 1.78 \times 10^6 = 0.113k_0$, where k_0 is the wavenumber of free space for the frequency of 750 THz.

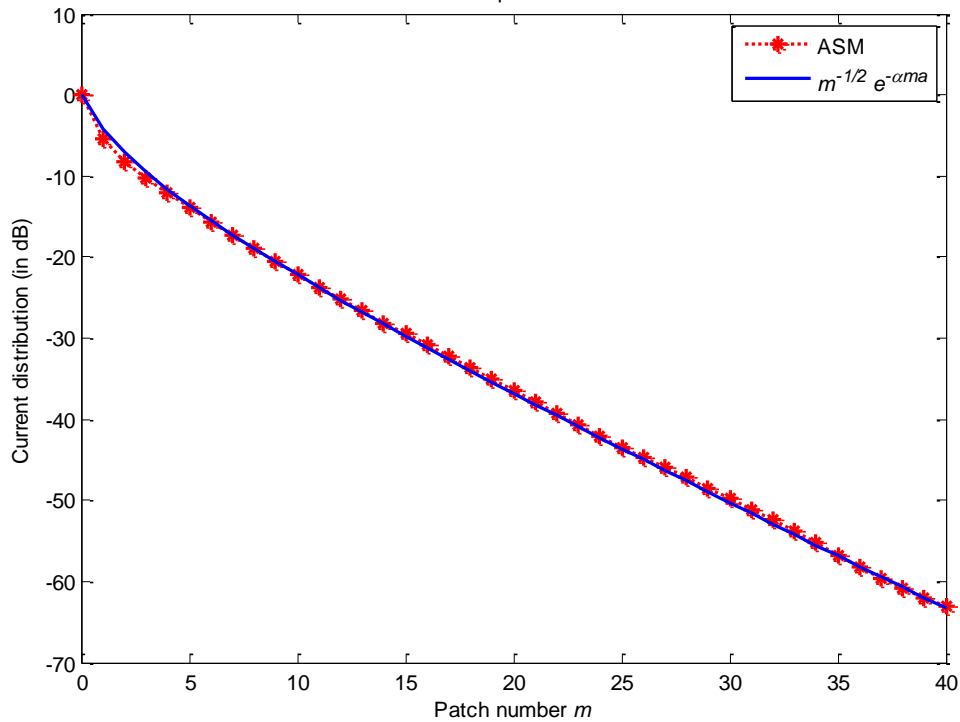


Fig. 5.11. Current distribution on the patches in the E-plane from ASM.

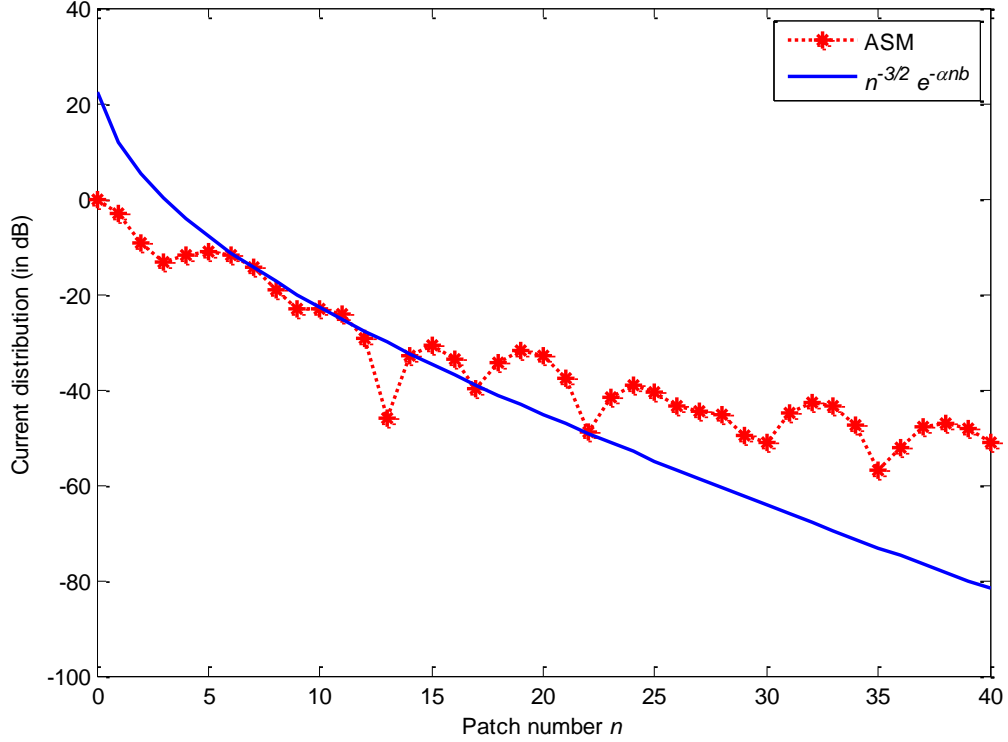


Fig. 5.12. Current distribution on the patches in the H-plane from ASM.

5.4 Dispersion Behaviour – Variation of Leaky Plasmon Wavenumber as a Function of the Azimuthal Angle ϕ

The wavenumber of the leaky plasmon wave, which produces the narrow directive beam in the plasmonic structure, varies with the radial angle of propagation ϕ . We take the following design parameters for the plasmonic directive beaming structure: The frequency is $f = 750$ THz. The substrate is silver, which has a relative permittivity of $\epsilon_r = -4.5$ and a loss tangent of $\tan\delta = 0.04545$, and the height of the substrate is $h = 300$ nm. The substrate is a layer of lossy dielectric (silver) with the excitation provided by a subwavelength aperture through the dielectric layer. The aperture is centered at the location, $x_0 = a/2$, $y_0 = 0$. The subwavelength aperture in the silver layer is modeled as an infinitesimal y -directed magnetic dipole at the upper surface of the silver layer. The

length of the patch is $L = 140$ nm, the width is $W = 50$ nm, and the dimension of the unit cell in the y -direction is $b = 90$ nm. The number of basis functions assumed for modeling the currents on the patches (given in Eq. (2.18)) is one. Here the design is optimized by keeping all other parameters fixed and varying the spacing a between patches in the x -direction to get maximum power density radiated at broadside. Based on this, the dimension of the unit cell in the x -direction is $a = 378.824$ nm. The normalized phase constant of the fundamental harmonic of the leaky plasmon wave is plotted in Fig. 5.13 with respect to the angle ϕ . Similarly, the normalized attenuation constant of the fundamental harmonic of the leaky plasmon wave is plotted in Fig. 5.14 with respect to the angle ϕ .

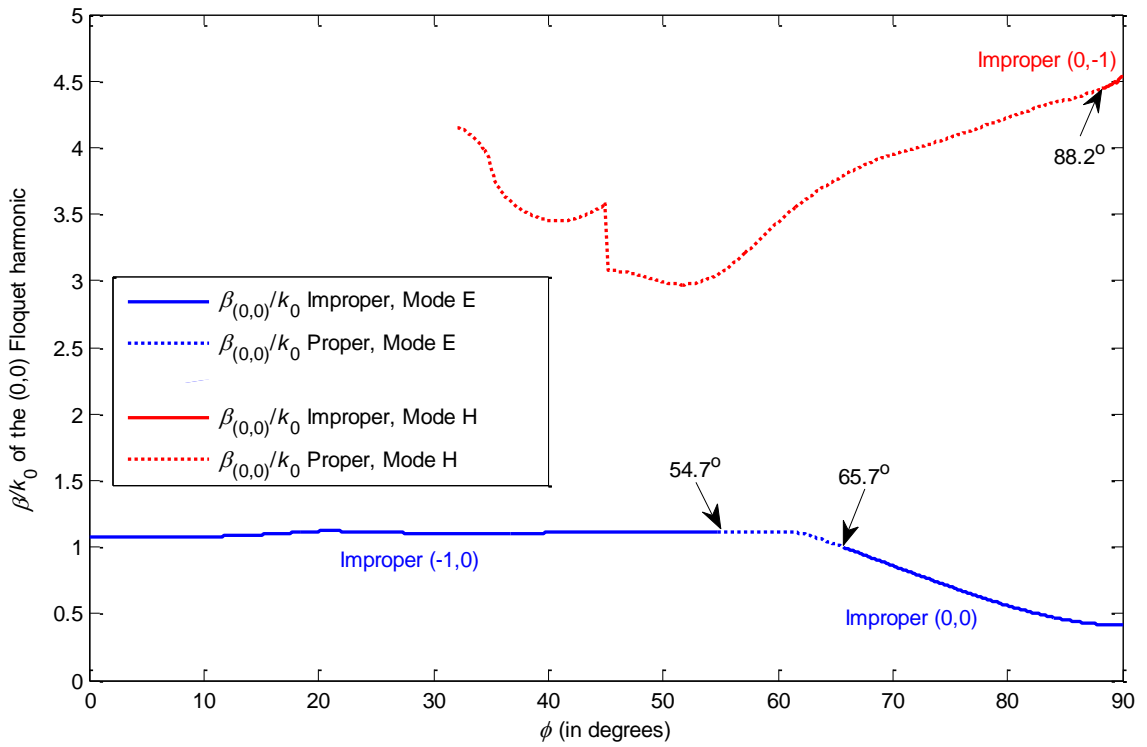


Fig. 5.13. Dispersion diagram showing the variation of the phase constant with ϕ .

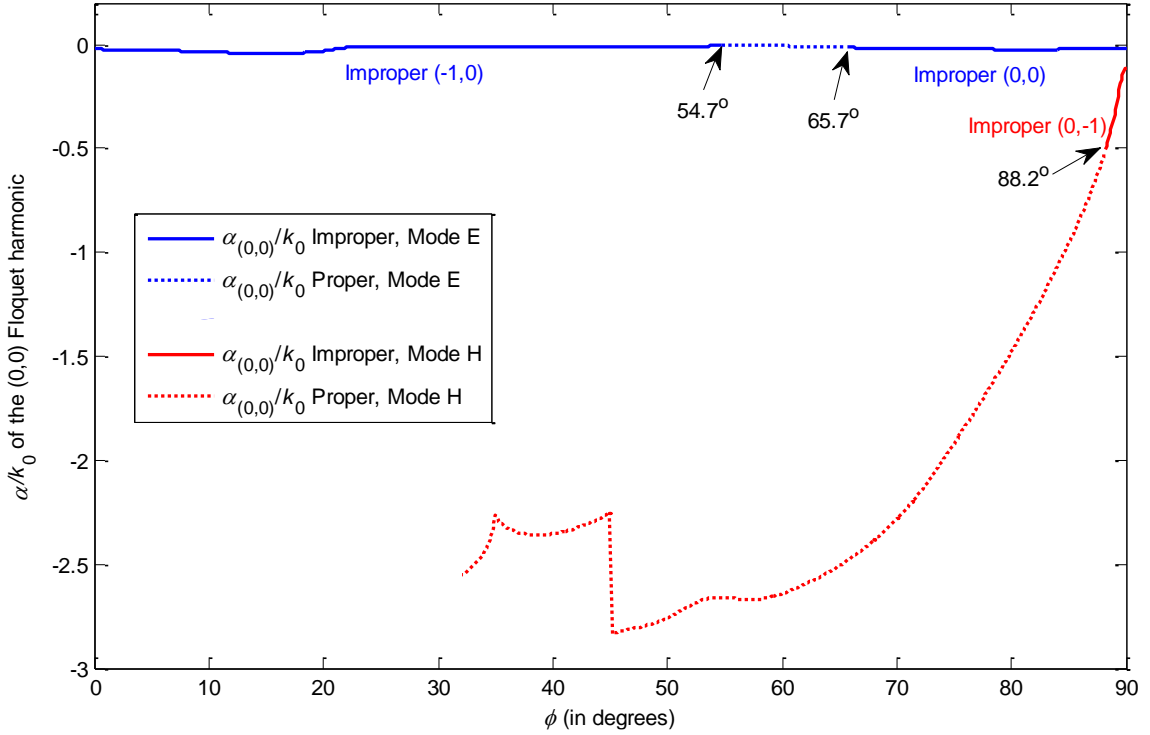


Fig. 5.14. Dispersion diagram showing the variation of the attenuation constant with ϕ .

From Figs. 5.13 and 5.14, we see that there are two separate leaky modes. The one that is dominant along the x -axis, i.e., in the E-plane, is shown in blue and is termed the E-plane mode (Mode E). The one that is dominant along the y -axis, i.e., in the H-plane, is shown in red and is termed the H-plane mode (Mode H). The E-plane leaky mode produces the beam in the E-plane and the H-plane leaky mode produces the beam in the H-plane.

So far it has been observed that the behavior of the plasmonic directive beaming structure is very similar to the 2D periodic leaky-wave antenna at microwave frequencies. The plasmonic structure and the 2D periodic leaky-wave antenna can be seen as equivalent structures after a geometric scaling with frequency and some variation due to the different substrate properties. Therefore, it is expected that many of the other results

and observations that were observed for the 2D periodic leaky-wave antenna would be approximately duplicated for the plasmonic structure.

CHAPTER 6 SUMMARY AND CONCLUSIONS

6.1 Summary

A 2D periodic leaky-wave antenna at microwave frequencies and a similar plasmonic structure at optical frequencies have been studied here. The radiation characteristics and the dependence of these characteristics on antenna parameters have been examined. Also, a fundamental explanation for the radiation behavior of this class of antenna – a 2D periodic leaky-wave antenna, has been explored.

The phenomena of directive beaming, which is observed in the plasmonic structure at optical frequencies, is the motivation behind this research into the 2D periodic leaky-wave antenna. The basic principle of operation of the 2D periodic leaky-wave antenna and the directive-beaming plasmonic structure is the same, and the narrow beam in each structure is produced by a radially-propagating radiating leaky wave supported by the structure.

The theoretical methods of analysis used for studying this antenna structure are: (1) reciprocity based on the spectral domain immittance method and the method of moments, (2) the array scanning method, and (3) an approximate CAD formula for calculating the radiation pattern due to a leaky wave. With these mathematical tools the radiation characteristics and the fundamental principle of operation of the leaky wave have been studied. This research has been conducted to study the nature of the radiating leaky wave and its correlation with the formation of the narrow main beam, grating lobes, an optimization of the pattern to get maximum power radiated at broadside, and the current distribution on the surface of the patches. The dispersion behavior of the different leaky

wave modes that exist on the structure has been examined to see how the wavenumber of the leaky mode varies with the azimuthal angle of propagation on the 2D periodic leaky-wave antenna structure. Some of the practical characteristics of the 2D periodic leaky-wave antenna such as radiation efficiency, bandwidth, figure of merit and normalized tolerance have been calculated.

Since the plasmonic structure at optical frequencies has similar radiation characteristics and principle of operation as the 2D periodic leaky-wave antenna, the same theoretical methods of analysis are used to study the plasmonic structure, namely: (1) reciprocity based on the spectral domain immittance method and the method of moments, (2) the array scanning method, and (3) an approximate CAD formula for calculating the radiation pattern due to the leaky wave. These theoretical methods are applied to the plasmonic structure to study the radiation characteristics and the fundamental principle of operation of the leaky mode, which have been found to be very similar to the 2D periodic leaky-wave antenna at microwave frequencies. The aspects of the plasmonic structure examined were the nature of the radiating leaky plasmon wave, the formation of the narrow main beam, an optimization of the pattern to get maximum power radiated at broadside, and the current distribution on the surface of the patches. The dispersion behavior of the different leaky wave modes was also examined to see how the wavenumber of the leaky mode varies with the azimuthal angle of propagation on the plasmonic structure.

6.2 Conclusions

From the radiation properties observed in Chapter 3 we see that the 2D periodic leaky-wave antenna can be optimized for maximum power density at broadside by adjusting the periodic spacing between the patches in the x -direction, i.e., the dimension a . When the periodic spacing between the patches in the y -direction, i.e., the dimension b is increased, the power density at broadside increases but so does the number of grating lobes. Hence, in order to keep the grating lobes at a minimum, b should be small. The power level of the grating lobes seem to decrease a little bit when a small amount of loss is added to the substrate. We have also observed that with a small variation in frequency the main beam, which is optimized for maximum power radiation at broadside, is split in the E-plane. In the H-plane it splits to a greater extent when the frequency is increased, but this splitting effect disappears and the beam diminishes when the frequency is lowered from its optimum value.

It is established that the CAD formula for the calculation of the leaky-wave radiation pattern for a 1D leaky-wave antenna works quite well in predicting the shape of the main beam in the E-plane and H-plane of the 2D periodic leaky-wave antenna. We also see that an effective 2D periodic leaky-wave antenna can be designed for a variety of substrate material, even one with relative permittivity as low as $\epsilon_r = 2.2$, as well as one with a higher loss tangent such as $\tan\delta = 0.004$. The cross-section of the main beam reveals that the beam is usually much narrower in the E-plane and much wider in the H-plane. For a lossless substrate, the beamwidths in the E-plane and H-plane decrease and the enhancement factor increases monotonically as the patches are made very small. For a lossy substrate, on the other hand, the enhancement factor decreases and the beamwidths

in the E-plane and H-plane also decrease along with an increase in the space wave for very small patches. When the patches are larger, for both the lossy and lossless cases, the beamwidths increase and then decrease again as the length of patches is increased, while the enhancement factor follows an opposite trend.

In Chapter 4, looking at the current distribution on the patches, we can see evidence of interference between the leaky wave and space wave in the E-plane and H-plane, along the interface of the substrate and air. Overall, the current distribution on the patches follows the asymptotic trend expected for the leaky wave. When the design of the 2D periodic leaky-wave antenna is optimized to get maximum power radiated at broadside, the condition of $|\beta| = \alpha$ is satisfied, i.e., the magnitude of the propagation constant is equal to the attenuation constant of the radiating fast wave harmonic of the leaky mode in both the E-plane and the H-plane. For the E-plane leaky mode, a region of open stopband at broadside has been observed but it is absent for the H-plane leaky mode. From the dispersion diagrams we observe that the wavenumber of the leaky mode, including the propagation constant and attenuation constant, vary with the angle ϕ . Three different leaky modes have been observed. The leaky mode that is dominant along the x -axis or the E-plane is called the E-plane mode, and the one that is dominant along the y -axis or the H-plane is called the H-plane mode. In addition to those, a third mode is observed, which does not seem to impact the radiation from the structure in any way. The E-plane mode propagating along the x -axis appears to be mostly responsible for the formation of the main beam, but close to the H-plane, the H-plane mode along the y -axis dominates in influencing the shape of the main beam. There are usually up to three grating lobes in the region ($0 < \theta < 90^\circ$) which seem to be due to the $(-1, 0)$ and $(-1, -1)$ Floquet waves of

the E-plane mode (perturbed surface wave mode) and the $(0, -1)$ Floquet harmonic of the H-plane mode.

In Chapter 5 the case of the directive beaming plasmonic structure has been explored in detail, and we have found it to be very similar to the 2D periodic leaky-wave antenna. The beam is much narrower in the E-plane than in the H-plane, as for the 2D periodic leaky-wave antenna at the microwave frequencies. There is a lot of dielectric loss in the substrate at the optical frequencies for the plasmonic structure; therefore there is a lot of space wave in the radiation pattern. The variation of the beamwidths in the E-plane and the H-plane and the enhancement factor with the length of the patch is similar to that seen in the 2D periodic leaky-wave antenna with a lossy substrate, which is that the beamwidths decrease and so does the enhancement factor for very small patches. When the size of the patches are increased, the beamwidths increase up to a certain point and then decrease while the enhancement factor shows an opposite trend to the beamwidths. The CAD formula for calculating the beam pattern due to the leaky wave agrees well with the main beam shape in the E-plane and to some extent in the H-plane for the plasmonic structure. The current distribution on the patches in the E-plane and the H-plane for the plasmonic structure have the same trends as the 2D periodic LWA. The E-plane current distribution shows that the propagation constants of the space wave and the leaky wave along the x -axis must be close since the beat period is relatively large and there is no significant interference. In the H-plane, however, the interference between the space wave and the leaky wave can be seen clearly. From the dispersion diagrams we see that the wavenumber, including the propagation constant and the attenuation constant of the leaky mode, is a function of the angle of propagation ϕ . As seen in the case of the 2D

periodic leaky-wave antenna at microwave frequencies, the leaky mode that is dominant along the x -axis or the E-plane is the E-plane mode, and the one that is dominant along the y -axis or the H-plane is the H-plane mode. Both of these modes combine together to produce the main beam.

We have obtained a satisfactory explanation for most the radiation characteristics and modal behavior observed in the 2D periodic leaky-wave antenna. This structure can provide a good design for a highly-directive antenna at microwave, millimeter wave, and optical frequencies with a simple feed and simple structure.

6.3 Future Work

One of the future possibilities to continue to study the 2D periodic leaky-wave antenna is to do fabrication and measurements, at least at microwave frequencies. This will help us understand some of the practical challenges for implementing the 2D periodic leaky-wave antenna and explore the best way to implement the feed. It will also give us a chance to study the effects of truncating the substrate and the ground plane. It will also form a basis for comparison with the theoretical model which assumes ideal conditions such as an infinite structure and an ideal infinitesimal magnetic dipole feed; and this will tell us how effective the theoretical model is. We will then know how well the radiation pattern obtained from the theoretical calculations agree with the actual measurements.

Along the same lines, in order to study the effects of truncation of just the periodic metallization on the surface of the dielectric, one could simulate the 2D periodic leaky-wave antenna using a truncated periodic array of patches on an infinite grounded

dielectric slab using software such as Ansys Designer, which is a full-wave simulation software.

There are several ideas for variations and improvements on the design of the 2D periodic leaky-wave antenna that can be studied in the future. For example, one could have an array of 1D periodic leaky-wave antennas with separate sources, which could be a phased array of sources, even having an amplitude variation and amplitude tapering to obtain a desired radiation pattern. One could also experiment with a 2D periodic leaky-wave antenna shaped like a cross, i.e., the periodic array of patches is restricted within a cross-shaped region with the arms of the cross along the x -axis and y -axis. Since the main beam is produced by the leaky modes travelling along the x -axis and the y -axis, removing some of the patches in between the x -axis and the y -axis might not affect the beam too much, and might even improve the pattern and also get rid of the grating lobes.

The launching efficiency of the leaky wave could be calculated for the 2D periodic LWA and the plasmonic structure. The launching efficiency is an estimate of the percentage of power that is launched into the leaky wave that produces the narrow main beam at broadside with respect to the total power radiated, which includes the power going into the space wave, the grating lobes, and the main beam.

Another task for the future is to form a better understanding of the H-plane mode, which is the dominant leaky mode propagating along the y -axis and mainly responsible for the formation of the beam in the H-plane. The E-plane mode, which is the dominant leaky mode propagating along the x -axis and is responsible for the formation of the beam in the E-plane, is well understood. The E-plane mode is due to the perturbation of the TM_0 surface wave mode. But the H-plane mode is not a perturbation of the surface wave

mode. It appears to be a perturbation of a higher order TE-like component of the surface wave. Since the TM_0 surface-wave mode has a $\cos^2 \phi$ power variation, there is no propagation of the first-order component of the surface wave along the y -axis. However there is some higher-order component of the surface wave which propagates along the y -axis, which has a TE-like polarization and could be perturbed by the periodic patches along the y -axis. At the same time, whatever the periodic spacing in the y -direction, b is, the propagation constant of the H-plane mode is always close to $2\pi/b$ when the 2D periodic leaky-wave antenna is optimized for maximum power radiation at broadside. There are many aspects of the H-plane mode that are perplexing, so this mode needs to be studied further to form a better understanding.

REFERENCES

- [1] C. H. Walter, *Traveling Wave Antennas*, McGraw-Hill, New York, 1965.
- [2] A. Hessel, “General Characteristics of Traveling-Wave Antennas,” Ch. 19 in *Antenna Theory, Part 2*, R. E. Collin and F. J. Zucker (Eds.), McGraw-Hill, New York, 1969.
- [3] T. Tamir, “Leaky-Wave Antennas,” Ch. 20 in *Antenna Theory, Part 2*, R. E. Collin and F. J. Zucker (Eds.), McGraw-Hill, New York, 1969.
- [4] A. A. Oliner and D. R. Jackson, “Leaky-Wave Antennas,” Ch. 11 in *Antenna Engineering Handbook*, 4th Ed., J. L. Volakis (Ed.), McGraw-Hill, New York, 2007.
- [5] R. E. Collins and F. J. Zucker, *Antenna Theory*, New York: McGraw-Hill, 1969, pt. 2, Ch. 19–20.
- [6] A. A. Oliner, “Leaky Wave Antennas,” in *Antenna Engineering Handbook*, R. C. Johnson, McGraw Hill, 1993.
- [7] D. R. Jackson and A. A. Oliner, “Leaky-Wave Antennas,” in *Modern Antenna Handbook*, C. A. Balanis, Wiley 2008, pp. 325-367.
- [8] W. W. Hansen, “Radiating Electromagnetic Waveguide,” U.S. Patent No. 2,402,622, 1940.
- [9] L. O. Goldstone and A. A. Oliner, “Leaky-wave antennas—Part I: Rectangular waveguides,” *IRE Transactions on Antennas and Propagation*, vol. AP-7, pp. 307–319, Oct. 1959.
- [10] J. N. Hines and J. R. Upson, “A wide aperture tapered-depth scanning antenna,” Ohio State Univ. Res. Found., Report 667-7, Columbus, Ohio, December 1957.

- [11] W. Rotman and N. Karas, "The sandwich wire antenna: A new type of microwave line source radiator," *IRE Convention Record*, part 1, pp. 166, 1957.
- [12] W. Rotman and A. A. Oliner, "Asymmetrical trough waveguide antenna," *IRE Transactions on Antennas and Propagation*, vol. AP-7, pp. 153-162, April 1959.
- [13] A. A. Oliner, "Scannable millimeter wave arrays," Final Report on RADC Contract No. F19628-84-K-0025, Polytechnic University, September 30, 1988, 528 pages in two volumes.
- [14] G. V. Trentini, "Partially reflecting sheet arrays," *IEEE Transactions on Antennas and Propagation*, vol. 4, pp. 666-671, Oct. 1956.
- [15] N. G. Alexopoulos and D. R. Jackson, "Fundamental superstrate (cover) effects on printed circuit antennas," *IEEE Transactions on Antennas and Propagation*, vol. 32, pp. 807- 816, Aug. 1984.
- [16] D. R. Jackson and N. G. Alexopoulos, "Gain enhancement methods for printed circuit antennas," *IEEE Transactions on Antennas and Propagation*, vol. 33, pp. 976-987, Sept. 1985.
- [17] D. R. Jackson and A. A. Oliner, "A leaky-wave analysis of the high-gain printed antenna configuration," *IEEE Transactions on Antennas and Propagation*, vol. 36, pp. 905-910, July 1988.
- [18] D. R. Jackson, A. A. Oliner, and A. Ip, "Leaky-wave propagation and radiation for a narrow-beam multiple-layer dielectric structure," *IEEE Transactions on Antennas and Propagation*, vol. 41, pp. 344-348, March 1993.

- [19] P. Feresidis and J. C. Vardaxoglou, "High gain planar antenna using optimised partially reflective surfaces," *IEE Proceedings on Microwaves Antennas and Propagation*, vol. 148, pp. 345-350, Dec. 2001.
- [20] T. Zhao, D. R. Jackson, J. T. Williams, H. Y. Yang, and A. A. Oliner, "2-D periodic leaky-wave antennas -- Part I: Metal patch design," *IEEE Transactions on Antennas and Propagation*, vol. 53, pp. 3505-3514, Nov. 2005.
- [21] T. Zhao, D. R. Jackson, and J. T. Williams, "2-D periodic leaky-wave antennas -- Part II: Slot design," *IEEE Transactions on Antennas and Propagation*, vol. 53, pp. 3515-3524, Nov. 2005.
- [22] G. Lovat, P. Burghignoli, F. Capolino, D. R. Jackson, and D. R. Wilton, "Analysis of directive radiation from a line source in a metamaterial slab with low permittivity," *IEEE Transactions on Antennas and Propagation*, vol. 54, no. 3, pp. 1017-1030, Mar. 2006.
- [23] G. Lovat, P. Burghignoli, F. Capolino, and D. R. Jackson, "On the combinations of low/high permittivity and/or permeability substrates for highly directive planar metamaterial antennas," *IET Microwaves, Antennas and Propagation*, vol. 1, no. 1, pp. 177-183, Feb. 2007.
- [24] J. R. Kelly and A. P. Feresidis, "Array antenna with increased element separation based on a Fabry-Pérot resonant cavity with AMC walls," *IEEE Transactions on Antennas and Propagation*, vol. 57, no. 3, pp. 682-687, Mar. 2009.
- [25] Y. Sun, Z. N. Chen, Y. Zhang, H. Chen, and T. S. P. See, "Subwavelength substrate-integrated Fabry-Pérot cavity antennas using artificial magnetic conductor," *IEEE Transactions on Antennas and Propagation*, vol. 60, no. 1, pp. 30-35, Jan. 2012.

- [26] D. R. Jackson, A. A. Oliner, T. Zhao, and J. T. Williams, "Beaming of light at broadside through a subwavelength hole: Leaky wave model and open stopband effect," *Radio Science*, vol. 40, Sep. 2005.
- [27] D. R. Jackson, J. Chen, R. Qiang, F. Capolino, and A. A. Oliner, "The role of leaky plasmon waves in the directive beaming of light through a subwavelength aperture," *Optics Express*, vol. 16, no. 26, 22 Dec. 2008.
- [28] P. Baccarelli, P. Burghignoli, F. Frezza, A. Galli, P. Lampariello, "Novel modal properties and relevant scanning behaviors of phased arrays of microstrip leaky-wave antennas," *IEEE Transactions on Antennas and Propagation*, vol. 51, no. 12, pp. 3228-3238, Dec. 2003.
- [29] J. Liu, D. R. Jackson, Y. Long, "Substrate integrated waveguide (SIW) leaky-wave antenna with transverse slots," *IEEE Transactions on Antennas and Propagation*, vol. 60, no. 1, pp. 20-29, Jan. 2012.
- [30] F. Xu, K. Wu, X. Zhang, "Periodic leaky-wave antenna for millimeter wave applications based on substrate integrated waveguide," *IEEE Transactions on Antennas and Propagation*, vol. 58, no. 2, pp. 340-347, Feb. 2010.
- [31] C. Caloz, T. Itoh, "Array factor approach of leaky-wave antennas and application to 1-D/2-D composite right/left-handed (CRLH) structures," *IEEE Microwave and Wireless Components Letters*, vol. 14, no. 6, pp. 274-276, June 2004.
- [32] M. Guglielmi, D. R. Jackson, "Broadside radiation from periodic leaky-wave antennas," *IEEE Transactions on Antennas and Propagation*, vol. 41, no. 1, pp. 31-37, Jan. 1993.

- [33] P. Baccarelli, S. Paulotto, C. Di Nallo, "Full-wave analysis of bound and leaky modes propagating along 2D periodic printed structures with arbitrary metallization in the unit cell," *IET Microwaves, Antennas and Propagation*, vol. 1, no. 1, pp. 217-225, Feb. 2007.
- [34] P. Baccarelli, S. Paulotto, C. Di Nallo, "Modal analysis of arbitrary-shaped 2D periodic structures printed on a grounded dielectric slab: real and complex solutions," *IEEE MTT-S International Microwave Symposium Digest*, pp. 1465-1468, 11-16 Jun. 2006.
- [35] Y. Kaganovsky, R. Shavit, "Full wave analysis of electric and magnetic line sources in the presence of a strip grating over a grounded dielectric slab structure," *The Second European Conference on Antennas and Propagation (EuCAP)*, pp. 1-5, 11-16 Nov. 2007.
- [36] S. Otto, A. Rennings, K. Solbach, C. Caloz, "Transmission line modeling and asymptotic formulas for periodic leaky-wave antennas scanning through broadside," *IEEE Transactions on Antennas and Propagation*, vol. 59, no. 10, pp. 3695-3709, Oct. 2011.
- [37] W. A. Johnson, S. Paulotto, D. R. Jackson, D. R. Wilton, W. L. Langston, L. I. Basilio, P. Baccarelli, G. Valerio, F. T. Celepcikay, "Modeling of general 1-D periodic leaky-wave antennas in layered media using EIGER™," *International Conference on Electromagnetics in Advanced Applications (ICEAA)*, pp. 205-208, 20-24 Sept. 2010.
- [38] S. K. Podilchak, S. F. Mahmoud, A. I. P. Freundorfer, Y. M. M. Antar, "Perturbation analysis of planar periodic leaky-wave antennas fed by cylindrical surface-

- waves,” *URSI General Assembly and Scientific Symposium*, pp. 1-4, 13-20 Aug. 2011.
- [39] S. Tooni, T. F. Eibert, M. Tayarani, L. Vietzorreck, K. Wang, “Dispersion analysis of open periodic structures using reflection pole method,” *7th European Conference on Antennas and Propagation (EuCAP)*, pp. 2365-2368, 8-12 April 2013.
- [40] S. K. Podilchak, P. Baccarelli, P. Burghignoli, A. P. Freundorfer, Y. M. M. Antary, “A sectorized planar periodic leaky-wave antenna fed by a printed surface-wave source,” *IEEE Antennas and Propagation Society International Symposium (APSURSI)*, pp. 1286-1287, 6-11 July 2014.
- [41] A. Foroozesh, R. Paknys, D. R. Jackson, J. J. Laurin, “Beam focusing using backward-radiating waves on conformal leaky-wave antennas based on a metal strip grating,” *IEEE Transactions on Antennas and Propagation*, vol. 63, no. 11, pp. 4667-4677, Nov. 2015.
- [42] A. Foroozesh, L. Shafai, “2-D truncated periodic leaky-wave antennas with reactive impedance surface ground planes,” *IEEE Antennas and Propagation Society International Symposium*, pp. 15-18, 9-14 July 2006.
- [43] M. Lorente-Crespo, C. Mateo-Segura, “Analysis of 2-D periodic leaky-wave nano-antennas in the NIR,” *IEEE Antennas and Propagation Society International Symposium (APSURSI)*, pp. 83-84, 6-11 July 2014.
- [44] C. Mateo-Segura, G. Goussetis, A. P. Feresidis, “Analysis of 2-D periodic leaky wave antennas with subwavelength profile,” *IEEE Antennas and Propagation Society International Symposium (APSURSI)*, pp. 1-4, 1-5 June 2009.

- [45] J. R. Kelly, T. Kokkinos, A. P. Feresidis, "Analysis and design of sub-wavelength resonant cavity type 2-D leaky-wave antennas," *IEEE Transactions on Antennas and Propagation*, vol. 56, no. 9, pp. 2817-2825, Sept. 2008.
- [46] C. Mateo-Segura, M. Garcia-Vigueras, G. Goussetis, A. P. Feresidis, J. L. Gomez-Tornero, "A simple technique for the dispersion analysis of Fabry-Perot cavity leaky-wave antennas," *IEEE Transactions on Antennas and Propagation*, vol. 60, no. 2, pp. 803-810, Feb. 2012.
- [47] T. W. Ebbesen, H. J. Lezec, T. F. Ghaemi, T. A. Thio, P. A. Wolf, "Extraordinary optical transmission through subwavelength hole arrays," *Nature*, vol. 391, pp 667-669, Feb 1998.
- [48] H. J. Lezec, A. Degiron, E. Devaux, R. A. Linke, L. Martin-Moreno, F. J. Garcia-Vidal, T. W. Ebbesen, "Beaming Light from a Subwavelength Aperture," *Science*, vol. 297, issue 5582, pp. 820-822, Aug 2002.
- [49] F. Wang, M. Xiao, K. Sun, Q. -H. Wei, "Generation of radially and azimuthally polarized light by optical transmission through concentric circular nanoslits in Ag films," *Optics Express*, vol. 18, issue 1, pp. 63-71, 2010.
- [50] G. Li, F. Xiao, K. Li, K. Alameh, A. Xu, "Theory, figures of merit, and design recipe of the plasmonic structure composed of a nano-slit aperture surrounded by surface corrugations," *Journal of Lightwave Technology*, vol. 30, no. 15, pp. 2405-2414, 1 Aug. 2012.
- [51] D. Wang, T. Yang, K. B. Crozier, "Optical antennas integrated with concentric ring gratings: electric field enhancement and directional radiation," *Optics Express*, vol. 19, issue 3, pp. 2148-2157, 2011.

- [52] O. Mahboub, S. C. Palacios, C. Genet, F. J. Garcia-Vidal, S. G. Rodrigo, L. Martin-Moreno, T. W. Ebbesen, "Optimization of bull's eye structures for transmission enhancement," *Optics Express*, vol. 18, issue 11, pp. 11292-11299, 2010.
- [53] M. S. Muradoglu, T. W. Ng, A. Neild, I. Gralinski, "Tailored leaky plasmon waves from a subwavelength aperture for optical particle trapping on a chip," *Journal of Optical Society of America B*, vol. 28, issue 4, pp. 602-607, 2011.
- [54] Y. Lee, K. Hoshino, A. Alù, X. Zhang, "Tunable directive radiation of surface-plasmon diffraction gratings," *Optics Express*, vol. 21, issue 3, pp. 2748-2756, 2013.
- [55] F. -F. Ren, K. -W. Ang, J. Ye, M. Yu, G. -Q. Lo, D. -L. Kwong, "Split bull's eye shaped aluminum antenna for plasmon-enhanced nanometer scale germanium photodetector," *Nano Letters*, vol. 11, no. 3, pp. 1289-1293, Feb. 2011.
- [56] S. Campione, C. Guclu, Q. Song, O. Boyraz, F. Capolino, "An optical leaky wave antenna with Si perturbations inside a resonator for enhanced optical control of the radiation," *Optics Express*, vol. 20, issue 19, pp. 21305-21317, 2012.
- [57] Q. Song, S. Campione, O. Boyraz, F. Capolino, "Silicon-based optical leaky wave antenna with narrow beam radiation," *Optics Express*, vol. 19, issue 9, pp. 8735-8749, 2011.
- [58] M. Beruete, I. Campillo, J. S. Dolado, J. E. Rodriguez-Seco, E. Perea, F. Falcone, M. Sorolla, "Very low-profile "Bull's Eye" feeder antenna," *IEEE Antennas and Wireless Propagation Letters*, vol. 4, pp. 365-368, 2005.
- [59] C. Huang, Z. Zhao, X. Luo, "Application of "bull's eye" corrugated grooves integrated with artificially soft surfaces structure in the patch antenna to improve

- radiation performance,” *Microwave and Optical Technology Letters*, vol. 51, pp. 1676–1679, July 2009.
- [60] Tianxia Zhau, *Analysis and Design of 2-D Periodic Leaky Wave Antennas using Metal Patches or Slots*, PhD Dissertation, University of Houston, August 2003.
- [61] Christophe Caloz, David R. Jackson, and Tatsuo Itoh, “Leaky-Wave Antennas,” Chapter 9 in *Frontiers in Antennas, Next Generation Design and Engineering*, Frank B. Gross (Ed.), 1st Ed., McGraw-Hill, 2011.
- [62] Constantine A. Balanis, *Antenna Theory, Analysis and Design*, 3rd Ed., Wiley, New Jersey, 2005.
- [63] P. Burghignoli, G. Lovat, D. R. Jackson, “Analysis and optimization of leaky-wave radiation at broadside from a class of 1-D periodic structures,” *IEEE Transactions on Antennas and Propagation*, vol. 54, no. 9, pp. 2593-2604, Sept. 2006.